DESIGN AND APPLICATION OF THE META-GGA AND RANGE-SEPARATED HYBRID EXCHANGE-CORRELATION FUNCTIONALS

By

BIKASH PATRA

Enrolment No: PHYS11201504012

National Institute of Science Education and Research, Bhubaneswar

A thesis submitted to the

Board of Studies in Physical Sciences

In partial fulfillment of requirements

for the Degree of

DOCTOR OF PHILOSOPHY

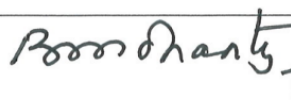*of*

HOMI BHABHA NATIONAL INSTITUTE

November, 2021

Homi Bhabha National Institute

Recommendations of the Viva Voce Committee

As members of the Viva Voce Committee, we certify that we have read the dissertation prepared by **Bikash Patra** entitled "Design and application of the meta-GGA and range-separated hybrid exchange-correlation functionals" and recommend that it may be accepted as fulfilling the thesis requirement for the award of Degree of Doctor of Philosophy.
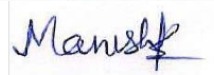

Chairman - Prof. Bedangadas Mohanty   *Boro dhanty* 15|11|2021

Guide/Convener - Dr. Prasanjit Samal   *15-11-21*

Examiner - Prof. Manish Kumar Niranjan   *Manish*

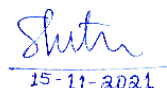
Member 1- Dr. Joydeep Bhattacharjee   *15/11/21*

Member 2- Dr. A. V. Anil Kumar   *15|11|21*
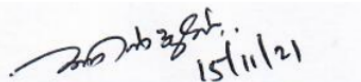
Member 3- Prof. Suresh Kumar Patra   *15-11-2021*

Final approval and acceptance of this thesis is contingent upon the candidate's submission of the final copies of the thesis to HBNI.

I/We hereby certify that I/we have read this thesis prepared under my/our direction and recommend that it may be accepted as fulfilling the thesis requirement.

Date: 15-11-21

Place: Bhubaneswar

Guide

STATEMENT BY AUTHOR

This dissertation has been submitted in partial fulfillment of requirements for an advanced degree at Homi Bhabha National Institute (HBNI) and is deposited in the Library to be made available to borrowers under rules of the HBNI.

Brief quotations from this dissertation are allowable without special permission, provided that accurate acknowledgement of source is made. Requests for permission for extended quotation from or reproduction of this manuscript in whole or in part may be granted by the Competent Authority of HBNI when in his or her judgment the proposed use of the material is in the interests of scholarship. In all other instances, however, permission must be obtained from the author.

Bikash Patra

DECLARATION

I, hereby declare that the investigation presented in the thesis has been carried out by me. The work is original and has not been submitted earlier as a whole or in part for a degree / diploma at this or any other Institution / University.

Bikash Patra

List of Publications arising from the thesis

Journal

1. "Long-range corrected density functional through the density matrix expansion based semilocal exchange hole", **Bikash Patra**, Subrata Jana and Prasanjit Samal, Physical Chemistry Chemical Physics, **2018**, 20, 8991-8998.
Correction: Physical Chemistry Chemical Physics, **2019**, 21, 22158-22158.

2. "Efficient band gap prediction of semiconductors and insulators from a semilocal exchange-correlation functional", **Bikash Patra**, Subrata Jana, Lucian A. Constantin and Prasanjit Samal, Physical Review B, **2019**, 100, 045147.

3. "Relevance of the Pauli kinetic energy density for semilocal functionals", **Bikash Patra**, Subrata Jana, Lucian A. Constantin and Prasanjit Samal, Physical Review B, **2019**, 100, 155140.

4. "Correct Structural Phase Stability of FeS_2, TiO_2 and MnO_2 from a Semilocal Density Functional", **Bikash Patra**, Subrata Jana, Lucian A. Constantin and Prasanjit Samal, The Journal of Physical Chemistry C, **2021**, 125, 4284-4291.

Conferences

1. Poster:-"Density Matrix Based Semilocal Exchange Hole Applied to Range Separated Density Functional Theory.", **Bikash Patra**, National Conference on Recent Trends in Condensed Matter Physics (RTCMP 2017), Bose Institute, Kolkata, West Bengal-700054, India.

2. Poster:-"Density Matrix Based Semilocal Exchange Hole Applied to Range Separated Density Functional Theory.", **Bikash Patra**, International Workshop on Advanced Materials (IWAM-2017), National Institute of Science & Technology, Berhampur, Orissa-761008, India.

3. Poster:-"Meta-GGA Pseudopotential for Plane Wave Calculations", **Bikash Patra**, International Workshop on Evolution of Electronic Structure Theory & Experimental Realization (EESTER 2018), SRM Institute of Science and Technology & Indian Institute of Technology Madras, Tamil Nadu-600036, India.

4. Oral:-"Relevance of the Pauli Kinetic Energy Density for Semilocal Functionals", **Bikash Patra**, International Workshop on Evolution of Electronic Structure Theory & Experimental Realization (EESTER 2020), Dept. of Physics and Nanotechnology, SRMIST KTR (India), Dept. of Physics, IIT Madras (India) and Dept. of Physics and Astronomy, Uppsala University (Sweden).

Bikash Patra

DEDICATIONS

Dedicated to

.....

My Grandfather and Grandmother and Father

.....

.....

ACKNOWLEDGEMENTS

Contents

SUMMARY

Density functional theory (DFT) is one of the most widely used methods to understand the properties of many-particle systems due to its affordable computational cost to accuracy ratio. The foundation of DFT started with the discovery of Hohenberg-Kohn (HK) [1] theorem which proved a one-to-one mapping between the external potential and the ground state density of a many-electron system. In principle, this allows us to investigate the properties of a system in terms of the ground state density alone. However, the practical application of DFT gains popularity only after the Kohn-Sham (KS) formalism [2] which maps the interacting many-body system to an effective non-interacting system with the same density. This ensures the ground state energy of both systems remains the same. The KS equation contains the kinetic energy term, interaction of electrons with nucleus, classical interaction between the electrons i.e. Hartree interaction, and the exchange-correlation (XC) term. All the terms in the KS equation are known exactly except the XC potential. So, for practical calculations, we need to approximate the form of XC functional. Over the years, there are several approximations developed for the XC functional starting from local density approximation (LDA), generalized gradient approximation (GGA), meta-GGA to hybrid functional.

This thesis will be focused on the development and application of the meta-GGA XC functional both at the semilocal and the meta-GGA range-separated hybrid level. Exchange energy functional can be derived if the corresponding exchange hole is known. Also, the exchange hole can be used to derive the range-separated exchange energy functional. In fact, we have developed a long-range corrected XC functional using the recently developed Tao-Mo [3] meta-GGA exchange hole. The proposed long-range corrected functional improves the properties of a broad range of molecular databases and also for the fractional particle number cases and dissociation energies because of its improved long-range behaviour. Next, we construct meta-GGA exchange functionals by modelling

the exchange hole using model hydrogen and cuspless hydrogen densities, following a modified Becke-Roussel (BR) [4] approach. These functionals are applied to predict the band gap of the narrow, intermediate, and wide gap insulators and the layered materials. Their performance is comparable to the hybrid functional results and better than the known semilocal functionals. It is also shown that the cuspless hydrogen density is more suitable for solid-state calculation than the hydrogen density. Next, we build a meta-GGA exchange functional by satisfying some exact constraints, following the BR approach, which depends only on the Pauli kinetic enhancement factor. This functional is shown to give good results over a broad range of molecular and solid-state systems. In fact, this functional is the best performing semilocal functional for the semiconductor band gaps. Further, this functional is applied to predict the phase stability ordering of the Fe_2, TiO_2 and MnO_2 polymorphs. These systems are challenging for semilocal functionals and the proposed functional is shown to recover the correct ordering of all the polymorphs.

References

1. P. Hohenberg and W. Kohn, Phys. Rev. 136, B864 (1964).

2. W. Kohn and L. J. Sham, Phys. Rev. 140, A1133 (1965).

3. J. Tao and Y. Mo, Phys. Rev. Lett, 117, 073001 (2016).

4. A. Becke and Roussel, Phys. Rev. A, 39, 3671 (1989).

List of Figures

List of Tables

Chapter 1

Quantum Many-Body Problem

1.1 Introduction

The exact description of the electronic structure of atoms, molecules, and solids is important to understand the properties of the significant portion of condensed matter physics, quantum chemistry, and material science. However, this is a daunting task mainly because of two reasons. Firstly, electrons in a matter must be described by the laws of quantum mechanics rather than classical ones. This is because the de Broglie wavelength ($\lambda = h/p$) of an electron in a many-electron environment is comparable to the average inter-particle separation, where h is the Planck's constant and p be the momentum of the electron. The second problematic case arises from the complex multi-particle interaction due to the overlapped de Broglie wavelength. This causes the solution to be impossible for many-electron systems and the complexity grows drastically with the increasing number of electrons. For these reasons, the electronic structure of matter is known as the quantum many-body problem.

The quantum many-body problem is surprising because the equations required for exact solution are known but the exact solution is possible only for a few restricted systems. The properties of any time-independent quantum system can be characterized by solving

the Schrödinger equation,

$$\hat{H}\psi(\{\mathbf{R}_I\},\{\mathbf{x}_i\}) = E\psi(\{\mathbf{R}_I\},\{\mathbf{x}_i\}), \tag{1.1}$$

where $\hat{H}$, $\psi(\{\mathbf{R}_I\},\{\mathbf{x}_i\})$ and E are the Hamiltonian, many-body wavefunction, and total energy of the system respectively. Here, $\{\mathbf{x}_i\} \equiv \{\mathbf{r}_i, \sigma_i\}$ for $i = 1,2,3,\cdots,N$ denotes the position and spin coordinates of N electrons and similarly, $\{\mathbf{R}_I\}$ for $I = 1,2,3,\cdots,M$ denotes the position of the M nuclei of the interacting system under consideration. The Hamiltonian of Eq. 1.1 consists of the following terms

$$\begin{aligned}
\hat{H} &= \hat{T}_{\mathrm{n}}(\mathbf{R}) + \hat{T}_{\mathrm{e}}(\mathbf{r}) + \hat{V}_{\mathrm{nn}}(\mathbf{R}) + \hat{V}_{\mathrm{ee}}(\mathbf{r}) + \hat{V}_{\mathrm{ne}}(\mathbf{r},\mathbf{R}) \\
&= -\sum_{I=1}^{M}\frac{\hbar^2}{2M_I}\nabla_I^2 - \sum_{i=1}^{N}\frac{\hbar^2}{2m_e}\nabla_i^2 + \frac{e^2}{4\pi\varepsilon_0}\sum_{I}^{M}\sum_{J>I}^{M}\frac{Z_I Z_J}{|\mathbf{R}_I - \mathbf{R}_J|} \\
&\quad + \frac{e^2}{4\pi\varepsilon_0}\sum_{i}^{N}\sum_{j>i}^{N}\frac{1}{|\mathbf{r}_i - \mathbf{r}_j|} - \frac{e^2}{4\pi\varepsilon_0}\sum_{I}^{M}\sum_{i}^{N}\frac{Z_I}{|\mathbf{R}_I - \mathbf{r}_i|},
\end{aligned} \tag{1.2}$$

where Z_I, M_I, and m_e are the atomic numbers, nuclear masses, and electron mass respectively. The first two terms of the above equation represent the kinetic energy of the nuclei and electrons. The last three terms represent the interaction energy operators between nuclei-nuclei ($\hat{V}_{\mathrm{nn}}$), electron-electron ($\hat{V}_{\mathrm{ee}}$) and electron-nuclei ($\hat{V}_{\mathrm{ne}}$) respectively. In practice, the partial differential equation 1.1 is almost impossible to solve within a full quantum mechanical framework. There are various features that contribute to this difficulty, but the most important one is that the two-body nature of the Coulomb interaction which makes the above Schrödinger equation not separable.

As a first approximation, we can partially decouple the motion of electrons from the nuclear motion due to the time scale associated with the motion of nuclei is much larger than that of electrons. This is known as the Born-Oppenheimer approximation.[1] Using this approximation, we can factorize the total wavefunction ψ into a nuclear wavefunction ψ_n and electronic wavefunction ψ_e,

$$\psi(\{\mathbf{R}_I\},\{\mathbf{x}_i\}) = \psi_{\mathrm{n}}(\{\mathbf{R}_I\})\psi_{\mathrm{e}}(\{\mathbf{R}_I\};\{\mathbf{x}_i\}). \tag{1.3}$$

This approximation allows us to fix nuclear configuration at some particular value $\mathbf{R}_c$ and solve for the electronic wavefunction $\psi_e(\{\mathbf{R}_c\}; \{\mathbf{x}_i\})$ which depends parametrically on R. If we repeat this for several values of R, we will get the potential energy curve along which nuclei move. Finally, the electronic Shrödinger equation for fixed nuclear position becomes

$$\hat{H}_e \psi_e(\{\mathbf{R}_I\}; \{\mathbf{x}_i\}) = E_e \psi_e(\{\mathbf{R}_I\}; \{\mathbf{x}_i\}), \tag{1.4}$$

where the electronic Hamiltonian is

$$\hat{H}_e = -\sum_{i=1}^{N} \frac{1}{2}\nabla_i^2 + \sum_{i}^{N}\sum_{j>i}^{N} \frac{1}{|\mathbf{r}_i - \mathbf{r}_j|} - \sum_{I}^{M}\sum_{i}^{N} \frac{Z_I}{|\mathbf{R}_I - \mathbf{r}_i|}. \tag{1.5}$$

In the above equation, we use atomic units, whereby $\hbar = e = m_e = 4\pi\varepsilon_0 = 1$. Unless otherwise stated, we will use this unit for the rest part of the thesis.

Although we simplified our many-body Schrödinger equation in Eq. 1.4 by applying Born-Oppenheimer approximation, but still the solution of the electronic Schrödinger equation i.e. Eq. 1.4 is too complex because of the many-electron wavefunction which depends on $3N$ variables and which for a solid of $N \sim 10^{26}$ electrons, is an unmanageable number of degrees of freedom. In the next section, we will briefly describe the various wavefunction based approaches to obtain approximate solutions of Eq. 1.4.

1.2   Wavefunction Based Methods for Solving Many-Electron Schrödinger Equation

Many-electron wavefunction ψ is the basic quantity for the wave function based methods but its functional form is very complicated. Practically, we start with some reasonable guess for the ψ and then try to calculate it using the variational principle. The variation principle states that for any guessed wave function the expectation value of the Hamiltonian ($\hat{H}_e$) always gives the upper bound to the electronic ground state energy

$$\langle \psi | \hat{H}_e | \psi \rangle \geq \langle \psi_0 | \hat{H}_e | \psi_0 \rangle, \tag{1.6}$$

where the equality sign holds only for the true ground state wave function ψ_0. In the next section, this principle will be applied for the minimization of the approximated Hartree-Fock wave function.

1.2.1 Hartree-Fock Method

The starting point of this method was introduced by D. R. Hartree in 1928, where each electron in a many-electron system is assumed to be moving in an effective potential which takes into account the effect of attraction to the nucleus and the average effect of the repulsive electron-electron interactions due to other electrons. Each electron in the system is described by its own wavefunction. In 1930, V. A. Fock generalized Hartree's method which takes into account the antisymmetry requirement of the many-electron wavefunction. In the Hartree-Fock (HF) approximation, the trial wavefunction of a N electron system is taken as a Slater determinant[2]

$$
\psi^{\mathrm{HF}} = \frac{1}{\sqrt{N!}}
\begin{vmatrix}
\phi_1(x_1) & \phi_1(x_2) & \dots & \phi_1(x_N) \\
\phi_2(x_1) & \phi_2(x_2) & \dots & \phi_2(x_N) \\
\vdots & \vdots & \ddots & \vdots \\
\phi_N(x_1) & \phi_N(x_2) & \dots & \phi_N(x_N)
\end{vmatrix}
\tag{1.7}
$$

, where the spin-orbitals follow the orthonormality condition i.e.

$$
\langle \phi_i | \phi_j \rangle = \int \phi_i^*(x)\phi_j(x)dx = \delta_{ij}.
\tag{1.8}
$$

In the above equation, $\int dx$ implies an integration over space coordinates and summation over spin coordinates. The expectation value of the Hamiltonian of Equation 1.5 is given by

$$
E_{\mathrm{HF}} = \langle \psi^{\mathrm{HF}} | \hat{H}_e | \psi^{\mathrm{HF}} \rangle = \sum_{i=1}^{N} h_i + \frac{1}{2} \sum_{i,j=1}^{N} (J_{ij} - K_{ij}),
\tag{1.9}
$$

where

$$h_i = \int \phi_i^*(x) \left(-\frac{1}{2}\nabla_{\mathbf{r}}^2 + v_{\text{ext}}(\mathbf{r}) \right) \phi_i(x) dx \tag{1.10}$$

$$J_{ij} = \int \int \phi_i^*(x_1)\phi_j^*(x_2)\frac{1}{\mathbf{r}_{ij}}\phi_i(x_1)\phi_j(x_2)dx_1 dx_2 \tag{1.11}$$

$$K_{ij} = \int \int \phi_i^*(x_1)\phi_j^*(x_2)\frac{1}{\mathbf{r}_{ij}}\phi_i(x_2)\phi_j(x_1)dx_1 dx_2 \tag{1.12}$$

The terms in Eq. 1.10 represent the kinetic energy and interaction energy of the electrons with the external potential respectively. The term in Eq. 1.11 is the classical Coulomb interaction energy between electrons and the Eq. 1.12 represents the exchange energy between electrons arising due to the Pauli correlation. For $i = j$, we have $J_{ii} = K_{ii}$ i.e. the self-interaction energy is properly cancelled in the HF theory. Minimizing the above expression w.r.t. the orbital ϕ_i gives the canonical HF equation for the ith orbital

$$\left(-\frac{1}{2}\nabla_{\mathbf{r}}^2 + v_{\text{ext}}(\mathbf{r}) + \int \frac{\rho(\mathbf{r}')}{|\mathbf{r}-\mathbf{r}'|}d\mathbf{r}' \right)\phi_i(\mathbf{r}) - \sum_{\substack{i,j \\ (\sigma_i||\sigma_j)}} \int \int \frac{\phi_j^*(\mathbf{r}')\phi_j(\mathbf{r})\phi_i(\mathbf{r}')}{|\mathbf{r}-\mathbf{r}'|}d\mathbf{r}' = \varepsilon_i\phi_i(\mathbf{r}),$$

$$\tag{1.13}$$

where ε_i is the Lagrange multiplier to ensure the orthonormality of the orbitals and σ_i is the spin index of the ith orbital. The Eq. 1.13 should be solved self-consistently and the solution results in a set of orthonormal orbitals with corresponding eigenvalues. Some of the important advantages of the HF method are:

1. The enormous conceptual simplification from the complicated many-body problem due to the independent particle approximation.

2. The good accuracy of the total energy of molecules. For example, 98.5% for He,[3] 99% for LiH,[4] 99.5% for N$_2$[5] etc.

3. HF orbitals are suitable as zero-order states for perturbation schemes.[6]

However, there are some important disadvantages of the HF theory:

1. The error in the binding energy of molecules is large.

2. The dissociation limit of molecules is usually predicted incorrectly.

1.2.2 Post HF method

The HF method is an approximation to solve the Schrödinger equation where the electrons move in the average field of other electrons. However, the position of an electron in a system depends on the position of other electrons, and on average they are further apart than described by the HF method. This phenomenon of correlated motion of electrons is known as *electron correlation*. Conventionally, correlation energy is defined as

$$E_{\mathrm{c}} = E_{\mathrm{exact}} - E_{\mathrm{HF}}, \tag{1.14}$$

where E_{exact} is the exact ground state energy of Eq. 1.4 and E_{HF} is the ground state energy in the HF approximation method. There are two kinds of correlation which is missed in the HF method, one is called dynamical correlation and another one is static correlation. Dynamical correlation is dominated by the movement of electrons with opposite spin, which is poorly described in the HF theory. Static correlation is important in systems where the ground state is well described only with more than one degenerate Slater determinant.

Some of the post HF method includes:

- **Configuration Interaction** : The correlated wavefunction ψ_{CI} in this approach is taken as a linear combination of the ground and excited-state determinants

$$\psi_{\mathrm{CI}} = \sum_I C_I \psi_I = C_0 \psi^{\mathrm{HF}} + \sum_{ia} C_i^a \psi_i^a + \sum_{\substack{a>b \\ i>j}} C_{ij}^{ab} \psi_{ij}^{ab} + \cdots, \tag{1.15}$$

where $i, j, ..$ denotes occupied spin orbitals in ψ^{HF} while $a, b, ..$ are the unoccupied spin orbitals. ψ_i^a, ψ_{ij}^{ab}, .. are the singly, doubly, .. excited state determinants. The expansion coefficients C_I are determined using the variational principle.

- **Coupled Cluster** : The wavefunction of the coupled cluster method is written as

$$\psi_{\mathrm{CC}} = \exp(\hat{T}) \psi^{\mathrm{HF}}, \tag{1.16}$$

where $\hat{T}$ is the cluster operator which produces a linear combination of excited state determinants upon acting on the reference HF wavefunction. If we include all possible excitations, this wavefunction is equivalent to full CI wavefunction. The choice of exponential ansatz guarantees the size extensivity of the solution.

- **Møller-Plesset Perturbation Theory** : This method adds electron correlation by using Rayleigh-Schrödinger perturbation theory, usually up to second (MP2), third (MP3) or fourth (MP4) order. HF Hamiltonian is taken as the unperturbed Hamiltonian and the perturbation term is the difference between the exact electronic Hamiltonian and the HF Hamiltonian.

Although, the mentioned post HF methods improve the result from the HF method, but these methods are computationally very expensive. In the next section, we will describe a method of solving Eq. 1.4 in which the many-electron wavefunction is bypassed using the density and which gives the reasonable computational cost to accuracy ratio.

1.3   Density Functional Theory

Density functional theory uses the density $\rho(\mathbf{r})$ as the central quantity. The main advantage of using the density rather than wave function is that it is always three dimensional regardless of the number of electrons in the system. This enables DFT to compute the properties of large systems containing hundreds to thousands of atoms. Electron density is defined as

$$\rho(\mathbf{r}) = N \int \cdots \int |\psi(\mathbf{x}_1, \mathbf{x}_2, \cdots, \mathbf{x}_N)|^2 d\sigma_1 d\mathbf{x}_2 \cdots d\mathbf{x}_N, \qquad (1.17)$$

and this determines the probability of getting one of the N electrons with arbitrary spin at $\mathbf{r}$ while the other $N-1$ electrons have arbitrary spin and positions in the state ψ. This is always non-negative and integrates to the total number of electrons

$$\int \rho(\mathbf{r}) d\mathbf{r} = N. \qquad (1.18)$$

1.3.1 Thomas-Fermi Theory

The first attempt to solve a many-body problem by taking density as a basic variable is given by Thomas and Fermi. This is known as Thomas-Fermi (TF)[7,8] theory. In this theory, the kinetic energy of an interacting many-particle system of N electrons is considered as a homogeneous system of N independent fermions. The kinetic energy of it is given by the expression

$$T_{\text{TF}}[\rho] = C_k \int \rho(\mathbf{r})^{5/3} d\mathbf{r}, \tag{1.19}$$

where $C_k = 3(3\pi^2)^{2/3}/10$ and $\rho(\mathbf{r})$ be the density of electrons at space point $\mathbf{r}$. The total energy is given by adding the kinetic energy given above with the classical electrostatic energy and interaction with external potential i.e.

$$E_{\text{TF}}[\rho] = T_{\text{TF}}[\rho] + \frac{1}{2} \int \int \frac{\rho(\mathbf{r})\rho(\mathbf{r}')}{|\mathbf{r}-\mathbf{r}'|} d\mathbf{r} d\mathbf{r}' + \int v_{\text{ext}}(\mathbf{r})\rho(\mathbf{r}) d\mathbf{r}. \tag{1.20}$$

The energy calculated using the above expression overestimates the total energy because of the missing exchange and correlation energy. The TF equation for density is obtained by minimizing the TF energy w.r.t. density which satisfies the number of particles,

$$\frac{5}{3} C_k \rho(\mathbf{r})^{2/3} + v_{\text{ext}}(\mathbf{r}) + \int \frac{\rho(\mathbf{r}')}{|\mathbf{r}-\mathbf{r}'|} d\mathbf{r}' = \mu, \tag{1.21}$$

where μ is the Lagrange multiplier to satisfy the constraint $\int \rho(\mathbf{r}) d\mathbf{r} = N$. In general, the TF equation can be solved self-consistently. The TF equation can be improved by including the exchange energy functional into the total energy functional. However, it was very difficult to express exchange energy functional in terms of density only. This is done in the same spirit of kinetic energy, where the exchange energy is approximated same as the exchange energy of the homogeneous electron gas with the density replaced by local density $\rho(\mathbf{r})$ at each point. This was suggested by Dirac[9] and the corresponding TFD energy functional and the corresponding equation are given as

$$E_{\text{TFD}}[\rho] = T_{\text{TF}}[\rho] + \frac{1}{2} \int \int \frac{\rho(\mathbf{r})\rho(\mathbf{r}')}{|\mathbf{r}-\mathbf{r}'|} d\mathbf{r} d\mathbf{r}' + \int v_{\text{ext}}(\mathbf{r})\rho(\mathbf{r}) d\mathbf{r} + C_x \int \rho(\mathbf{r})^{4/3} d\mathbf{r}, \tag{1.22}$$

$$\frac{5}{3}C_k\rho(\mathbf{r})^{2/3} + v_{\text{ext}}(\mathbf{r}) + \int \frac{\rho(\mathbf{r'})}{|\mathbf{r}-\mathbf{r'}|}d\mathbf{r'} + \frac{4}{3}C_x\rho(\mathbf{r})^{1/3} = \mu, \quad (1.23)$$

where $C_x = -\frac{3}{4}\left(\frac{3}{\pi}\right)^{1/3}$.

Although the idea of realizing the inhomogeneous system as locally homogeneous for the kinetic energy term is reasonable for metallic systems but it turns out to be a very bad approximation for atomic and molecular systems. The density diverges at the nucleus and it does not show atomic shell structure. To improve these features, better treatment of kinetic energy functional was needed. However, in the next section, we will describe the modern density functional theory (DFT) approaches where the kinetic energy is treated to a better accuracy at the cost of introducing one-particle orbitals.

1.3.2 The Hohenberg-Kohn Theorem

The objective of the TF approach was to write the energy of a many-electron system solely in terms of density. However, the idea was intuitive at that time because of the unavailability of the proper framework which guarantees the above mapping. In 1964, Hohenberg and Kohn (HK)[10] proved a theorem that provides solid mathematical grounds for the TF ideas.

Theorem I There exists a one-to-one mapping between the electron density and the external potential up to a trivial constant.

Corollary Since the density $\rho(\mathbf{r})$ determines the external potential, hence it also determines the complete Hamiltonian. The ground state wavefunction ψ is obtained by solving the full many-electron Schrödinger equation. Therefore, the ground state energy is expressed as a functional of the density

$$E[\rho] = \langle\psi|\hat{H}_e[\rho]|\psi\rangle = F[\rho] + \int v_{\text{ext}}(\mathbf{r})\rho(\mathbf{r})d\mathbf{r}, \quad (1.24)$$

where

$$F[\rho] = \langle\psi|\hat{T}[\rho(\mathbf{r})] + \hat{V}_{\text{ee}}[\rho(\mathbf{r})]|\psi\rangle. \quad (1.25)$$

Eq. 1.25 is called the universal functional as it is independent of the external potential. Its form remains unchanged irrespective of the system. Therefore, a particular kind of system is completely determined by $v_{ext}[\rho(\mathbf{r})]$.

Theorem II The ground-state energy can be determined using variational principle and the density which minimizes the total energy functional is the exact ground-state density.

Corollary This implies that the energy functional $E[\rho(\mathbf{r})]$ gives the true ground-state energy only for the exact ground-state density $\rho_0(\mathbf{r})$. For any other density, the predicted energy will be higher than the ground state energy.

$$E[\rho_0] = \min_{\rho(\mathbf{r})}\left\{E[\rho(\mathbf{r})]\right\} \leq E[\rho(\mathbf{r})]. \tag{1.26}$$

The ground-state energy can be calculated using the variational principle with the constraint of conserving the number of electrons.

$$\delta\left\{E[\rho(\mathbf{r})] - \mu\left(\int \rho(\mathbf{r})d\mathbf{r} - N\right)\right\} = 0. \tag{1.27}$$

This leads to the Euler-Lagrange equation,

$$\frac{\delta E[\rho(\mathbf{r})]}{\delta\rho(\mathbf{r})} = \mu = v_{\text{ext}}(\mathbf{r}) + \frac{\delta F[\rho(\mathbf{r})]}{\delta\rho(\mathbf{r})}, \tag{1.28}$$

where, μ is the Lagrange multiplier and also known as the chemical potential of the electrons. These two theorems form the mathematical basis of density-functional theory.

1.3.3 Constrained Search Formulation

In the HK theorem, the electron density which determines the external potential needs to come from some antisymmetric ground state wave function. Although, it is necessary for the true ground state density ρ_0 but it may violate for other trial density $\tilde{\rho}$.

In 1982, Levy[11] formulated DFT in such a way that assures the antisymmetric origin of density. Levy proposed the constrained search formalism by which the expression of

Eq. 1.25 is redefined in the following way

$$F[\rho] = \min_{\psi \to \rho} \left\{ \langle \psi | \hat{T} + \hat{V}_{ee} | \psi \rangle \right\}, \tag{1.29}$$

where the density ρ is such that

$$\rho(\mathbf{r}) \geq 0, \qquad \int \rho(\mathbf{r}) d\mathbf{r} = N \quad \text{and} \quad \int |\nabla \rho^{1/2}(\mathbf{r})|^2 d\mathbf{r} < \infty \tag{1.30}$$

with the additional constraint that density should come from an antisymmetric wave function. In this way, this formalism eliminates the conceptual difficulty of possible unphysical densities.

1.4   Practical DFT : Kohn-Sham Construction

The Eqs. 1.24 and 1.26 in the previous subsection give a way of calculating the ground-state properties if the form of $F[\rho]$ is known. However, for practical calculations, we have to rely on the approximate form of $F[\rho]$, and finding a good approximation for this is not easy. As we have already seen in TF and TFD theory, an approximate form of $T[\rho]$ and $V_{ee}[\rho]$ is used. Although this provides a nice simplicity but the main drawback of the TF procedure is related to the expression of the kinetic energy part in terms of density. In 1965, Kohn and Sham (KS)[12] introduced an idea to approximate the kinetic energy term in a better way. They assumed that there exists an equivalent non-interacting system corresponding to the interacting system, where the ground-state density $\rho(\mathbf{r})$ remains the same for both the systems. This system of non-interacting N electrons with density $\rho(\mathbf{r})$ is described by the Hamiltonian,

$$\hat{H}_{KS} = \sum_{i=1}^{N} \left[-\frac{1}{2} \nabla_i^2 + v_{KS}(\mathbf{r}_i) \right]. \tag{1.31}$$

Here, the effective potential $v_{KS}(\mathbf{r})$ is such that the ground-state density of $\hat{H}_{KS}$ equals to $\rho(\mathbf{r})$. The HK theorem ensures that the ground state energy remains the same for both the

interacting and non-interacting system.

As the Hamiltonian in Eq. 1.31 has no electron-electron interactions, one can write its eigenstate in terms of a single Slater determinant $\Phi[\rho]$ in the same way of Eq. 1.7. Within this approximation, density and kinetic energy will be expressed as

$$\rho(\mathbf{r}) = \sum_{i=1}^{N} |\phi_i(\mathbf{r})|^2 \quad \text{and} \quad T_s[\rho] = \sum_{i=1}^{N} \langle \phi_i | -\frac{1}{2}\nabla^2 | \phi_i \rangle, \tag{1.32}$$

where the single particle orbitals $\phi_i(\mathbf{r})$ are obtained by solving the KS equation

$$\hat{H}_{KS}\phi_i(\mathbf{r}) = \varepsilon_i \phi_i(\mathbf{r}). \tag{1.33}$$

The universal density functional of Eq. 1.25 can be rewritten as follows

$$F[\rho] = T_s[\rho] + E_H[\rho] + E_{xc}[\rho], \tag{1.34}$$

where $E_H[\rho] = \frac{1}{2} \int \int \frac{\rho(\mathbf{r})\rho(\mathbf{r}')}{|\mathbf{r}-\mathbf{r}'|} d\mathbf{r} d\mathbf{r}'$ is the classical part of the electron-electron interaction or the Hartree energy and the term E_{xc} contains the Pauli and Coulomb correlation and the ignored kinetic correlation in $T_s[\rho]$. We finally obtain the KS total energy functional,

$$E_{KS}[\rho] = T_s[\rho] + \int \rho(\mathbf{r})v_{\text{ext}}(\mathbf{r})d\mathbf{r} + E_H[\rho] + E_{xc}[\rho]. \tag{1.35}$$

The Kohn-Sham potential is determined by minimizing the KS energy functional w.r.t. density under the constraint of the density integrates to the N electrons,

$$\frac{\delta}{\delta\rho(\mathbf{r})}\left\{ E_{KS}[\rho] - \mu \int \rho(\mathbf{r})d\mathbf{r} \right\} = 0. \tag{1.36}$$

From the above equation, we obtain the following equation for the minimizing ground state density

$$\frac{\delta T_s[\rho]}{\delta\rho(\mathbf{r})} + v_{\text{ext}}(\mathbf{r}) + \int \frac{\rho(\mathbf{r}')}{|\mathbf{r}-\mathbf{r}'|}d\mathbf{r}' + \frac{\delta E_{xc}}{\delta\rho(\mathbf{r})} = \mu. \tag{1.37}$$

The effective KS potential v_{KS} will be

$$v_{KS}(\mathbf{r}) = v_{ext}(\mathbf{r}) + v_H(\mathbf{r}) + v_{xc}(\mathbf{r}),\qquad(1.38)$$

where $v_H(\mathbf{r}) = \int \frac{\rho(\mathbf{r}')}{|\mathbf{r}-\mathbf{r}'|}d\mathbf{r}'$ and $v_{xc}(\mathbf{r}) = \frac{\delta E_{xc}}{\delta\rho(\mathbf{r})}$ are the Hartree and exchange-correlation (XC) potential respectively. The KS equation should be solved self-consistently and a flowchart for the solution is shown in Fig. 1.1. The XC energy can be written as the sum
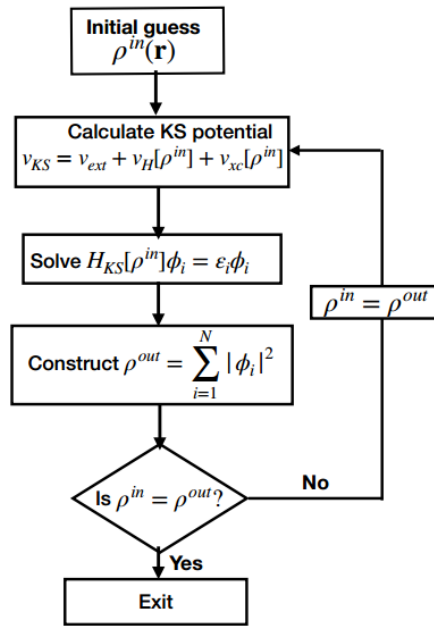
Figure 1.1: Flowchart for the iterative solution of the KS equation.

of exchange and correlation terms independently:

$$E_{xc}[\rho] = E_x[\rho] + E_c[\rho],\qquad(1.39)$$

where $E_x[\rho]$ and $E_c[\rho]$ are defined as[13]

$$E_x[\rho] = \langle\Phi_{\min}[\rho]|\hat{V}_{ee}|\Phi_{\min}[\rho]\rangle - E_H[\rho],\qquad(1.40)$$

$$E_c[\rho] = \langle\Psi_{\min}[\rho]|\hat{T} + \hat{V}_{ee}|\Psi_{\min}[\rho]\rangle - \langle\Phi_{\min}[\rho]|\hat{T} + \hat{V}_{ee}|\Phi_{\min}[\rho]\rangle.\qquad(1.41)$$

Here, $\Psi_{\text{min}}[\rho]$ minimizes the $\langle \hat{T} + \hat{V}_{\text{ee}} \rangle$ and $\Phi_{\text{min}}[\rho]$ minimizes $\langle \hat{T} \rangle$ and both yield same density ρ.

The main advantage of the KS approach is that through $T_{\text{s}}[\rho]$ it captures a large part of the total kinetic energy which is responsible for the density oscillations of the shell structure. On the other hand, it is more convenient to approximate $E_{\text{xc}}[\rho]$ using local or semilocal quantities rather than $T[\rho]$. In the next section, we will discuss about various approximations to the XC energy term for practical calculations.

1.5 Exchange-Correlation Functionals

It is necessary to know the form of XC energy functional for the practical use of the KS equation. However, the exact form of E_{xc} is not known till date. Thus, since the advent of DFT various types of approximations for E_{xc} have been used for practical calculations. Proposed XC functionals are categorized as different rungs of a Jacob's ladder[14] depending upon the ingredients used as shown in Fig. 1.2. Furthermore, the XC functionals can be divided into non-empirical which are proposed by satisfying some physical rules, and empirical ones which are proposed by fitting to known atomic or molecular properties. Next, we briefly describe the rungs of the Jacob's ladder to introduce some of the most widely used XC functionals which also have been used later in this thesis for studying different properties of solid-state and molecular systems.

Local Density Approximation (LDA) : In this approximation, a real inhomogeneous system is divided into infinitesimal volumes and within each infinitesimal volume, the density is taken to be uniform. The XC energy for each volume can be calculated using the XC energy for the uniform electron gas at that density and the total XC energy for the system can be written as

$$E_{\text{xc}}^{\text{LDA}} = \int \rho(\mathbf{r}) \varepsilon_{\text{xc}}^{\text{unif}}(\rho(\mathbf{r})) d\mathbf{r}, \tag{1.42}$$
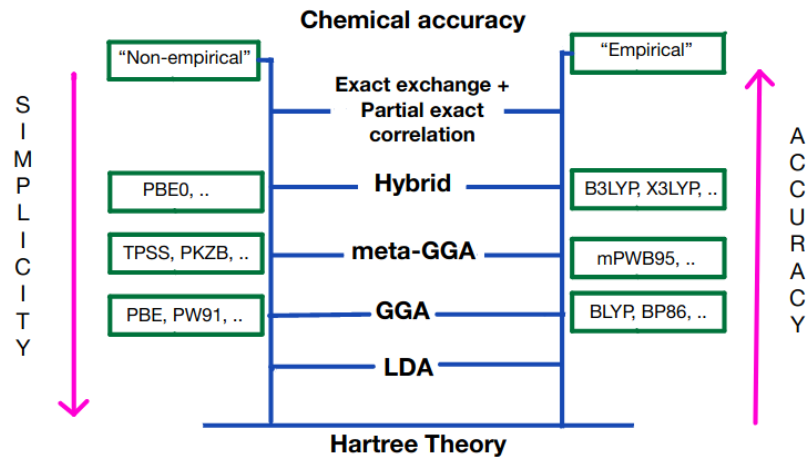
Figure 1.2: Schematic representation of the Jacob's ladder of the exchange-correlation functional approximations.

where $\varepsilon_{\text{xc}}^{\text{unif}}(\rho(\mathbf{r}))$ is the XC energy density for the interacting electron gas of density $\rho(\mathbf{r})$. The analytical form of the exchange energy is known in this case and given by[13,15]

$$E_{\text{x}}^{\text{LDA}} = -\frac{3}{4}\left(\frac{3}{\pi}\right)^{1/3}\int\rho(\mathbf{r})^{4/3}d\mathbf{r}. \tag{1.43}$$

However, there is no simple form available for the correlation energy and generally obtained by analysis and interpolation of highly accurate quantum Monte-Carlo simulations of the uniform electron gas.[16] Some of the popularly used LDA functionals are the Vosko-Wilk-Nusair (VWN),[17] Perdew-Zunger (PZ)[18] and Perdew-Wang (PW).[19]

The LDA shows good performance for various properties of solid-state systems such as equilibrium structures, vibrational frequencies etc.. LDA works remarkably well for metallic systems. A possible explanation for this success can be related to the error cancellation between the exchange and correlation energies in LDA. Typically, LDA overestimates the exchange and underestimates the correlation energies for real systems and as a result of which it gives good values of $E_{\text{xc}}^{\text{LDA}}$. This error cancellation appears because the LDA satisfies the exact sum rule[20,21] of XC energy.

However, LDA underestimates the lattice constants by $2-3\%$,[22] overestimates the cohesive energies by $15-20\%$[23] for solids and overestimates the atomization energies of

molecules by $\sim 20\%$.[24] LDA gives a very large error for weakly bonded system where Van der Waals interaction is dominant.

Generalized Gradient Approximation (GGA) : The first step to improve the performance of LDA is to include the gradient of density ($\nabla \rho(\mathbf{r})$) into the XC functional in order to capture the varying electron densities of many materials. The earlier attempt was called the gradient-expansion approximation (GEA), where the gradient correction terms in powers of $\nabla \rho(\mathbf{r})$, $|\nabla \rho(\mathbf{r})|^2$, $\nabla^2 \rho(\mathbf{r})$, etc. are added to LDA. However in reality the lowest order gradient correction deteriorates the LDA result for most of the cases.[25] Also, it is very difficult to calculate the higher-order correction terms.

After the failure of GEA, it was found that one could write the expression of XC functional as a more general function of $\rho(\mathbf{r})$ and $\nabla \rho(\mathbf{r})$ and the general form of such functional can be written as

$$E_{\text{xc}}^{\text{GGA}} = \int f_{\text{xc}}^{\text{GGA}}(\rho(\mathbf{r}), \nabla \rho(\mathbf{r})) d\mathbf{r}. \tag{1.44}$$

The functional form of f_{xc}^{GGA} is taken such that it can capture the correction to the LDA XC energy while following the exact sum rules. The exchange energy functional within GGA takes the form

$$E_{\text{x}}^{\text{GGA}} = \int \rho(\mathbf{r}) \varepsilon_{\text{x}}^{\text{unif}}(\rho(\mathbf{r})) F_{\text{x}}^{\text{GGA}}(s) d\mathbf{r}, \tag{1.45}$$

where $F_x^{GGA}(s)$ is the exchange enhancement factor which determines the enhanced exchange energy over the LDA for a given density and 's' is the dimensionless reduced density gradient

$$s = \frac{|\nabla \rho(\mathbf{r})|}{2 \left(3\pi^2\right)^{1/3} \rho(\mathbf{r})^{4/3}}. \tag{1.46}$$

The functional form of GGA correlation energy $E_{\text{c}}^{\text{GGA}}$ is expressed as a complex function of density gradient and relative spin polarization. Some widely used GGA functionals are PBE,[26] PW91,[27] LYP[28] and AM05.[29]

Normally GGAs improve the LDA results but this is not always the case. GGAs im-

prove binding energies, atomic energies, and dynamical properties of water, ice, and water clusters[30] over the LDA results. However, lattice constants of solids are typically overestimated by GGAs. A particularly problematic situation is that self-interaction present in the Hartree term is not compensated satisfactorily in the GGA functionals.

meta-GGA : The next step towards improving the performance of GGA is to consider the fourth-order gradient expansion of the exchange and correlation energy. This was first done in 1999 by constructing a meta-GGA that uses kinetic energy density $\left(\tau(\mathbf{r}) = \sum_i |\nabla \phi_i(\mathbf{r})|^2\right)$ or the Laplacian of density $(\nabla^2 \rho(\mathbf{r}))$ as an additional semilocal information.[31] Meta-GGA functionals improve results over GGA by satisfying other known constraints which are missing in the GGA level and at the same time these functionals retain the good formal properties of the GGAs. In general meta-GGA exchange functionals are expressed as,

$$E_{\mathrm{x}}^{\mathrm{MGGA}} = \int \rho(\mathbf{r}) \varepsilon_{\mathrm{x}}^{\mathrm{unif}}(\rho(\mathbf{r})) F_{\mathrm{x}}^{\mathrm{MGGA}}(s, \alpha) d\mathbf{r}, \qquad (1.47)$$

where s is defined in Eq. 1.46 and $\alpha = \frac{\tau - \tau^w}{\tau^{unif}}$ with $\tau^w = \frac{|\nabla \rho(\mathbf{r})|^2}{8\rho(\mathbf{r})}$ is the von Weizsäcker kinetic energy density and $\tau^{unif} = \frac{3}{10}\left(3\pi^2\right)^{2/3} \rho^{5/3}$ is the uniform kinetic energy density. MGGA correlation energy E_c^{MGGA} can be expressed as a complex functional of the density gradient, relative spin polarization and spin-polarized kinetic energy density. We can construct a one-electron self-interaction[18] free correlation energy functional at the meta-GGA level i.e.

$$E_c[\rho] = 0 \quad \text{for any density such that } \int \rho(\mathbf{r}) d\mathbf{r} = 1. \qquad (1.48)$$

Some of the widely used meta-GGA functionals are PKZB,[31] TPSS,[32] TM,[33] and SCAN.[34] The TM functional is developed by modelling the exchange hole using density matrix expansion under a generalized coordinate transformation. The SCAN density functional satisfies seventeen known exact constraints for the exchange and correlation. These functionals are very accurate for predicting lattice constants, cohesive energies, and frequencies of the solid-state systems and at the same time give accurate atomization energies of molecules.[32,34]

The most important unresolved issue at the meta-GGA level is the incomplete cancellation of the self-interaction by the exchange term. Also, meta-GGA functionals do not include the static correlation and van der Waals interaction.

Hybrid Functional : The observation that the trends of semilocal approximations are opposite to those of the HF approximation initiates the development of approximations that mix these two approaches. However, the concept of hybrid functionals can be derived using the "adiabatic connection"[35] for the XC energy of the DFT, which is expressed in the following way

$$E_{\text{xc}} = \int_0^1 U_{\text{xc}}^\lambda d\lambda, \tag{1.49}$$

where λ is the parameter for the interelectronic coupling strength which switches on the Coulomb interaction between the electrons and U_{xc}^λ is the potential energy of the XC at a particular value of λ. The Eq. 1.49 connects the non-interacting Kohn-Sham system for $\lambda = 0$ to the fully interacting system for $\lambda = 1$ through a series of partially interacting systems in between $0 < \lambda < 1$ and all of the systems have the same density as the interacting one. As the non-interacting limit ($\lambda = 0$) is described by the HF exchange, we might expect an important role of the exact exchange for the improvement of the XC functionals. Thus in the hybrid functionals, semilocal XC approximation is mixed with the HF exchange in the following way

$$E_{\text{xc}}^{\text{hyb}} = \alpha E_{\text{x}}^{\text{HF}} + (1 - \alpha) E_{\text{x}}^{\text{DFT}} + E_c^{\text{DFT}}. \tag{1.50}$$

The most popular and widely used hybrid functional within the quantum chemistry community is the B3LYP[36] which uses three parameters for controlling the mixing of the HF exchange and the DFT XC and the functional form can be written as

$$E_{\text{xc}}^{\text{B3LYP}} = E_{\text{xc}}^{\text{LDA}} + \alpha_0 (E_{\text{x}}^{\text{HF}} - E_{\text{x}}^{\text{LDA}}) + \alpha_{\text{x}} \Delta E_{\text{x}}^{\text{B88}} + \alpha_{\text{c}} \Delta E_{\text{c}}^{\text{LYP}}, \tag{1.51}$$

where $\alpha_0 = 0.20$, $\alpha_{\text{x}} = 0.72$ and $\alpha_{\text{c}} = 0.81$ are determined empirically by fitting to experimental data, $\Delta E_{\text{x}}^{\text{B88}}$ and $\Delta E_{\text{c}}^{\text{LYP}}$ are the gradient corrections for the exchange and correlation respectively.[28,37] In the case of PBE0[38] functional, PBE GGA is used in Eq. 1.50.

In this case, the mixing coefficient α is taken to be 0.25 from the perturbative calculation.[39] These functionals improve the performance over semilocal functionals for several molecular properties.[40,41]

The hybrid functionals discussed till now are called the global hybrids as the mixing coefficient is constant over the whole range. However, there are some hybrid functionals which use position dependent mixing to further reduce the self-interaction error. These are called local hybrid functionals[42,43] which can model two-centre, three-electron symmetric radicals accurately.

There are another class of hybrid functionals where the HF exchange and the semilocal XC functionals are mixed using the range separation of the Coulomb interaction operator. These are called range separated functionals and popular examples of this type of functionals are the CAM-B3LYP,[44] HSE06,[45] LC-ωPBE,[46] LC-ωPBEh[47] etc.. These functionals will be discussed in great detail in the second chapter.

Besides these four rungs of the Jacob's ladder, there are other XC functionals in the higher rungs with increasing complexity. Although, it is expected to get improved results by climbing higher on Jacob's ladder but it is not always the case.[23] Most of the proposed XC functionals have been implemented in the library of exchange-correlation functional (LIBXC)[48] which can be interfaced with several first-principle codes for the DFT calculations.

1.6 Designing Exchange-Correlation Functional via the Exchange-Correlation Hole

In the previous section, we have introduced different levels of approximations for the XC energy functional. In this section, we will describe how one can derive XC functional using the concept of XC hole. By combining Eqs. 1.39, 1.40, and 1.41 we can express the XC energy functional as

$$E_{\text{xc}}[\rho] = (V_{\text{ee}}[\rho] - E_{\text{H}}[\rho]) + (T[\rho] - T_{\text{s}}[\rho]). \tag{1.52}$$

The first part of the contribution is associated with the second-order reduced density matrix and the second one with the first-order reduced density matrix. A brief description of the reduced density matrix is given in Appendix A. Using the adiabatic connection theorem, we can derive a single expression for the XC energy functional in terms of the XC hole. Let's define the universal functional for any intermediate interaction strength as

$$F_\lambda[\rho(\mathbf{r})] = \min_{\psi \to \rho} \langle \psi | \hat{T} + \lambda \hat{V}_{ee} | \psi \rangle. \tag{1.53}$$

Then Eq. 1.52 reduces to

$$E_{xc} = \int_0^1 \frac{\partial F_\lambda(\rho)}{\partial \rho} d\lambda - E_H(\rho). \tag{1.54}$$

Finally, inserting the value of $\frac{\partial F_\lambda(\rho)}{\partial \rho}$ in the above equation, we obtain[49]

$$E_{xc}[\rho] = \frac{1}{2} \int \int \frac{\rho(\mathbf{r})\rho_{xc}(\mathbf{r},\mathbf{r}')}{|\mathbf{r}-\mathbf{r}'|} d\mathbf{r}d\mathbf{r}'. \tag{1.55}$$

The XC hole ρ_{xc} represents a fictitious charge reduction due to the exchange and correlation effects. In other words, it represents that the presence of an electron at $\mathbf{r}$ reduces the probability of getting another electron at $\mathbf{r}'$ in the vicinity of $\mathbf{r}$. The XC hole follows the following sum rule[20] -

$$\int \rho_{xc}(\mathbf{r},\mathbf{r}')d\mathbf{r}' = -1. \tag{1.56}$$

This signifies that the XC hole consists of exactly one displaced electron. We can disintegrate exchange and correlation contributions from ρ_{xc}. We can define the exchange hole as

$$\rho_x(\mathbf{r},\mathbf{r}') = -\frac{1}{2} \frac{|\rho_1(\mathbf{r},\mathbf{r}')|^2}{\rho(\mathbf{r})}, \tag{1.57}$$

where $\rho_1(\mathbf{r},\mathbf{r}')$ is the first-order reduced density matrix. Using this exchange energy will be expressed as

$$E_x = \frac{1}{2} \int \int \frac{\rho(\mathbf{r})\rho_x(\mathbf{r},\mathbf{r}')}{|\mathbf{r}-\mathbf{r}'|} d\mathbf{r}d\mathbf{r}'. \tag{1.58}$$

and the exchange hole satisfies

$$\int \rho_x(\mathbf{r}, \mathbf{r}') d\mathbf{r}' = -1. \tag{1.59}$$

Then the correlation hole must integrate to zero, $\int \rho_c(\mathbf{r}, \mathbf{r}') d\mathbf{r}' = 0$ and the correlation energy is

$$E_c = \frac{1}{2} \int \int \frac{\rho(\mathbf{r}) \rho_c(\mathbf{r}, \mathbf{r}')}{|\mathbf{r} - \mathbf{r}'|} d\mathbf{r} d\mathbf{r}'. \tag{1.60}$$

From the above discussion, it is clear that the exchange energy corresponds to the interaction energy of the electrons with a charge distribution of one unit charge and the correlation energy equals the interaction of the electrons with a neutral charge distribution. We will construct exchange energy functional using Eq. 1.58 which will be discussed in detail in the third & fourth chapter.

1.7 Important Properties Of The Exchange-Correlation Functional

In the previous section, we have discussed about the exact expression of the XC energy functional in terms of the XC hole. But the exact form of the exchange hole is known only for the homogeneous electron gas. Hence, for the calculation purpose, we need to approximate the form of the XC energy functional. Although the exact form of the XC functional is unknown, many features of the exact $E_{xc}[\rho]$ are known. In general non-empirical XC functionals are designed to satisfy as many exact constraints as possible.

1.7.1 Scaling Properties

In uniform density scaling, a scaling factor γ is introduced which changes the length scale of the density, either stretches out ($\gamma < 1$) or squeezes in ($\gamma > 1$), while maintaining the

normalization. Under this condition, density scales as

$$\rho_\gamma(\mathbf{r}) = \gamma^3 \rho(\gamma \mathbf{r}), \tag{1.61}$$

where the prefactor is chosen to maintain the normalization-

$$N = \int \rho_\gamma(\mathbf{r}) d\mathbf{r} = \int \gamma^3 \rho(\gamma \mathbf{r}) d\mathbf{r} = \int \rho(\mathbf{r}') d\mathbf{r}'. \tag{1.62}$$

Scaling properties of the exact exchange functional is given as[50]

$$E_\mathrm{x}[\rho_\gamma] = \gamma E_\mathrm{x}[\rho]. \tag{1.63}$$

However, the exact scaling relation for the correlation energy is not known. It follows the following inequalities[50]

$$
\begin{aligned}
E_\mathrm{c}[\rho_\gamma] &> \gamma E_\mathrm{c}[\rho] \quad \text{for} \quad \gamma > 1 \\
E_\mathrm{c}[\rho_\gamma] &< \gamma E_\mathrm{c}[\rho] \quad \text{for} \quad \gamma < 1
\end{aligned}
\tag{1.64}
$$

1.7.2   One-Electron Limit

In the case of a one-electron system, the exact exchange energy should cancel the classical Coulomb interaction energy due to the self-interaction present in both the terms. As exchange and Hartree term cancel each other, correlation energy must be zero in this case to avoid any spurious self-interaction error. It is very hard to follow these condition exactly when we approximate XC functional in terms of density. Our XC functional designing strategies would be to follow these conditions as closely as possible. Thus for any one-electron density $\rho^{(1)}$,

$$
\begin{aligned}
E_\mathrm{x}[\rho^{(1)}] &= -E_\mathrm{H}[\rho^{(1)}], \\
E_\mathrm{c}[\rho^{(1)}] &= 0.
\end{aligned}
\tag{1.65}
$$

1.7.3   The Lieb-Oxford Bound

Exact XC energy functional satisfies the following inequalities[51]

$$E_{\text{x}}[\rho] \geq E_{\text{xc}}[\rho] \geq -1.679 \int \rho^{4/3}(\mathbf{r})d\mathbf{r}. \qquad (1.66)$$

The above inequality will be satisfied if the enhancement factor defined in Eq. 1.45 satisfy the following relation[26]

$$F_{\text{x}} \leq 1.804. \qquad (1.67)$$

The Lieb-Oxford bound is satisfied by some of the popular semilocal functionals including PBE, PKZB, and TPSS. In the case of two-electron systems, where $\alpha = 0$, an optimal lower bound on exchange was derived[52] for the meta-GGA functional and it is satisfied for all possible densities if and only if

$$F_{\text{x}}(s, \alpha = 0) \leq 1.174. \qquad (1.68)$$

It is also conjectured that for any general α the enhancement factor of the meta-GGA functional should follow the following relation[52]

$$F_{\text{x}}(s, \alpha) \leq F_{\text{x}}(s, \alpha = 0) \leq 1.174 \qquad (1.69)$$

This tight lower bound is satisfied by the MVS[53] and MGGAC[54] meta-GGA XC functionals. This condition will be used in chapter four to develop meta-GGA exchange energy functional.

1.7.4   Spin Scaling Relations

The total density of a system can be written as a sum of up and down spin densities i.e.

$$\rho(\mathbf{r}) = \rho_{\uparrow}(\mathbf{r}) + \rho_{\downarrow}(\mathbf{r}). \qquad (1.70)$$

Since the exchange is only allowed between like spins, exchange energy functional can be decomposed in terms of up and down spin densities in the following way,

$$E_{\mathrm{x}}[\rho_\uparrow, \rho_\downarrow] = \frac{1}{2}\left(E_{\mathrm{x}}[2\rho_\uparrow] + E_{\mathrm{x}}[2\rho_\downarrow]\right). \tag{1.71}$$

By using the above formula any spin unpolarized exchange energy functional can be transformed into its spin-polarized form. This is very useful for calculating the properties of magnetic systems. However, there is no simple spin scaling relation for the correlation energy functional.

To conclude, in this chapter we have discussed a brief overview of the density functional method including its practical applications for which we need exchange-correlation functional. As the exact XC functional is unknown, for practical calculations we need to approximate the same. Then, we have presented different levels of approximation for the XC term in terms of the Jacob's ladder of DFT. Next, we have provided some exact constraints of the XC functional which are useful for functional development. In this thesis, we will discuss about new developments of the XC functionals both in the semilocal and hybrid level and the application of those developed functionals for different solid-state and molecular systems.

1.8   Outline of the Thesis

In the second chapter, we will develop a long-range corrected density functional using semilocal exchange hole. This chapter will have a rigorous theoretical description of the range-separated density functional from the adiabatic connection theorem. The developed functional will be applied to calculate the properties of various molecular test sets and benchmarked by comparing with other popularly known range-separated functional.

In the third chapter, a semilocal density-functional will be developed by modelling the exchange hole using cuspless hydrogen density as a model for the band gap of solid-state systems. The proposed functional will be applied to calculate band gap of narrow and moderate band gap semiconductors and layered materials.

In the fourth chapter, we will extend the method of the second chapter and propose a meta-GGA exchange functional depending only on the Pauli kinetic energy density. In combination with a GGA correlation, the proposed functional will be applied to calculate the properties of various thermochemical test-sets, bulk solids, and surfaces.

In the fifth chapter, we will apply the developed functional in the fourth chapter for the case of phase stability of FeS_2, TiO_2 and MnO_2.

Chapter 2

Long-range Corrected Hybrid Density Functional Using Semilocal Exchange Hole

2.1 Introduction

The semilocal XC functionals described in the previous chapter have an excellent accuracy to computational cost ratio and are mostly easy to implement. These functionals are very successful in predicting atomization energies,[55,56,57,58] lattice constants,[22,23,59] equilibrium bond lengths,[58,60] cohesive energies,[23,59] and surface properties.[59] However, DFT with these class of functionals exhibits noticeable failures including underestimation of reaction barriers,[61] instability of anions,[62,63] incorrect dissociation limit of molecules,[64,65] absence of Rydberg states[66] and wrong prediction of oscillator strength.[67,68,69]

The aforementioned shortcomings of the semilocal functionals are linked with their failures to deal with the self-interaction error (SIE), also known as delocalization error. For one-electron systems, the Hartree energy should be cancelled by the exact XC energy. On the contrary, the Hartree-Fock (HF) theory correctly follows this constraint and hence gives correct dissociation limit for one electron system. For many-electron case, an

XC functional is said to be one-electron self-interaction free if it satisfies the following condition[18]-

$$E_{xc}[\rho_j] + E_H[\rho_j] = 0, \tag{2.1}$$

where $\rho_j = \sum |\psi_j|^2$ is the one-electron density. However, Eq. 2.1 is puzzling in the case of the many-electron system as we cannot always identify orbital densities with electrons. An XC functional is many-electron self-interaction free if it satisfies the piecewise linearity[70] condition of total energy $E(N)$ as a function of particle number N

$$E(N) = (1 - \varepsilon)E(N_0) + \varepsilon E(N_0 + 1), \tag{2.2}$$

where $E(N_0)$ and $E(N_0 + 1)$ are the ground-state energies of the N_0 and $N_0 + 1$ electron systems respectively and $0 \le \varepsilon \le 1$. Although semilocal functionals give a good estimate of ground-state energies of the system with integer particle number, but give too low energies for fractionally occupied systems. This gives rise to deviation from the linearity condition and we get a convex curve for semilocal functionals and on the other hand, the HF theory gives the energy curve to be concave.

It is expected that self-interaction error is connected to the XC potential. If an electron is removed to infinity from a finite neutral-charge system, it will feel the hole of charge one that is left behind and as a result the potential felt by that electron should have $-1/r$ asymptote.[71]

$$\lim_{|\mathbf{r}| \to \infty} V_{xc}(\mathbf{r}) = -\frac{1}{|\mathbf{r}|}. \tag{2.3}$$

The XC potential coming from semilocal functionals shows incorrect asymptotic behaviour and decays faster than $-1/r$. Missing non-locality[72] of the semilocal XC functionals is essential to describe barrier heights, long-range charge transfer and dissociation limit of the molecules. One of the possible solutions to include the missing non-locality is to consider the global hybrid functional defined in the previous chapter where a fraction of HF exchange is mixed with semilocal functional. Although B3LYP[36] and other[73,74] popular hybrid XC functionals give satisfactory results in most of the cases but still, they have accuracy issues in describing dissociation energy and phenomena involving fractional oc-

cupation number. For global hybrids, XC potential decays asymptotically as $-c/r$, where c is the fraction of mixed Hartree-Fock exchange but this violates the condition stated in Eq. 2.3. Another possible way to include non-locality and at the same time follow the Eq. 2.3, is to use the range-separation technique[66,75] of the Coulomb interaction operator. In this scheme, exact HF exchange is used for long-range interaction and semilocal DFT is adopted for the short-range interaction.

Usually, range-separated functionals are designed from the spherically averaged exchange holes[33,76] or the holes constructed from the reverse engineering technique.[77,78] The CAM-B3LYP functional is designed employing LDA exchange hole and including the inhomogeneity through the modification of Thomas-Fermi wave-vector.[44] Following this, the HSE06,[45] LC-ωPBE,[46] and LC-ωPBEh[47] functionals are designed using the PBE exchange hole. In this chapter, we construct a long-range corrected density functional using Tao-Mo[33] semilocal exchange hole. First, we briefly describe the theoretical framework of the range-separated functional. The proposed form of the long-range corrected functional is given in section 2.3. Finally, computational details and results for different benchmarking test sets are discussed in the subsequent sections.

2.2   Theoretical Background

In range-separated density functional theory, Coulomb interaction $V_{ee}(\mathbf{r}_i, \mathbf{r}_j) = \frac{1}{r_{ij}}$ between two electrons at $\mathbf{r}_i$ and $\mathbf{r}_j$ can be splitted into a short-range (SR) and long-range (LR) parts in the following way

$$\frac{1}{r_{ij}} = \underbrace{\frac{1 - f(r_{ij})}{r_{ij}}}_{SR} + \underbrace{\frac{f(r_{ij})}{r_{ij}}}_{LR}. \tag{2.4}$$

where $f(r_{ij})$ is some smooth range-separation function. The most suitable form for the function 'f' from both physical and computational point of view is $f(r_{ij}) = \mathrm{erf}(\mu r_{ij})$, where μ is a parameter. However other forms[79,80] of the function 'f' have been used in the literature. For this choice, the first term of the equation goes to zero as $r_{ij} \to \infty$

and the second term goes to $2\mu/\sqrt{\pi}$ for $r_{ij} \to 0$. Parameter μ can be regarded as a cut-off between long-range and short-range parts. For interelectronic distances larger than the cut-off radius ($r_c \approx 1/\mu$), LR part of the interaction (V_{ee}^{LR}) reproduces long-range Coulomb tail as shown in Fig. 2.1. The most natural form of these functionals, also called
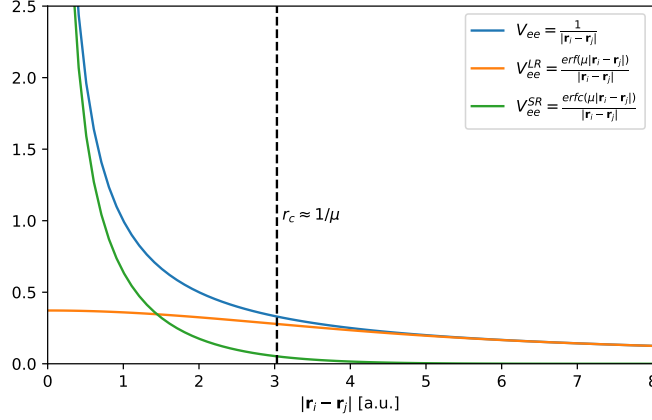
Figure 2.1: Coulomb interaction (V_{ee}) and its long-range (V_{ee}^{LR}) and short-range (V_{ee}^{SR}) parts versus electron-electron distance $|\boldsymbol{r}_i - \boldsymbol{r}_j|$ are shown for range separation parameter $\mu = 0.33$ in a.u.. $r_c \approx 1/\mu$ is the cut-off radius for the range of interaction.

as Coulomb-attenuating method (CAM)[75] functional defined as

$$\frac{1}{r_{ij}} = \underbrace{\frac{1 - [\alpha + \beta f(r_{ij})]}{r_{ij}}}_{SR} + \underbrace{\frac{\alpha + \beta f(r_{ij})}{r_{ij}}}_{LR}, \tag{2.5}$$

where α is the fraction of exact HF exchange and $\alpha + \beta$ is the fraction of LR HF exchange.[81] The parameters α and β should follow the relations $0 \leq \alpha + \beta \leq 1, 0 \leq \alpha \leq 1, 0 \leq \beta \leq 1$. Mixing DFT and HF in this way gives rise to different global hybrids and long-range corrected functionals as limiting cases depend on the values of α and β.

Till now, range-separated functionals have been introduced from the empirical background. However, these functionals can be derived from the adiabatic connection theorem. Let's assume there exists a one parameter smooth representation of electron-electron Coulomb interaction operator, $\hat{V}_{ee} \to \hat{V}_{ee}^{\mu}$ for $0 \leq \mu \leq \infty$ such that $\hat{V}_{ee}^{0} = 0$ and $\hat{V}_{ee}^{\infty} = \hat{V}_{ee}$.

The universal functional for this kind of interaction is written as

$$F^{\mu}[\rho] = \min_{\psi^{\mu} \to \rho} \langle \psi^{\mu} | \hat{T} + \hat{V}_{ee}^{\mu} | \psi^{\mu} \rangle. \tag{2.6}$$

Then by construction $F^0 = T^0$ for the Kohn-Sham system and $F^{\infty} = F$ for real interacting system. The XC functional from the adiabatic connection theorem[82] is given by

$$\begin{aligned} E_{xc}[\rho] &= \int_0^{\infty} \frac{dF^{\mu'}}{d\mu'} d\mu' - E_{H}[\rho] \\ &= \int_0^{\infty} \langle \psi^{\mu'} | \frac{d\hat{V}_{ee}^{\mu'}}{d\mu'} | \psi^{\mu'} \rangle d\mu' - E_{H}[\rho]. \end{aligned} \tag{2.7}$$

Given a value of parameter μ, if we assume the wavefunction in Eq. 2.7 to be Slater determinant Φ for $\mu' < \mu$ and full interacting wavefunction for $\mu' > \mu$ then the above equation reduces to

$$E_{xc}[\rho] = E_{x,HF}^{\mu,LR}[\rho] + \underbrace{\left[\langle \psi | \hat{V}_{ee} - \hat{V}_{ee}^{\mu} | \psi \rangle - \frac{1}{2} \int V_{ee}^{SR} \rho(\mathbf{r}) \rho(\mathbf{r}') d^3\mathbf{r} d^3\mathbf{r}' \right]}_{E_{xc}^{\mu,SR}}. \tag{2.8}$$

To sum up, the full energy functional in range-separated hybrid scheme becomes

$$E_{RSH}[\rho] = T^0[\rho] + V_{ext}[\rho] + E_{H}[\rho] + E_{x,HF}^{\mu,LR}[\rho] + E_{xc}^{\mu,SR}[\rho]. \tag{2.9}$$

After applying the range-separation only on the exchange part, the above equation can be written as

$$E_{RSH}[\rho] = T^0[\rho] + V_{ext}[\rho] + E_{H}[\rho] + E_{x,HF}^{\mu,LR}[\rho] + E_{x}^{\mu,SR}[\rho] + E_{c}[\rho]. \tag{2.10}$$

The functional obtained above is called the long-range corrected (LC) functional. In Eq. 2.10, the form of the long-range part of the exchange interaction is

$$E_{x,HF}^{\mu,LR}[\rho] = -\frac{1}{2} \sum_{\sigma} \sum_{i,j}^{occ} \int \int \phi_{i\sigma}^*(\mathbf{r}_i) \phi_{j\sigma}^*(\mathbf{r}_j) \frac{\mathrm{erf}(\mu r_{ij})}{r_{ij}} \phi_{j\sigma}(\mathbf{r}_i) \phi_{i\sigma}(\mathbf{r}_j) d\mathbf{r_i} d\mathbf{r_j}, \tag{2.11}$$

where $\phi_{i\sigma}$ is the ith σ-spin molecular orbital and the short-range exchange functional is given as

$$E_x^{\mu,\text{SR}}[\rho] = \frac{1}{2}\int\int \frac{\rho(\mathbf{r_i})(1-\text{erf}(\mu r_{ij}))\rho_x(\mathbf{r_i},\mathbf{r_j})}{r_{ij}}d\mathbf{r_i}d\mathbf{r_j}, \qquad (2.12)$$

where $\rho_x(\mathbf{r_i},\mathbf{r_j}) = -|\rho_1(\mathbf{r_i},\mathbf{r_j})|^2/2\rho(\mathbf{r_i})$ is the exchange hole and $\rho_1(\mathbf{r_i},\mathbf{r_j})$ be the first order reduced density matrix. Therefore knowing the exchange hole, the short-range part of the exchange functional can be designed.

2.3   Proposed Long-range Corrected Functional

We design a long-range corrected functional using the recently proposed Tao-Mo[33] semilocal exchange hole. This exchange hole is derived from density matrix expansion (DME) making use of the fact that the exchange hole can be made localized under a generalized coordinate transformation. Tao-Mo semilocal exchange hole at a reference point $\mathbf{r}$ due to another electron at $\mathbf{r}'$ has the following form

$$\rho_x(\mathbf{r},\mathbf{u}) = -\frac{9\rho(\mathbf{r})}{2}\frac{j_1^2(ku)}{k^2u^2} - \frac{105 j_1(ku)j_3(ku)}{k^4u^2}\mathscr{G} - \frac{3675 j_3^2(ku)}{8k^6u^4}\mathscr{H}, \qquad (2.13)$$

where $\mathbf{u} = \mathbf{r}' - \mathbf{r}$, $\mathscr{G} = 3(\lambda^2 - \lambda + \frac{1}{2})(\tau - \tau_{unif} - \frac{|\nabla\rho(\mathbf{r})|^2}{72\rho(\mathbf{r})}) - (\tau - \tau_{unif}) + 7(2\lambda-1)^2\frac{|\nabla\rho(\mathbf{r})|^2}{18\rho(\mathbf{r})}$, $\mathscr{H} = (2\lambda-1)^2\frac{|\nabla\rho(\mathbf{r})|^2}{\rho(\mathbf{r})}$, τ is the Kohn-Sham kinetic energy density, $\tau_{unif} = \frac{3}{10}(3\pi^2)^{2/3}\rho^{5/3}$, λ is the parameter for the generalized coordinate transformation[83,84] and j_1, j_3 are the spherical Bessel functions of order one and three respectively. To take care the inhomogeneity in the system, the modified momentum vector k is defined as $k = fk_F$, where k_F is the Fermi momentum for the uniform electron gas. The inhomogeneity parameter[33] f is fixed using the sum rule of exchange hole by extrapolating its large and small gradient limit and is given by $f = [1 + 10(70y/27) + \beta y^2]^{1/10}$, where $y = (2\lambda-1)^2s^2$, $s = |\nabla\rho|/(2k_F\rho)$ and β is a parameter. This semilocal exchange hole has the following properties

(i) It correctly recovers the exchange hole of the uniform electron gas $\rho_x^{unif}(\mathbf{r},\mathbf{u}) = -\frac{9\rho(\mathbf{r})}{2}\frac{j_1^2(k_Fu)}{k_F^2u^2}$, which is the first term in equation 2.13.

(ii) It correctly reproduces the small u expansion of the exchange hole proposed by Becke.[76]

(iii) Exchange hole converge at large u limit such that the form of exchange energy can be evaluated without any numerical cutoff procedure.[85]

As prescribed by Tao-Mo,[33] the parameters λ and β are fixed from the condition of getting the exchange energy of the hydrogen atom and the enhancement factor to be smoothly increasing function of s in the iso-orbital region. This gives λ and β to be 0.6866 and 79.873 respectively. Using the exchange hole of Eq. 2.13, the short-range part of the exchange functional becomes

$$E_{\text{x}}^{\mu,\text{SR}}[\rho] = \frac{1}{2} \int \rho(\mathbf{r})(\mathscr{M} + \mathscr{N} + \mathscr{Q})d^3 r, \tag{2.14}$$

where

$$\mathscr{M} = -\frac{9\pi\rho(\mathbf{r})}{2k^2}\left[1 - \frac{8}{3}a\left\{\sqrt{\pi}\,\text{erf}\left(\frac{1}{2a}\right) + (2a - 4a^3)\exp\left(-\frac{1}{4a^2}\right)\right.\right.$$
$$\left.\left. -3a + 4a^3\right\}\right], \tag{2.15}$$

$$\mathscr{N} = -\frac{35\pi}{3k^4}\mathscr{G}\left[1 + 24a^2\left\{(20a^2 - 64a^4)\exp\left(-\frac{1}{4a^2}\right) - 3 - 36a^2 + 64a^4\right.\right.$$
$$\left.\left. +10a\sqrt{\pi}\,\text{erf}\left(\frac{1}{2a}\right)\right\}\right], \tag{2.16}$$

$$\mathscr{Q} = -\frac{245\pi}{48k^4}\mathscr{H}\left[1 + \frac{8}{7}a\left\{(-8a + 256a^3 - 576a^5 + 3840a^7 - 122880a^9)\exp\left(-\frac{1}{4a^2}\right)\right.\right.$$
$$\left.\left. +24a^3(-35 + 224a^2 - 1440a^4 + 5120a^6) + 2\sqrt{\pi}(-2 + 60a^2)\,\text{erf}\left(\frac{1}{2a}\right)\right\}\right], \tag{2.17}$$

and $a = \frac{\mu}{2k}$. Most of the previously proposed LC hybrid XC functionals employ system independent value for the screening parameter μ. However, there are some reports regarding the use of system-dependent screening parameter,[86,87] but those are computationally not efficient due to their non-trivial implementation. The value of the parameter μ for LC functionals generally lies between 0.25 to 0.40.[44,46,87,88,89,90,91,92] This parameter can be

optimized from a small test set of atomization energy of molecules[92] or vertical ionization potential of some molecule.[90,91] For the present case, the value of μ is chosen to be 0.33, analogous with the CAMB3LYP functional which gives balanced results for both thermo-chemistry and barrier heights. We use one electron self-interaction free LYP[28] correction with our proposed LC functional and we term it as LC-TMLYP.

2.4 Computational Details And Benchmark Test-sets

The newly proposed LC functional of Eq. 2.14 is implemented in the modified local version of NWChem-6.6.[93] All calculations have been performed self-consistently in NWChem. Spin polarized calculation has been done for open shell systems. The value of $\mu = 0.33$ is used for all parts of the code. A medium grid is used for the numerical evaluation of the exchange-correlation contribution to the density functional. The details of the basis set used in the calculations are discussed in the result section. In Table 2.1, we have shown the dataset used for benchmarking LC-TMLYP functional. The deviation from theoretical results from the reference values are reported as mean error (ME) and mean absolute error (MAE). To compare the results of LC-TMLYP, we consider the four other popularly known range-separated functionals HSE06,[45] CAM-B3LYP,[44] LC-ωPBE,[46] and LC-ωPBEh.[47]

2.5 Results

2.5.1 Total Energies of Atoms

The total energies of atoms up to Cl are computed for the functionals under investigation. The 6-311++G(3df,3pd) basis set is used for all atoms except He, for which aug-cc-pVQZ basis set is used. The comparison of calculated results using different functionals with the accurate non-relativistic reference values[96] is provided in Table 2.2. Overall, CAM-B3LYP has the smallest MAE and LC-ωPBEh gives the largest MAE for this test set. LC-TMLYP gives MAE 0f 0.14 Hartree, which is very close to the prediction of CAM-

Table 2.1: Summary of the test sets used for benchmarking calculations.

Database	Description	Ref.
AE17	17 atomic energies (H-Cl)	94
	Thermochemistry	
G2/97	148 atomization energies	95
IP13	13 ionization potentials	94
EA13	13 electron affinities	94
PA8	8 proton affinities	94
NCCE31	31 non-covalent interactions	94
πTC13	13 thermochemistry of π system	94
ABDE12	12 alkyl bond dissociation energies	94
ISOL6	6 isomerization energies	94
HC7	11 hydrocarbon chemistry	94
DC7	7 difficult cases	94
	Barrier Height	
HTBH38	38 hydrogen transfer barrier height	94
NHTBH38	38 non-hydrogen transfer barrier height	94

B3LYP. For the case of the total energy of H atom, LC-ωPBE has the largest deviation among the tested functionals. Any deviation of the total energy of H atom (one electron) from the reference value can be linked with the one-electron self-interaction error. There is a spurious one-electron self-interaction error of 0.006 Hartree for LC-ωPBE. LC-TMLYP and CAM-B3LYP have the lowest error of about 0.002 Hartree for this case.

2.5.2   Thermochemical Test Set

Atomization Energy:

Atomization energy of a molecule is defined as the difference between the total energy of the molecule and sum of the energy of its constituent free atoms, all measured at 0K. The atomization energies of 148 molecules for the G2/97[95] test set are calculated. The total energy is calculated using 6-311++G(3df,3pd) basis set and MP2(full)/6-31G* optimized geometry for each molecule. The calculated results are then compared with that of the CCSD(T) values,[97] which is assumed to be gold-standard in quantum chemistry. All the

Table 2.2: Total energies (Hartree) of atoms from H to Cl (AE17) test set.

Atom	Ref.	LC-TMLYP	CAM-B3LYP	LC-ωPBE	LC-ωPBEh	HSE06
H	-0.500	-0.498	-0.498	-0.506	-0.503	-0.504
He	-2.904	-2.904	-2.901	-2.904	-2.897	-2.902
Li	-7.478	-7.479	-7.470	-7.469	-7.468	-7.475
Be	-14.667	-14.659	-14.649	-14.637	-14.639	-14.647
B	-24.654	-24.650	-24.640	-24.624	-24.622	-24.631
C	-37.845	-37.846	-37.836	-37.816	-37.809	-37.819
N	-54.589	-54.592	-54.580	-54.559	-54.547	-54.558
O	-75.067	-75.082	-75.070	-75.038	-75.021	-75.034
F	-99.734	-99.755	-99.741	-99.698	-99.676	-99.691
Ne	-128.938	-128.958	-128.941	-128.887	-128.861	-128.877
Na	-162.255	-162.284	-162.266	-162.191	-162.176	-162.196
Mg	-200.053	-200.085	-200.071	-199.968	-199.964	-199.987
Al	-242.346	-242.378	-242.368	-242.251	-242.252	-242.275
Si	-289.359	-289.386	-289.380	-289.254	-289.255	-289.279
P	-341.259	-341.274	-341.274	-341.140	-341.141	-341.166
S	-398.110	-398.124	-398.130	-397.981	-397.981	-398.006
Cl	-460.148	-460.156	-460.170	-460.007	-460.006	-460.031
ME		-0.012	-0.004	0.057	0.064	0.049
MAE		0.014	0.012	0.058	0.064	0.049

range-separated functionals including LC-TMLYP are performing well in this case, giving MAE below 6 kcal/mol. Table 2.3 shows that the CAM-B3LYP has the lowest MAE in this case, followed by LC-TMLYP. The LC-ωPBEh gives the largest MAE among the functionals considered here.

Ionization Potential, Electron Affinity and Proton Affinity:

Ionization potential (IP) and electron affinity (EA) is defined as the difference in energy of the ion (cation for IP and anion for EA) and the corresponding neutral atom or molecule, all measured at 0 K. We calculate IP and EA for the IP13 and EA13 databases respectively with QCISD/MG3[98] level optimized geometry. Single point energy is calculated using 6-311++G(3df,3pd) basis set. From Table 2.3, it is clear that all the considered functionals overestimate IP and underestimate EA except CAMB3LYP. HSE06 is performing best for IP giving MAE of 0.139 eV and for EA it is CAM-B3LYP with MAE of 0.084 eV. For both IP and EA, LC-TMLYP performs with comparable accuracy with the other range-

Table 2.3: ME and MAE for the following benchmark datasets using the considered range-separated functionals. Best/worst MAE result for each dataset is shown in bold/underline style.

Dataset	Error	LC-TMLYP	CAM-B3LYP	LC-ωPBE	LC-ωPBEh	HSE06
G2/97	ME	-4.494	1.199	1.746	2.276	-4.610
(kcal/mol)	MAE	5.099	**4.329**	5.362	<u>5.735</u>	5.195
IP13	ME	0.083	0.158	0.239	0.147	0.108
(eV)	MAE	0.169	0.196	<u>0.239</u>	0.167	**0.139**
EA13	ME	-0.077	0.022	-0.027	-0.052	-0.068
(eV)	MAE	<u>0.128</u>	**0.084**	0.089	0.105	0.123
PA8	ME	0.012	-0.047	0.086	0.470	0.077
(eV)	MAE	**0.051**	0.084	<u>0.086</u>	0.470	0.077
NCCE31	ME	-0.27	-0.24	-0.70	-0.45	-0.46
(kcal/mol)	MAE	**0.45**	**0.45**	<u>0.78</u>	0.56	0.71
ABDE12	ME	-9.08	-6.63	-5.52	-6.42	-9.38
(kcal/mol)	MAE	9.08	6.63	**5.52**	6.42	<u>9.38</u>
ISOL6	ME	-1.96	-1.80	-1.05	-0.65	-1.12
(kcal/mol)	MAE	1.96	<u>2.03</u>	1.57	1.67	**1.42**
HC7	ME	-5.37	-5.35	16.05	9.22	0.24
(kcal/mol)	MAE	5.37	**5.35**	<u>20.07</u>	13.65	5.92
DC7	ME	-15.69	-4.40	4.43	-1.15	-21.21
(kcal/mol)	MAE	15.69	**9.53**	15.44	17.54	<u>23.07</u>

separated functionals.

Proton affinity (PA) is the amount of released energy when a proton is added to an atom or molecule in its ground state. We compute the PA of the PA8 database with MP2/6-31G(2df,p) level optimized geometry. Except for CAM-B3LYP, all the investigated functionals overestimate PA. LC-TMLYP is the most accurate for PA among the tested functionals.

Binding Energy of Weakly Interacting System:

Weak interactions play a significant role in diverse physical, chemical, and biological phenomena in nature.[99,100,101] It is very important to accurately describe these interactions theoretically for understanding the above technologically influential fields. Inclusion of weak interactions within semilocal DFT is difficult due to their inability to capture the non-local nature of these interactions. However, including kinetic energy density within semilocal DFT considerably reduces the errors of LDA and GGA XC functionals for predicting the binding energy of the weakly interacting systems.[94] We assess our proposed meta-GGA level long-range corrected functional for the NCCE/31 test set with MC-QCISD/3 level optimized geometry.[98] Single point energy is calculated using 6-311++G(3df,3pd) basis set for all the molecules except for the inert gas related molecules where we use aug-cc-pVQZ basis set. All the range-separated functionals perform well for this case as shown in Table 2.3. LC-TMLYP and CAM-B3LYP are the best choices for this database.

Alkyl Bond Dissociation Energies, Isomerization Energies, Hydrocarbon Chemistry and Difficult cases:

Predicting alkyl bond dissociation energy which depends on the size of the alkyl group proved to be challenging for many density functionals.[102] The database ABDE12 for alkyl bond dissociation contains two subsets ABDE4/05 and ABDEL8.[98] ABDE4 subset contains four bond dissociation energies of R-Y type organic molecules, where R = methyl and isopropyl and X = CH_3 and OCH_3 and ABDEL8 includes eight molecules with R = ethyl and tert-butyl and Y = H, CH_3, OCH_3 and OH. For isomerization energy, hydrocarbon chemistry and difficult cases, we use ISOL6,[94] HC7,[94] and DC9[94] test set. For all calculations in this section, 6-311++G(3df,3pd) basis set is used. LC-ωPBE performs the

best for alkyl bond dissociation energy with MAE of 5.52 kcal/mol.

For the isomerization of large molecules, all the investigated functionals underestimate which is evident from Table 2.3. HSE06 gives the best results for ISOL6 and other functionals also give comparable results with that of HSE06.

The hydrocarbon chemistry (HC7) database consists of seven challenging systems containing medium-range correlation energies in hydrocarbons. LC-TMLYP, CAM-B3LYP and HSE06 give comparable results for this test case while LC-ωPBE and LC-ωPBEh are not performing well for this case giving MAE of 20.07 and 13.65 kcal/mol respectively.

The Difficult cases (DC9) includes the reaction energies of nine cases which are found to be challenging for density functional theory.[103,104] The most popular global hybrid density functional, B3LYP, gives an MAE of 20.7 kcal/mol for this case.[105] The general tendency of range-separated functionals is to underestimate the value of reaction energies except for LC-ωPBE. CAM-B3LYP gives the lowest MAE of 9.53 kcal/mol, followed by LC-ωPBE, LC-TMLYP, and LC-ωPBEh functionals.

Thermochemistry of π system:

The database for π system (πTC13)[106,107] consists of three secondary databases - (i) πIE3/06- database of three isomeric energy differences between propyne and allene and higher homologs, (ii) PA-CP5/06- proton affinities of five conjugated polyenes and (iii) PA-SB5/06- proton affinities of five conjugated Schiff bases. Molecules with π bonds are challenging for DFT due to their multiconfigurational state functions which comes from their small HOMO-LUMO gap, where HOMO is the highest occupied molecular orbital and LUMO is the lowest unoccupied molecular orbital. The performance of the range-separated functionals for this database are tested and a summary of results for the full and its secondary databases are shown in Table 2.4. We have taken MP2/6-31+G(d,p) level optimized geometries[98] and 6-311++G(3df,3pd) basis set for all the calculations. All the tested functionals overestimate the result for this case. The CAM-B3LYP provides the best result for this case with an MAE of 3.39 kcal/mol, followed by LC-TMLYP with an MAE of 4.19 kcal/mol.

Barrier Heights of Chemical Reactions:

Table 2.4: Shown are the MAE for πTC13 and its secondary databases for the tested functionals. Best/worst MAE result is shown in bold/underline style. All values are given in kcal/mol.

Functional	πTC13		πIE3/06		PA-CP5/06		PA-SB5/06	
	ME	MAE	ME	MAE	ME	MAE	ME	MAE
LC-TMLYP	4.19	4.19	0.99	0.99	5.19	5.19	5.12	5.12
CAM-B3LYP	3.39	**3.41**	2.37	2.37	3.58	**3.61**	3.82	**3.82**
LC-ωPBE	4.05	4.24	0.17	**0.98**	4.92	4.92	5.51	5.51
LC-ωPBEh	4.79	4.79	2.39	2.39	5.45	5.45	5.58	5.58
HSE06	6.45	<u>6.54</u>	4.54	<u>4.94</u>	6.96	<u>6.96</u>	7.09	<u>7.09</u>

The semilocal density functionals often underestimate the barrier height of chemical reaction. A chemical reaction usually involves the breaking and formation of bonds. In this process, transition state have stretched bonds and hence electron delocalization where the same electron is shared between different molecular fragments. Most of the time semilocal density functionals give lower energy for the transition state with respect to reactants and products, which result in negative barrier height because of the large self-interaction error for these systems.[65] On the other hand, HF theory overestimates the barrier heights. Hence, the error in predicting the transition state energy can be substantially reduced by mixing a portion of HF exchange with the semilocal functionals. However, very often over 50 % of HF exchange is needed to get accurate kinetics, which worsen the results of thermochemistry.[108]

Both forward and reverse reaction barrier heights are computed for nineteen hydrogen and nineteen non-hydrogen transfer reactions from HTBH38 and NHTBH38 dataset[109,110] respectively. Moreover, the set NHTBH38 is partitioned into a set of six heavy-atom transfer reactions, eight nucleophilic substitution reactions, and five unimolecular and association reactions. Single point energy is computed using 6-311++G(3df,3pd) basis set and geometries are taken from Minnesota database.[98] Table 2.5 summarizes the ME and MAE for all the functionals tested. LC-ωPBE and LC-TMLYP give the lowest MAE for hydrogen transfer and non-hydrogen transfer barrier heights respectively. Overall, both LC-ωPBE and LC-TMLYP give comparable results for barrier heights. In this case, the performance of HSE06 is not satisfactory with an MAE of 3.48 kcal/mol for HTBH38

and 5.04 kcal/mol for NHTBH38 respectively.

2.5.3   Dissociation Energy

Here, we describe the dissociation of the H_2^+ and NaCl molecule which are proved to be challenging for density functional approximations. Dissociation energy is defined as the energy required to break all possible chemical bonds in a molecule by isolating all its constituent atomic species. Semilocal density functionals fail to interpret the dissociative nature of symmetric radical cations.[111] This failure of semilocal XC functionals can be attributed to self-interaction error, which comes from the delocalization error[112] associated with these functionals. In the case of H_2^+, semilocal XC functionals predict electron to be equally shared between two infinitely separated hydrogen atoms and for such a fractionally occupied system gives very low energy compared to the hydrogen atom. All the GGA functionals give an error of $50 - 60$ kcal/mol in case of H_2^+ dissociation, which is very large compared to chemical accuracy.[113] The dissociation curve of H_2^+ obtained from the tested range-separated functionals is compared with the HF one. The HF gives the exact result in this case because of its self-interaction free behaviour for one electron system. From Fig. 2.2, it is clear that all the functionals are giving the same equilibrium bond length, but the results start to deviate from the exact one as we go further from equilibrium bond distance. This is due to the enormous self-interaction error at large internuclear distances. LC-TMLYP and LC-ωPBE are giving almost the same dissociation curve while all other functionals deviate too much from the exact result. The HSE06 functional does not perform satisfactorily in this case.

The NaCl molecule is an ionic pair when the interatomic distance 'R' is near about the equilibrium distance. However, at infinite inter-atomic separation, it dissociates into two neutral Na and Cl atoms due to the fact that the $IP_{Na} > EA_{Cl}$. There is a sudden charge transfer ($Na^+ + Cl^- \rightleftharpoons Na + Cl$) that happens at a critical distance R_c,[70] which is given by $R_c = 1/(IP_{Na} - EA_{Cl})$, assuming only the electrostatic interaction between the atoms at R_c. We estimate the value of $R_c \approx 9.4$ Å from the experimental value[114] of IP and EA for Na and Cl respectively. The HF theory overestimates the value of $(IP_{Na} - EA_{Cl})$, and

Table 2.5: Deviations from the reference values of the barrier heights of the chemical reactions are shown for different functionals. Best/worst MAE result is shown in bold/underline style. All values are in Kcal/mol.

Functional	HTBH38 Hydrogen transfer (38)		Non-hydrogen-transfer reactions of the NHTBH38 set							
			Heavy-atom transfer (12)		nucleophilic substitution (16)		Unimolecular and association (10)		Full NHTBH38	
	ME	MAE	ME	MAE	ME	MAE	ME	MAE	ME	MAE
LC-TMLYP	-0.88	2.17	-2.49	2.63	0.05	1.17	0.64	2.04	-0.59	**1.86**
CAM-B3LYP	-3.00	3.29	-5.47	5.47	-0.88	1.19	-0.54	1.76	-2.24	2.69
LC-ωPBE	-0.57	**1.26**	-0.19	2.11	2.95	2.95	1.41	2.34	1.55	2.52
LC-ωPBEh	-3.28	3.31	-4.45	4.45	0.08	0.95	-0.10	2.26	-1.39	2.40
HSE06	-3.45	<u>3.48</u>	2.68	12.37	-1.34	1.53	-0.55	1.83	0.14	<u>5.04</u>

as a result, it underestimates the critical distance by giving $R_c = 5.72$ Å. The dissociation curves of LC-TMLYP and LC-ωPBEh show almost the same behaviour and give $R_c = 8.51$ Å. CAM-B3LYP and LC-ωPBE provide a good description of NaCl dissociation because of their accurate prediction of $(IP_{Na} - EA_{Cl})$ difference and yield $R_c = 8.93$ Å and 9.70 Å respectively. All the range-separated functionals tested here perform reasonably well in the case of NaCl dissociation except for HSE06, which completely fails in this case.
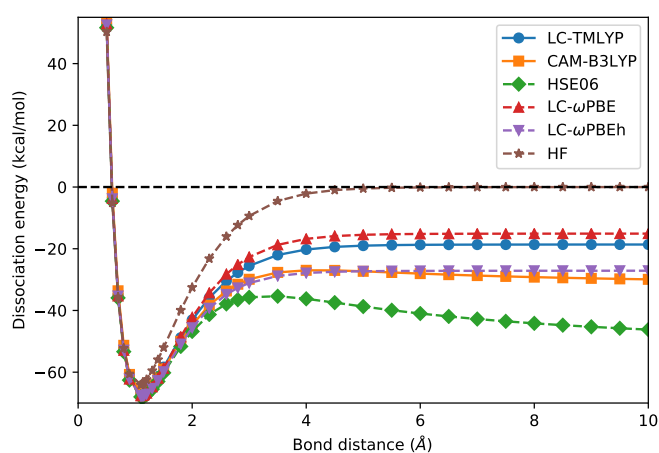
Figure 2.2: Dissociation energy curves of H_2^+ using 6-311++G(3df,3pd) basis set. The zero of the energy level is set to the energy of the hydrogen atom (E(H)).
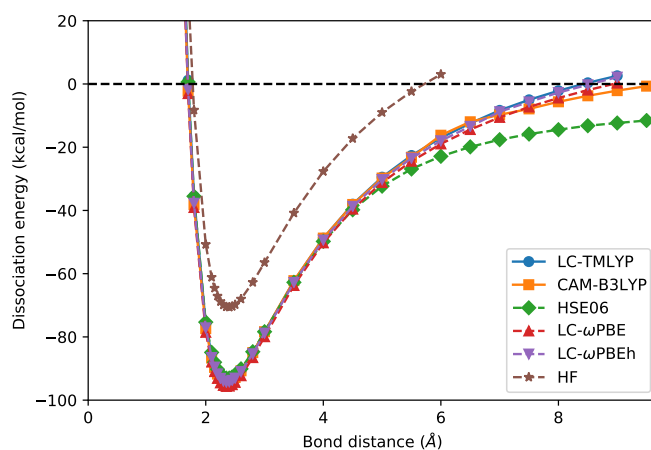
Figure 2.3: Dissociation energy curves of NaCl molecule using 6-311++G(3df,3pd) basis set. The zero of the energy level is set to the energy of E(Na)+E(Cl).

2.5.4   Fractional Particle Number

Here, the performance of the investigated range-separated functionals is explored for the case of fractional electron number perspective. This type of situation arises in the case of ionization potential, electron affinity, and the band gap of the system where the observable properties depend explicitly on the particle number. We take C atom as for illustration and vary the electron number between 5 to 7 in fractional steps using $-1 \leq \varepsilon \leq 0$ and $0 \leq \varepsilon \leq 1$, where ε is defined in Eq. 2.2. The value of ΔE is plotted as a function of particle number for the considered functionals in Fig. 2.4, where ΔE is defined as

$$\Delta E(-1 \leq \varepsilon \leq 0) = E(N_0 + \varepsilon) - [(1 + \varepsilon)E(N_0) - \varepsilon E(N_0 - 1)]$$
$$\Delta E(0 \leq \varepsilon \leq 1) = E(N_0 + \varepsilon) - [(1 - \varepsilon)E(N_0) + \varepsilon E(N_0 + 1)] \qquad (2.18)$$

Due to the inherent delocalization error, the density functionals, predict lower energy for the fractionally occupied state in general and that gives rise to the concave curve shown in Fig. 2.4. For the exact case, ΔE should be zero for the fractionally occupied state which is shown by the black dashed line in Fig. 2.4. The deviation of ΔE from zero is a measure of the delocalization error present in the corresponding XC functional. Mixing HF exchange with semilocal functional reduces the delocalization error. From Fig. 2.4, it is clear that in the range $-1 \leq \varepsilon \leq 0$, LC-$\omega$PBE gives the lowest error in comparison with the exact straight line followed by LC-TMLYP. Other range-separated functionals give substantial deviation in this range. Whereas, for $0 \leq \varepsilon \leq 1$ the LC-ωPBE has the tendency of slight over localization. Also, the LC-TMLYP gives almost the same amount of delocalization as LC-ωPBE localizes the system. This region in important for the stability of C^- anaion. Overall, LC-TMLYP and LC-ωPBE yield result very close to the exact straight line. From Fig. 2.4, it is evident that HF theory overlocalizes the system with fractional electron number which gives rise to the convex curve in the whole region.
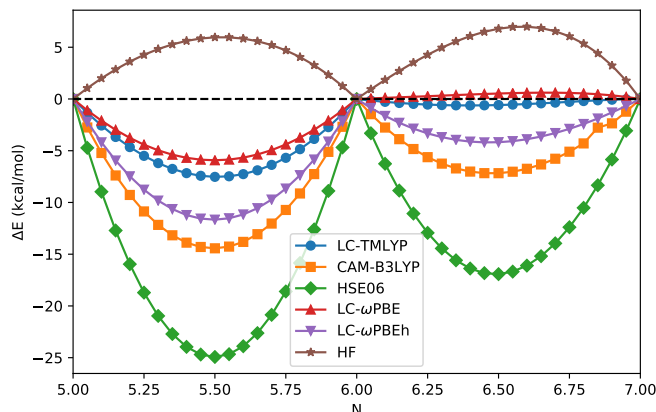
Figure 2.4: Deviation of energy of C atom for fractional occupation for both $-1 \leq \varepsilon \leq 0$ and $0 \leq \varepsilon \leq 1$ using 6-311++G(3df,3pd) basis set.

2.6 Conclusions

The three most important conditions that hinder the accuracy of the density functional approximations are the piecewise linearity of the total energy with fractional particle numbers, one-electron self-interaction free total energy, and asymptotic corrected $(-1/r)$ potential for a finite system. In this chapter, these problems are addressed through developing a new long-range corrected exchange-functional in DFT. The underlying theory is based on the Savin's long-range corrected scheme, where error function is used to split the Coulomb interaction into short-range and long-range parts. The Tao-Mo exchange hole is used in the short-range part and long-range part is described by HF exchange. For benchmarking, the results obtained by using our functional are compared with four popularly known range-separated functionals such as CAM-B3LYP, LC-ωPBE, LC-ωPBEh and HSE06. Out of these functionals, HSE06 mixes HF exchange at the short-range and semilocal exchange hole at the long-range to reduce the computational cost for the extended systems. The CAM-B3LYP and LC-ωPBEh mix HF exchange both at short and long-range and as a consequence of which two extra parameters are needed along with the range-separation parameter μ. The newly developed LC-TMLYP is of LC-ωPBE type, where only one parameter μ is used. The proposed functional gives correct asymptotic exchange potential and at the same time, it retains all the constraints satisfied by

TM exchange hole. The LC-TMLYP functional performs well for the tested molecular databases, also for the fractional particle number cases and dissociation energy because of its less self-interaction error and improved long-range behaviour. This new functional also yields results comparable to the heavily parametrized range-separated functionals like M11[115] and ωB97X.[116] The interesting and promising achievement of this present construction suggests that this functional can be applied for the charge transfer and Rydberg state related problems.

Chapter 3

Semilocal Functional for the Band Gap of Solid-State Systems

3.1 Introduction

Although the semilocal density functionals described in chapter one gives reasonable accuracy to computational ratio but they underestimate the band gap of solid-state systems. Efficient prediction of band gap is very important from the application point of view. Let's try to understand why semilocal functional tend to underestimate the band gap of solids. The fundamental gap of an insulating solid is defined as

$$E_\mathrm{g} = I(N) - A(N), \tag{3.1}$$

where $I(N)$ and $A(N)$ are the ionization energy and electron affinity of the N electron system respectively. In terms of the Kohn-Sham eigen values, the above equation can be expressed as

$$E_\mathrm{g} = \varepsilon_{N+1}(N+1) - \varepsilon_N(N), \tag{3.2}$$

where ε_N and ε_{N+1} are the highest occupied KS energy eigen values of N and $N+1$ electron system respectively.

In the case of a non-interacting KS system, the band gap is defined as

$$E_g^{KS} = \varepsilon_{N+1}(N) - \varepsilon_N(N). \tag{3.3}$$

However, the actual gap of interacting system, E_g and the KS gap E_g^{KS} are related by the following equation

$$E_g = E_g^{KS} + \Delta_{xc}, \tag{3.4}$$

where Δ_{xc} be the many-body correction to the KS gap and is defined by

$$\Delta_{xc} = \varepsilon_{N+1}(N+1) - \varepsilon_{N+1}(N). \tag{3.5}$$

The term Δ_{xc} is related to the derivative discontinuity[70] of the density functionals. The
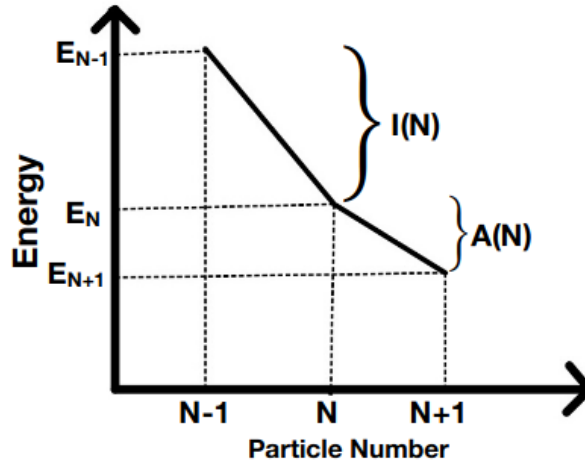
Figure 3.1: The total energy is shown as a function of particle number. There is discontinuity of energy at the integer particle number.

total energy is given by a set of straight lines connecting the energy values at the integer particle numbers as shown in Fig. 3.1 and expressed as

$$E_{N+\varepsilon} = (1-\varepsilon)E_N + \varepsilon E_{N+1}, \quad \text{where} \quad 0 \le \varepsilon \le 1. \tag{3.6}$$

The discontinuity of total energy at the integer particle number leads to the term Δ_{xc} and

it is related to the XC functional in the following way[117]

$$\Delta_{xc} = \frac{\delta E_{xc}[\rho]}{\delta \rho(\mathbf{r})}\bigg|_{N^+} - \frac{\delta E_{xc}[\rho]}{\delta \rho(\mathbf{r})}\bigg|_{N^-}, \tag{3.7}$$

where $N^\pm = \lim_{\varepsilon \to 0} N \pm \varepsilon$. The inclusion of Δ_{xc} improves the calculated band gap value using LDA or GGA functionals.[118,119] Meta-GGA functionals implemented within the generalized KS (gKS) scheme improve the band gap of solids by including some amount of Δ_{xc}.[120,121] The strongly constrained and appropriately normed (SCAN)[34] and meta-GGA made very simple (MVS)[53] functionals have shown promising results for the band gap and in many cases, the accuracy of the MVS functional is comparable to the hybrid functional.[121] Although the hybrid functionals are very accurate in predicting the band gap but they are computationally quite expensive due to the inclusion of the HF exchange term.

In this chapter, we will construct a meta-GGA exchange functional for the band gap of solids using the Becke-Roussel approach.[76] The exchange hole will be modelled using both the hydrogen density and cuspless hydrogen density. The proposed exchange functional in combination with a meta-GGA correlation will be applied to assess the band gap of various solids, from narrow gap semiconductors to wide gap insulators.

3.2   Theoretical Background

3.2.1   Overview of the Becke-Roussel Model

The Becke-Roussel (BR) model for the calculation of the exchange energy of a many-electron system is introduced as it will be used later for functional construction. As described in chapter one, the exchange energy at a point can be regarded as the interaction of the electron density at that point with the exchange hole surrounding that point. Generalizing the Eq. 1.58 for each spin density $\rho_\sigma(\mathbf{r})$, the exchange energy will be expressed as

$$E_x = \frac{1}{2}\sum_\sigma \int \int \frac{\rho_\sigma(\mathbf{r})\langle \rho_{x\sigma}(\mathbf{r}, \mathbf{r}+\mathbf{u})\rangle}{u}\, d\mathbf{r} d\mathbf{u}, \tag{3.8}$$

where $\mathbf{u} = \mathbf{r}' - \mathbf{r}$. The exchange energy is dependent only on the spherical average exchange hole which is defined as

$$\langle \rho_{x\sigma}(\mathbf{r}, \mathbf{r} + \mathbf{u}) \rangle = -\frac{\langle |\rho_{1\sigma}(\mathbf{r}, \mathbf{r} + \mathbf{u})|^2 \rangle}{\rho_\sigma(\mathbf{r})}, \tag{3.9}$$

with

$$\langle |\rho_{1\sigma}(\mathbf{r}, \mathbf{r} + \mathbf{u})|^2 \rangle = \frac{1}{4\pi} \int |\rho_{1\sigma}(\mathbf{r}, \mathbf{r} + \mathbf{u})|^2 \, d\Omega_u. \tag{3.10}$$

where $\rho_{1\sigma}(\mathbf{r}, \mathbf{r} + \mathbf{u}) = \sum_i^{occ} \phi_{i\sigma}^*(\mathbf{r}) \phi_{i\sigma}(\mathbf{r} + \mathbf{u})$ is the first-order reduced density matrix for spin σ and $\phi_{i\sigma}$ be the KS orbital. The exchange hole potential can be defined at reference point $\mathbf{r}$ as the potential generated by the spherical averaged exchange hole and given as

$$U_{x\sigma}(\mathbf{r}) = -\int \frac{\langle \rho_{x\sigma}(\mathbf{r}, \mathbf{r} + \mathbf{u}) \rangle}{u} \, d\mathbf{u}. \tag{3.11}$$

By making use of Eq. 3.11 in Eq. 3.8, the exchange energy can be rewritten as

$$E_x = \frac{1}{2} \sum_\sigma \int \rho_\sigma(\mathbf{r}) U_{x\sigma}(\mathbf{r}) d\mathbf{r} \,. \tag{3.12}$$

The small $\mathbf{u}$ expansion of the exact spherically averaged exchange hole is given as[76]

$$\langle \rho_{x\sigma}(\mathbf{r}, \mathbf{r} + \mathbf{u}) \rangle = \rho_\sigma(\mathbf{r}) + \frac{u^2}{6} \left[\nabla^2 \rho_\sigma(\mathbf{r}) - 4\tau_\sigma + \frac{1}{2} \frac{(\vec{\nabla} \rho_\sigma(\mathbf{r}))^2}{\rho_\sigma(\mathbf{r})} \right] + \cdots, \tag{3.13}$$

where $\tau_\sigma = \frac{1}{2} \sum_i |\nabla \phi_{i\sigma}|^2$. In the BR approach, the above equation is compared with the exchange hole derived using hydrogen density. The inhomogeneity parameter used in this model is defined as

$$Q_\sigma = \frac{1}{6} \left[\nabla^2 \rho_\sigma(\mathbf{r}) - 2\gamma D_\sigma \right], \tag{3.14}$$

where, $D_\sigma = 2\tau_\sigma - \frac{1}{4} \frac{(\vec{\nabla} \rho_\sigma(\mathbf{r}))^2}{\rho_\sigma(\mathbf{r})}$, and γ is an adjustable parameter to recover exact homogeneous potential. After comparing, we can calculate the exchange potential by solving a non-linear equation and subsequently the exchange energy can be calculated using Eq. 3.12.

3.2.2 Laplacian Free BR model

The exchange hole becomes divergent near the nucleus due to the laplacian term present in the Eq. 3.14. We can get rid of this situation by using the second-order gradient expansion (GE2) of the kinetic energy density as,

$$\nabla^2 \rho_\sigma(\mathbf{r}) \approx 3 \left[2\tau_\sigma - \tau_\sigma^{unif} - \frac{1}{36} \frac{(\vec{\nabla}\rho_\sigma(\mathbf{r}))^2}{\rho_\sigma(\mathbf{r})} \right], \tag{3.15}$$

where $\tau_\sigma^{unif} = \frac{3}{5}\left(6\pi^2\right)^{2/3}\rho_\sigma^{5/3}$. There exist several other approximations of $\nabla^2\rho_\sigma(\mathbf{r})$ in terms of τ_σ[122,123,124], but for our present case we only discuss the GE2 expression of Eq. 3.15. After putting the value of $\nabla^2\rho_\sigma(\mathbf{r})$, equation 3.14 reduces to the following form

$$Q_\sigma = (\frac{1}{2} - 2\gamma)\tau_\sigma' - \frac{1}{2}\tau_\sigma^{unif} + (\frac{\gamma}{2} - \frac{1}{12})\frac{|\nabla\rho_\sigma|^2}{\rho_\sigma}, \tag{3.16}$$

where $\tau_\sigma' = 2\tau_\sigma$. Let us generalize the above equation in the following way

$$Q_\sigma = a_1\tau_\sigma' - \frac{1}{2}\tau_\sigma^{unif} + a_2\frac{|\nabla\rho_\sigma|^2}{\rho_\sigma} + a_3\frac{|\nabla\rho_\sigma|^4}{\rho_\sigma^{11/3}}, \tag{3.17}$$

where a fourth-order gradient contribution[125,126] term is added to Q_σ. The above equation will be used further for our functional development and the parameters (a_1, a_2 and a_3) will be determined from several conditions, as discussed in the next section.

3.3 Proposed BR like meta-GGA exchange functionals

Here, laplacian free BR exchange functionals using model hydrogen density and cuspless hydrogen density will be constructed.

3.3.1   Hydrogen Hole Density

Model hydrogen density[127] is given as

$$\rho^H(r) = \frac{\alpha^3}{8\pi} e^{-\alpha r}. \tag{3.18}$$

Spherically averaged hydrogen exchange hole can be calculated as

$$
\begin{aligned}
\rho_x^H(r,u) &= \frac{1}{4\pi} \int \rho^H(\mathbf{r}+\mathbf{u}) d\Omega_u \\
&= \frac{\alpha}{16\pi r u}\left\{ e^{-\alpha|r-u|}(\alpha|r-u|+1) - e^{-\alpha(r+u)}(\alpha(r+u)+1) \right\}
\end{aligned} \tag{3.19}
$$

If we take α and r as parameters a and b and then comparing the Taylor expansion of the Eq. 3.19 with Eq. 3.13, the BR non-linear equation is obtained as,[76]

$$\frac{x \exp(-2x/3)}{x-2} = \frac{2}{3}\pi^{2/3}\frac{\rho_\sigma^{5/3}}{Q_\sigma}, \tag{3.20}$$

where Q_σ is given by Eq. 3.17 and $x = ab$ with b given by the following expression

$$b^3 = \frac{x^3 \exp(-x)}{8\pi\rho_\sigma}. \tag{3.21}$$

The above non-linear equation can be solved using the numerical technique of efficient root finding or by analytic representation,[128] for each value of density, gradient of density, and kinetic energy density. After obtaining the values of x and b, the exchange potential can be calculated using the expression

$$U_{x\sigma}^H(\mathbf{r}) = -(1 - e^{-x} - \frac{1}{2}xe^{-x})/b, \tag{3.22}$$

The meta-GGA exchange functional is calculated by substituting Eq. 3.22 into Eq. 3.12. Since x is a dimensionless ingredient, the exchange energy functional behaves properly under uniform density scaling as described in section 1.7.1. The parameters a_1 and a_2 that are needed to calculate the value of Q_σ, are analytically determined from the following

exact conditions:

1. In case of homogeneous density i.e. $\rho_\sigma(\mathbf{r}) = \rho_{\sigma,0}$, $\nabla\rho_\sigma = 0$, $\tau'_\sigma = \tau^{unif}_\sigma$, the exchange hole potential of Eq. 3.22 should reduce to the LDA value, $U^H_{x\sigma}(\mathbf{r}) = U^{LDA}_{x\sigma}(\mathbf{r}) = -3(\frac{3}{4\pi})^{1/3}\rho^{1/3}_\sigma$.

   For homogeneous electron gas $Q_{\sigma 0} = (a_1 - \frac{1}{2})\tau^{unif}_\sigma$. After putting this value in Eq. 3.20 , we get

$$a_1 - \frac{1}{2} = K_0 \frac{x_0 - 2}{x_0 e^{-2x_0/3}},\tag{3.23}$$

   where $K_0 = 0.156876$. From the condition of above mentioned exchange hole potential we get

$$\frac{e^{x_0/3}}{x_0}(1 - e^{-x_0} - \frac{1}{2}x_0 e^{-x_0}) = K_1,\tag{3.24}$$

   where $K_1 = 0.635348$. The solution of the non-linear equation results x_0 to be 1.104301. Using this value of x_0 in Eq. 3.23, we obtain

$$a_1 = \frac{1}{2} - 0.26568 = 0.23432.\tag{3.25}$$

2. The exchange energy functional should follow the modified second-order gradient expansion (MGE2) for the case of slowly varying density i.e. $\rho_\sigma(\mathbf{r}) = \rho_{\sigma,0} + \delta\rho_\sigma(\mathbf{r})$, with $\delta\rho_\sigma(\mathbf{r}) \ll \rho_\sigma(\mathbf{r})$ and $s_\sigma = |\nabla\rho_\sigma|/[2k_{F\sigma}\rho_\sigma] \leq 1$. The MGE2 provides accurate behaviour for large atoms and for the Thomas-Fermi density scaling.[129,130]

   By considering a small and long wave length perturbation of the homogeneous electron gas, the value of Q_σ and x will be changed slightly from their respective homogeneous value i.e. $Q_\sigma = Q_{\sigma 0} + Q_{\sigma 1}$, and $x = x_0 + x_1$, with $Q_{\sigma 1} \ll Q_{\sigma 0}$, and $x_1 \ll x_0$. After taking the gradient expansion of Eq. 3.17, we find

$$Q_{\sigma 1} = \left(\frac{a_1}{36} + a_2\right)\frac{|\nabla\rho_\sigma|^2}{\rho_\sigma}.\tag{3.26}$$

   Taking the Taylor expansion of Eq. 3.20, and keeping only the linear terms, we

obtain

$$e^{-2x_0/3} \frac{(x_0^2 - 2x_0 + 3)}{(x_0 - 2)^2} x_1 = \pi^{2/3} \frac{\rho_\sigma^{5/3}}{Q_{\sigma 0}^2} Q_{\sigma 1}, \tag{3.27}$$

with $x_1 = 0.305 \left(\frac{a_1}{36} + a_2 \right) \frac{|\nabla \rho_\sigma|^2}{\rho_\sigma^{8/3}}$. Taking the Taylor expansion of Eq. 3.22, the following equation is obtained.

$$
\begin{aligned}
U_{x\sigma}^H &= U_{x\sigma 0}^H + U_{x\sigma 1}^H \\
&= -1.861\rho_\sigma^{1/3} - 0.272\rho_\sigma^{1/3} x_1 \\
&= -1.861\rho_\sigma^{1/3} - 0.0830 \left(\frac{a_1}{36} + a_2 \right) \rho_\sigma^{1/3} \frac{|\nabla \rho_\sigma|^2}{\rho_\sigma^{8/3}}.
\end{aligned} \tag{3.28}
$$

The second-order gradient expansion of the exchange energy density[130] is given as

$$\varepsilon_{x\sigma} = -1.861\rho_\sigma^{1/3} - 0.0306\mu_x\rho_\sigma^{1/3} \frac{|\nabla \rho_\sigma|^2}{\rho_\sigma^{8/3}} \tag{3.29}$$

with μ_x be the second-order coefficient and the value of $\mu_x = 10/81$ for GE2[131] and $\mu_x = 0.26$ for MGE2.[130] Eq. 3.28 follows MGE2 if

$$a_2 = -\frac{a_1}{36} + \frac{0.0306}{0.0830}\mu_x \approx 0.089. \tag{3.30}$$

3. The remaining parameter a_3 is fixed from the band gap values of a small test set of bulk solids, which contains CdTe, CdSe, C, AgBr, and Ne. We choose the value of $a_3 = 0.0053$ to get well balanced band gaps of the narrow (CdTe, CdSe), intermediate (C, AgBr), and wide (Ne) band gap solids.

We call the developed exchange functional as modified Becke-Roussel exchange with hydrogen hole density for the band gap of solids (mBRxH-BG).

3.3.2   Cuspless Hydrogen Hole Density

Model cuspless hydrogen density is given as[127]

$$\rho^C(r) = \frac{\alpha^3}{32\pi} e^{-\alpha r}(1 + \alpha r). \tag{3.31}$$

The exchange hole for this model density is

$$\rho_x^C(r,u) = \frac{\alpha}{64\pi r u}\left\{ e^{-\alpha|r-u|}[\alpha^2(r-u)^2 + 3\alpha|r-u| + 3] \right.$$
$$\left. - e^{-\alpha(r+u)}[\alpha^2(r+u)^2 + 3\alpha(r+u) + 3] \right\}. \tag{3.32}$$

Using the same approach as described in 3.3.1, the non-linear equation is obtained as

$$\frac{(1+x)^{\frac{5}{3}}}{(x-3)} e^{-2x/3} = (32\pi)^{2/3}\frac{1}{6}\frac{\rho_\sigma^{5/3}}{Q_\sigma}, \tag{3.33}$$

and the corresponding exchange hole potential is given by

$$U_{x\sigma}^C = -\frac{1}{8b} e^{-x}(-x^2 - 5x + 8e^x - 8), \tag{3.34}$$

where

$$b^3 = \frac{x^3(1+x)e^{-x}}{32\pi\rho_\sigma}. \tag{3.35}$$

The parameter a_1, a_2 and a_3 are determined using conditions same as described in 3.3.1.

1. For homogeneous density, replacing the value of Q_σ by $Q_{\sigma 0}$ in Eq. 3.33, we obtain

$$a_1 - \frac{1}{2} = K_0 \frac{x_0 - 3}{(1 + x_0)^{5/3} e^{(-2x_0/3)}}, \tag{3.36}$$

where $K_0 = 0.39530296$. From the condition of exchange hole potential $U_{x\sigma}^C(\mathbf{r}) = U_{x\sigma}^{LDA}(\mathbf{r}) = -3(\frac{3}{4\pi})^{1/3}\rho_\sigma^{1/3}$, we get

$$\frac{e^{-2x_0/3}}{x_0(1+x_0)^{1/3}}(-x_0^2 - 5x_0 + 8e^{x_0} - 8) = K_1, \tag{3.37}$$

where $K_1 = 3.2019539$. After solving numerically, we get the value $x_0 = 1.201014$ and putting this value in Eq. 3.36 we obtain

$$a_1 = \frac{1}{2} - 0.425254 = 0.074746. \tag{3.38}$$

2. If we perform the same perturbative analysis as done for the hydrogen density case, we get

$$4e^{-2x_0/3}\frac{(x_0^2 - 3x_0 + 6)(1 + x_0)^{2/3}}{(x_0 - 3)^2}x_1 = (32\pi)^{2/3}\frac{\rho_\sigma^{5/3}}{Q_{\sigma 0}^2}Q_{\sigma 1}, \tag{3.39}$$

where $x_1 = 0.4\left(\frac{a_1}{36} + a_2\right)\frac{|\nabla\rho_\sigma|^2}{\rho_\sigma^{8/3}}$, and

$$U_{x\sigma}^C = -1.861\rho_\sigma^{1/3} - 0.0532\left(\frac{a_1}{36} + a_2\right)\rho_\sigma^{1/3}\frac{|\nabla\rho_\sigma|^2}{\rho_\sigma^{8/3}}. \tag{3.40}$$

Comparing the above equation with Eq. 3.29, we get

$$a_2 = -\frac{a_1}{36} + \frac{0.0306}{0.0532}\mu_x \approx 0.147. \tag{3.41}$$

3. The remaining parameter a_3 is fitted in the same way as done in the hydrogen density case.

Table 3.1: Shown are the parameter values for the mBRxH-BG and mBRxC-BG exchange energy functionals.

	a_1	a_2	a_3
mBRxH-BG	0.23432	0.089	0.0053
mBRxC-BG	0.074746	0.147	0.0032

We call this exchange functional as modified Becke-Roussel exchange with cuspless hydrogen hole density for the band gap of solids (mBRxC-BG). The parameters for both the proposed functionals are shown in Table 3.1.

3.3.3   Comparison between the mBRxH-BG and mBRxC-BG meta-GGA Exchange Functionals

In the left panel of Fig. 3.2, we have shown the electron densities for both the hydrogen and the cuspless hydrogen densities and their reduced density gradients ($s_\sigma = |\nabla \rho_\sigma|/[2k_{F\sigma}\rho_\sigma]$). The hydrogen density is more localized due to its nuclear cusp and the density gradient for this case increases monotonically from its minimum value at $r = 0$ ($s^H \geq s^H_{\min} \approx 0.376$). Hence the value of s in the region $0 \leq s < 0.376$ is not well represented by the hydrogen density and for bulk solids, s can be smaller than $s^H_{\min}$. This limitation is resolved by the more delocalized cuspless hydrogen density and its reduced density gradient covers all possible values of s ($s^C \geq 0$).
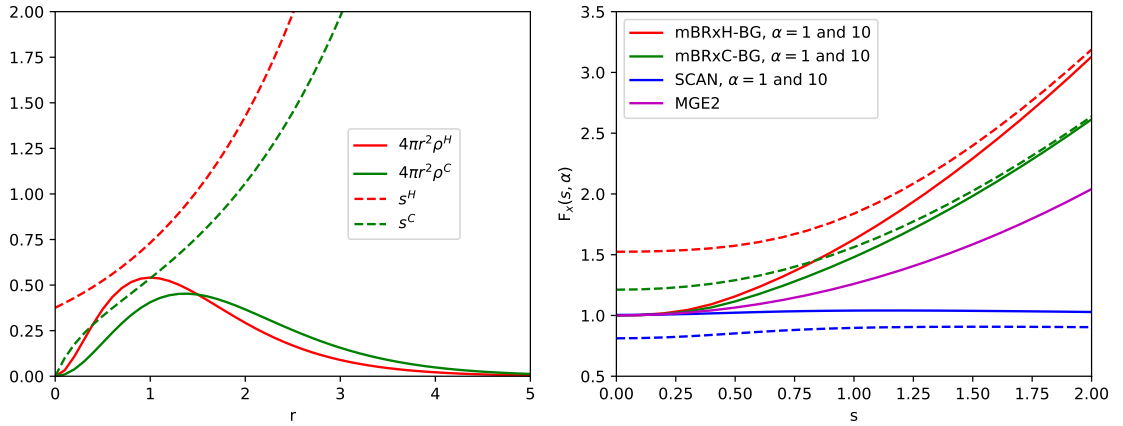
Figure 3.2: Left panel: The probability distribution and reduced density gradient are shown for both the hydrogen and cuspless hydrogen density case with $\alpha = 2$. Right panel: Comparison of the mBRxH-BG and mBRxC-BG exchange functionals with MGE2 ($F_x^{\mathrm{MGE2}} = 1 + 0.26s^2$) and SCAN meta-GGA functionals. Solid and dashed lines represent $\alpha = 1$ and $\alpha = 10$ cases respectively.

In the right panel of Fig. 3.2, the exchange enhancement factor of mBRxH-BG and mBRxC-BG functionals are compared with the MGE2 and SCAN meta-GGA functionals for $\alpha = 1$ and $\alpha = 10$. Here, $\alpha = (\tau - \tau^W)/\tau^{unif}$ is a well-known meta-GGA ingredient with $\tau^W = |\nabla \rho|^2/(8\rho)$. The mBRxH-BG and mBRxC-BG functionals recover MGE2 by construction when $\alpha \approx 1$ and $s \leq 0.5$ and for other values of s, they are larger than MGE2 due to the fourth-order gradient term in the expression of Q_σ. This large enhancement of

the exchange w.r.t. LDA is coming from the a_3 term which is fitted to the band gap energies of few solids. For this reason, these functionals are not suitable for the ground-state properties. It is important to note that even MGE2 is not accurate for solid-state calculations and we need a negative fourth-order gradient term which is present in the SG4 GGA functional.[130] In the present case, a more sophisticated form of Q_σ and incorporation of more exact constraints can give good results for ground-state properties which will be discussed in the chapter four but in this chapter, we solely focus on the band gap. Finally, we conclude that mBRxC-BG enhancement factor performs better than mBRxH-BG one and this shows that the cuspless density is more relevant for the BR method applied to solid-state calculations.

3.4   Computational Details

We use one-electron self-interaction free Tao-Perdew-Staroverov-Scuseria[32] (TPSSc) correlation functional in combination with our proposed exchange functionals. Although the choice of other correlation functionals is possible. But, we found that the TPSS correlation functional is properly fitted with our mBRxBG functionals for the narrow and intermediate band gap solids. We implement the mBRxBG functionals in the Vienna *ab initio* simulation package (VASP)[132,133] which is a plane wave pseudopotential based code. To implement the functionals, we follow the gKS framework which is described in Appendix B. A $15 \times 15 \times 15$ Monkhorst-Pack k-mesh and 700 eV kinetic energy cut-off for plane waves is used for all the calculations.

We perform a convergence checking of the proposed functionals by calculating the band gap of diamond w.r.t. the energy cut-off and k-mesh which is shown in Fig. 3.3. For comparison, we have also included the result of mBJLDA[134] calculated with VASP. From Fig. 3.3, it is obvious that all methods show smooth convergence starting from 400 eV energy cut-off and $15 \times 15 \times 15$ k-mesh.
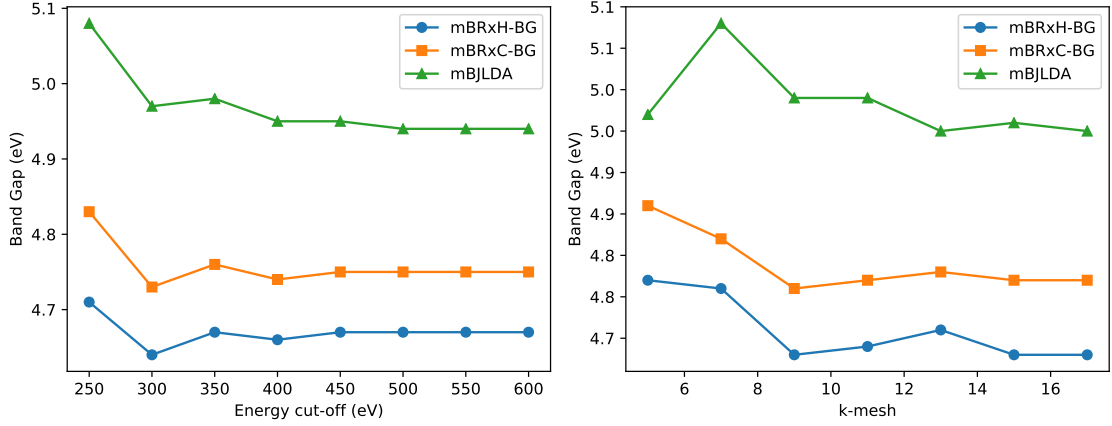
Figure 3.3: Left panel: Convergence of plane wave cut-off with band gap. We used $15 \times 15 \times 15$ Monkhorst-Pack k-mesh for this test. Right panel: Convergence of k-mesh with band gap. We used 700 eV energy cut-off for this test.

3.5 Results

To benchmark our functionals, we examine fifteen narrow band gap semiconductors with $0 \leq E_g \leq 2$ eV, thirty intermediate band gap semiconductors with $2 \leq E_g \leq 6.5$ eV, nine wide band gap ionic solids with $7 \leq E_g \leq 14.2$ eV, four rare gas solids with $9.2 \leq E_g \leq 21.5$ eV and nine layered materials with $1 \leq E_g \leq 3$ eV. The spin-orbit coupling (SOC) effect is taken into account for the calculation of band gaps. The SOC plays an important role in the case of narrow band gap semiconductors and its influence tends to lower the calculated band gap.[135,136] The SOC correction to the band gap have been calculated using PBE functional and for other functionals we subtract the SOC corrected PBE values which are shown to be a reasonable approximation.[135]

3.5.1 Narrow Band Gap Semiconductors

Narrow band gap materials are very important from technological viewpoint. From Table 3.2 and Fig. 3.4, it is clear that mBRxC-BG performs better than MVS, SCAN and mBRxH-BG, but worse than mBJLDA and HSE06. Note that the mBJLDA[134] is a potential only functional designed for band gap of solids and for calculation purpose used

with LDA XC energy. On the other hand, HSE06 is a hybrid functional for which the computational cost is high. In general, the mBRxC-BG slightly overestimates the band gap of these semiconductors with the exceptions of InN, Ge, GaSb, ScN, and GaAs where
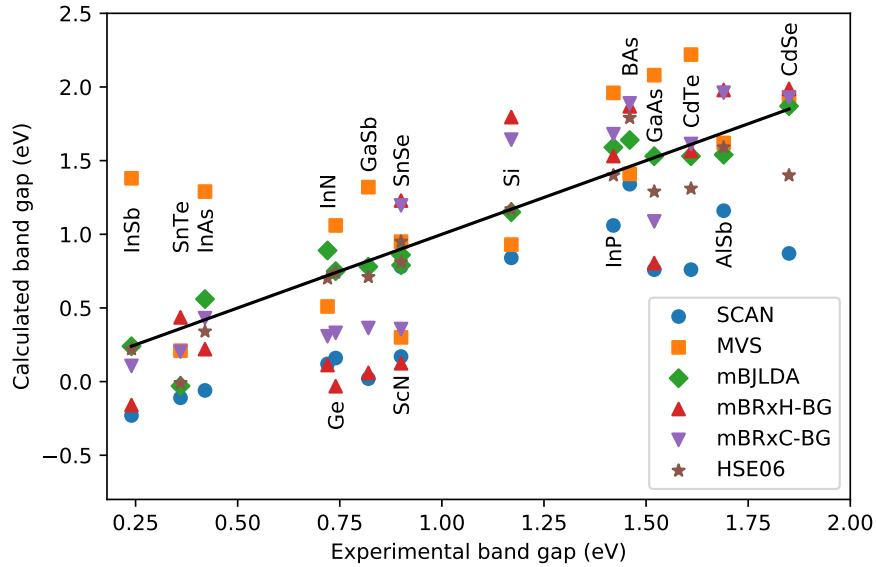
Figure 3.4: Calculated band gaps vs experimental band gaps for the narrow gap semiconductors.

it predicts smaller band gap values. We observe that the MVS functional largely overestimates the band gaps of some solids (InSb, InAs, GaSb, InP, GaSb, GaAs and CdTe). In summary, we can conclude that the mBRxC-BG functional provides good band gap values within the meta-GGA XC functionals, except for a few cases (for example Si).

3.5.2 Intermediate Band Gap Semiconductors

The mBRxH-BG and mBRxC-BG functionals provide balanced band gap values over the different band-gap range of materials in this category and improve over SCAN and MVS functionals. SCAN has the natural tendency to underestimate the band gap. On the other hand, although MVS gives larger gap than SCAN but in most cases still underestimate the gap. The mBRx based functionals give band gap values closer to the mBJLDA and HSE06 results. The SOC effect is important for some materials (e.g, ZnTe, BaTe, MgTe

and AgI) but the correction due to it is well below 10% of the experimental band gap values. An overview of the functionals performance is shown in Fig. 3.5.
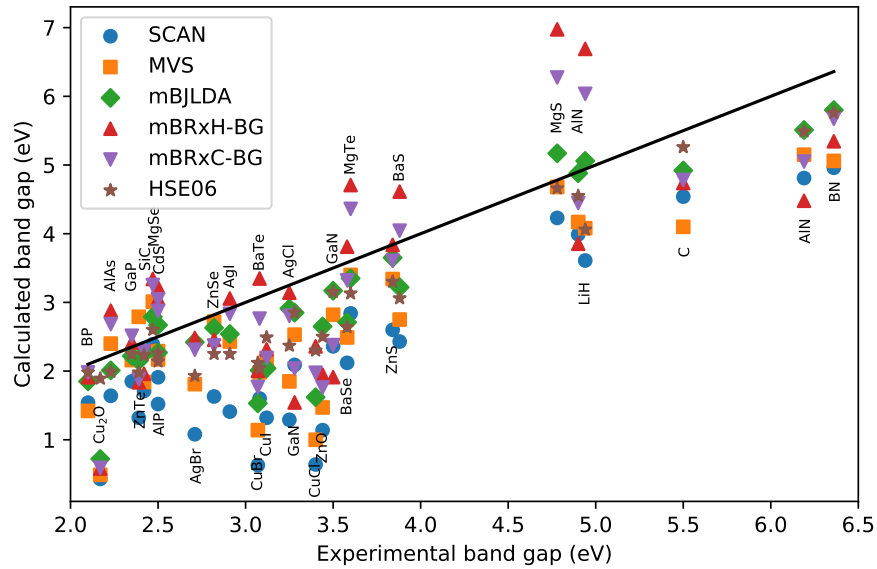
Figure 3.5: Calculated band gaps vs experimental band gaps for the intermediate gap semiconductors.
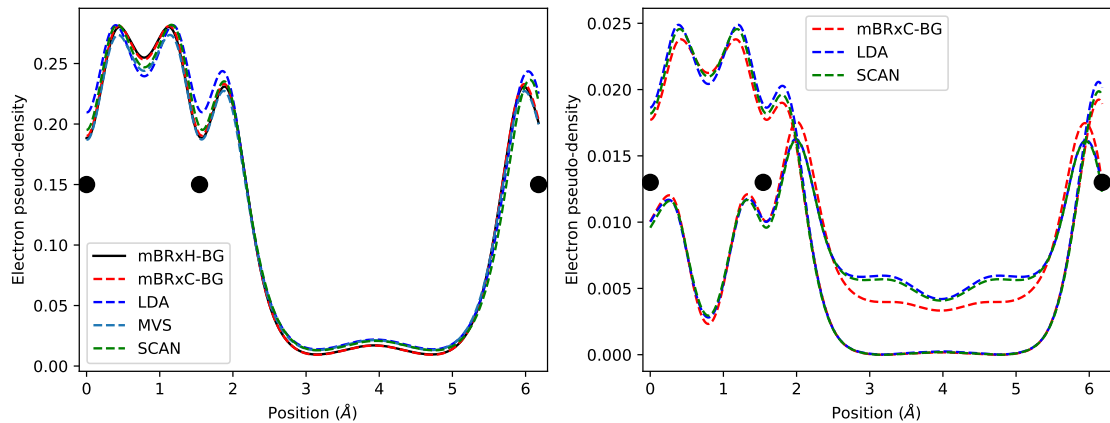
Figure 3.6: Left panel: The electron pseudodensities of the valence band along [111] direction of diamond bulk using different functionals. Right panel: The electron pseudo-densities of the CBM and VBM along the same direction as in the left panel.

In Fig. 3.6, we have plotted the pseudodensity of the valence band and also that of the conduction band minima (CBM) and valence band maxima (VBM) along the [111]

direction of carbon diamond to understand the physical behaviour of the meta-GGA functionals. The mBRxH-BG and mBRxC-BG valence band pseudodensities are slightly lowered w.r.t. other curves in the bonding region, in the range 3 to 5 Å(see the left pannel of Fig. 3.6). This is due to the strong exchange enhancement of these functionals. However, all curves agree well with each other in other regions. From the right panel of Fig. 3.6, it is clear that the CBM pseudodensity of mBRxC-BG differs significantly from LDA and SCAN values in the same bonding region.

Table 3.2: The band gap of considered solids using different level of XC functional approximations. The SOC effect is taken into account by subtracting the SOC correction calculated by PBE functional given in parentheses. The SOC uncorrected HSE06 and mBJLDA values are taken from Ref..[137] All calculations are performed at the experimental lattice constant, given in Ref..[137] The experimental band gap values are taken from Ref..[137] Mean absolute error (MAE) and mean absolute relative error (MARE is percent) are reported for each group of solids.

solids	PBE (SOC)	SCAN	MVS	mBJLDA	mBRxH-BG	mBRxC-BG	HSE06	Exp.
			Narrow band gaps (0 − 2 eV)					
InSb	-0.23 (0.23)	-0.23	1.38	0.24	-0.16	0.11	0.22	0.24
SnTe	-0.11 (0.18)	-0.11	0.21	-0.03	0.43	0.20	-0.01	0.36
InAs	-0.11 (0.11)	-0.06	1.29	0.56	0.22	0.43	0.34	0.42
InN	0.03 (0.00)	0.12	0.51	0.89	0.11	0.31	0.70	0.72
Ge	0.00 (0.08)	0.16	1.06	0.75	-0.03	0.33	0.74	0.74
GaSb	0.00 (0.17)	0.02	1.32	0.78	0.06	0.36	0.71	0.82
SnSe	0.55 (0.03)	0.78	0.95	0.86	1.23	1.19	0.95	0.90
ScN	-0.09 (0.09)	0.17	0.3	0.79	0.12	0.36	0.81	0.90
Si	0.59 (0.00)	0.84	0.93	1.15	1.79	1.64	1.17	1.17
InP	0.71 (0.03)	1.06	1.96	1.59	1.53	1.68	1.40	1.42
BAs	1.10 (0.07)	1.34	1.41	1.64	1.87	1.89	1.79	1.46
GaAs	0.49 (0.11)	0.76	2.08	1.53	0.80	1.09	1.29	1.52
CdTe	0.50 (0.26)	0.76	2.22	1.53	1.56	1.61	1.31	1.61
AlSb	0.99 (0.21)	1.16	1.62	1.54	1.98	1.96	1.59	1.69
CdSe	0.51 (0.12)	0.87	1.93	1.87	1.99	1.93	1.40	1.85
MAE	0.73	0.54	0.40	0.10	0.42	0.29	0.14	
MARE	84.80	69.55	71.64	15.32	53.51	33.34	16.66	
			Intermediate band gaps (> 2 − 6.5 eV)					
BP	1.24 (0.00)	1.54	1.42	1.85	1.91	1.98	1.98	2.10
Cu2O	0.41 (0.09)	0.43	0.49	0.72	0.58	0.59	1.89	2.17
AlAs	1.34 (0.12)	1.64	2.4	2.01	2.88	2.68	1.99	2.23
GaP	1.60 (0.03)	1.85	2.16	2.22	2.41	2.51	2.25	2.35
ZnTe	1.00 (0.27)	1.32	2.79	2.15	1.84	1.88	1.98	2.39
SiC	1.35 (0.00)	1.71	1.84	2.25	1.96	2.29	2.23	2.42
MgSe	1.76 (0.14)	2.39	3.01	2.79	3.34	3.25	2.6	2.47

Table 3.2 (continued.)

solids	PBE (SOC)	SCAN	MVS	mBJLDA	mBRxH-BG	mBRxC-BG	HSE06	Exp.
CdS	1.16 (0.00)	1.52	2.29	2.67	3.06	2.87	2.14	2.50
AlP	1.56 (0.04)	1.91	2.17	2.27	3.22	3.04	2.26	2.50
AgCl	0.86 (0.04)	1.29	1.85	2.91	3.14	2.80	2.37	3.25
AgBr	0.60 (0.08)	1.08	1.81	2.42	2.48	2.31	1.93	2.71
ZnSe	1.16 (0.12)	1.63	2.72	2.63	2.45	2.37	2.25	2.82
AgI	1.10 (0.23)	1.41	2.43	2.54	3.06	2.83	2.25	2.91
CuBr	0.33 (0.03)	0.63	1.14	1.53	2.00	1.77	2.12	3.07
BaTe	1.26 (0.27)	1.6	1.98	2.01	3.35	2.76	2.04	3.08
CuI	0.98 (0.16)	1.32	2.18	2.04	2.32	2.19	2.49	3.12
GaN	1.72 (0.00)	2.09	2.53	2.85	1.54	2.04	2.85	3.28
CuCl	0.38 (0.07)	0.64	1.00	1.62	2.36	1.97	2.3	3.40
ZnO (Wurzite)	0.77 (0.00)	1.14	1.47	2.65	1.95	1.76	2.50	3.44
GaN (Wurzite)	1.99 (0.00)	2.36	2.82	3.17	1.91	2.38	3.15	3.5
MgTe	2.23 (0.26)	2.84	3.40	3.35	4.71	4.36	3.13	3.60
BaSe	1.75 (0.15)	2.12	2.49	2.71	3.81	3.32	2.64	3.58
ZnS	2.09 (0.00)	2.6	3.34	3.65	3.84	3.61	3.3	3.84
BaS	2.07 (0.05)	2.43	2.75	3.22	4.61	4.04	3.06	3.88
MgS	3.56 (0.00)	4.23	4.68	5.17	6.97	6.27	4.66	4.78
AlN	3.38 (0.00)	3.99	4.17	4.88	3.85	4.45	4.55	4.90
LiH	2.98 (0.00)	3.61	4.08	5.06	6.69	6.04	4.06	4.94
C	4.13 (0.00)	4.54	4.10	4.92	4.74	4.78	5.26	5.50
AlN (Wurzite)	4.15 (0.00)	4.81	5.15	5.51	4.48	5.05	5.49	6.19
BN	4.47 (0.00)	4.96	5.06	5.80	5.34	5.67	5.76	6.36
MAE	1.66	1.25	0.86	0.52	0.83	0.70	0.53	
MARE	50.93	38.71	26.00	16.42	24.33	21.14	16.05	
			Ionic wide-band gap solids					
CaO	3.65 (0.00)	4.22	4.59	5.35	4.55	4.70	5.26	7.00
MgO	4.76 (0.00)	5.6	6.01	7.13	6.00	6.25	6.47	7.83
KCl	5.15 (0.04)	5.74	6.70	8.44	10.74	10.09	6.49	8.50
NaCl	5.13 (0.04)	5.89	6.79	8.41	11.14	9.53	6.57	8.50
LiCl	6.37 (0.03)	7.26	7.97	8.61	10.73	9.77	7.78	9.40
BeO	7.51 (0.00)	8.36	8.59	9.66	8.48	8.93	9.48	10.60
KF	6.10 (0.09)	6.68	7.48	10.31	11.56	11.11	8.09	10.90
NaF	6.35 (0.04)	7.09	7.91	11.42	11.72	10.36	8.53	11.50
LiF	9.20 (0.03)	10.09	10.69	12.86	12.98	12.18	11.43	14.20
MAE	3.80	3.05	2.41	0.69	1.63	1.32	2.04	
MARE	39.06	31.25	24.49	7.45	18.50	14.41	20.83	
			Rare gas solids					
Xe	5.80 (0.44)	6.47	7.75	8.04	11.83	10.87	7.00	9.29
Kr	7.02 (0.23)	7.77	9.12	10.57	14.90	13.69	8.48	11.59
Ar	8.62 (0.06)	9.46	10.86	13.78	18.06	16.46	10.31	14.15
Ne	11.50 (0.12)	12.77	14.47	22.21	28.57	22.33	14.15	21.48
MAE	5.89	5.01	3.58	0.84	4.21	1.71	4.14	
MARE	40.63	34.25	23.44	7.07	29.12	13.87	28.19	

3.5.3   Ionic Wide Band Gap Solids and Rare Gas Insulators

The results of this section are reported in the lower panel of the Table 3.2 and shown in Fig. 3.7. The mBRxC-BG produces very promising results in this case within semilocal functionals and outperforms the SCAN, MVS, and HSE06 screened hybrid functional. The performance of mBRxC-BG is remarkably accurate for these class of solids and very close to the mBJLDA values.
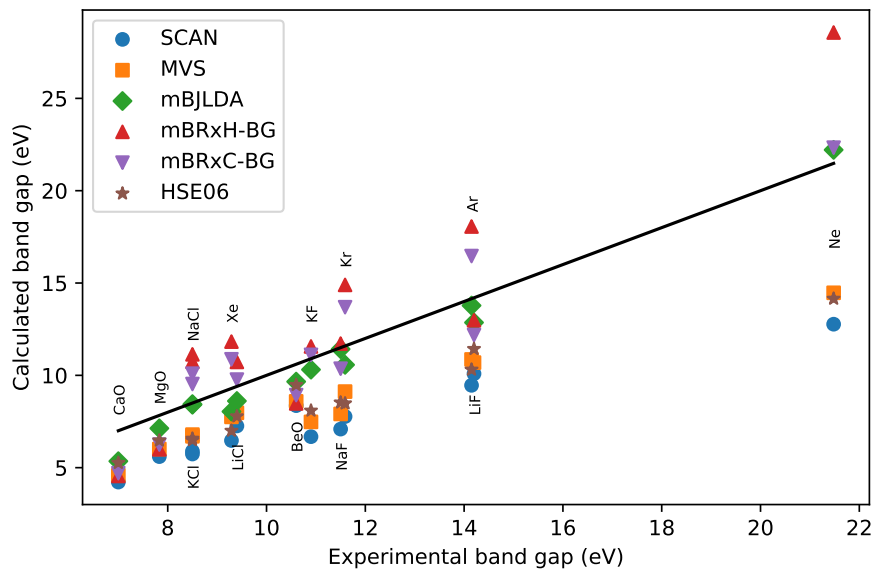
Figure 3.7: Calculated band gaps vs experimental band gaps for the ionic and rare gas solids.

In Fig. 3.8, we compare the band structure of Ar solid calculated using the SCAN and mBRxC-BG functionals. The mBRxC-BG predicts accurate band gap of Ar crystal and at the same time shows a smooth and physical band structure. This improvement of the band gap of the insulators is mainly due to the fourth-order gradient terms in the Q_σ of Eq. 3.17, which plays a significant role when $s \geq 0.5$ (see the right panel of Fig. 3.2).

3.5.4   Layered Solids

Layered materials are promising candidates for application in various electronic and optoelectronic devices. Recently, more than 5000 layered materials have been determined
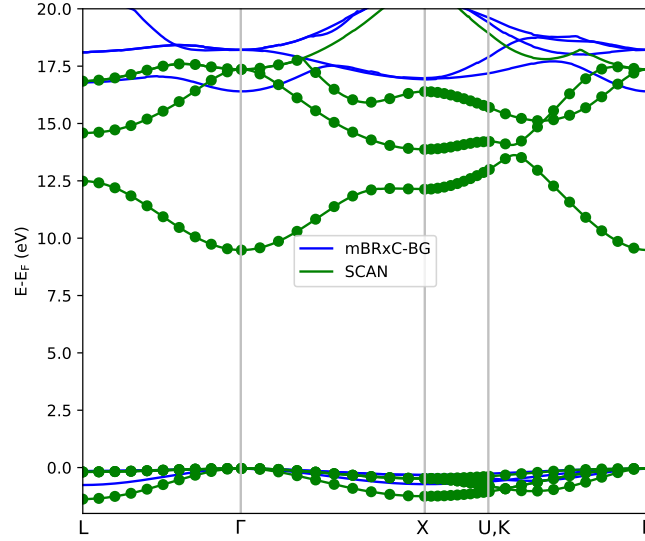
Figure 3.8: Band structure of Ar solid is shown using the mBRxC-BG and SCAN functionals.

from high-throughput DFT calculations[138] and accurate prediction of their band gaps is very important for further application. The results of the band gaps of the considered layered solids are shown in Table 3.3. The best performing functional is the mBRxC-BG with MAE = 0.18 eV, followed by HSE with MAE = 0.19 eV, MVS and mBJLDA with MAE = 0.28 eV and SCAN with MAE = 0.40 eV. Although the performance of mBJLDA is the best for other solids, but in this case, it shows a systematic underestimation of the band gaps. This underestimation of mBJLDA is an inherent problem that is related to the unit cell average of a quantity involving density and gradient of density, used in the construction of the mBJLDA potential. Recently, a reparametrized form of the mBJLDA is proposed for layered materials.[139] However, other functionals such SCAN, MVS, mBRxC-BG, and hybrid functionals are free from such an anomaly.

3.5.5 Overall Statistics

Overall error statistics for the band gaps computed using different functionals are shown in Table 3.4. Different errors have been reported as the mean (relative) error (M(R)E), mean absolute (relative) error (MA(R)E), and the standard deviation (relative) error (STD(R)E).

Table 3.3: The band gaps of the considered layered materials in their bulk form as calculated using different XC functionals. Experimental band gaps are taken from the references.[140,141,142,143] The mBJLDA calculations are performed in the WIEN2k code.[144] The HSE06 calculations are performed in the VASP[132,133] code. The SOC effect is taken into account in the same way as described in the Table 3.2. The last line reports MAE and MARE (%) in eV.

Solids	PBE (SOC)	SCAN	MVS	mBJLDA	mBRxH-BG	mBRxC-BG	HSE06	Expt.
HfS_2	0.94 (0.00)	1.29	1.52	1.64	1.56	1.71	1.70	1.96
$HfSe_2$	0.32 (0.16)	0.68	0.94	0.90	0.81	0.98	0.98	1.13
MoS_2	0.91 (0.00)	1.01	1.05	1.12	1.13	1.18	1.46	1.29
$MoSe_2$	0.85 (0.00)	0.96	1.01	1.02	1.14	1.21	1.33	1.10
WS_2	0.99 (0.05)	1.18	1.13	1.18	1.32	1.38	1.51	1.35
WSe_2	0.91 (0.08)	1.11	1.05	1.07	1.28	1.32	1.36	1.20
ZrS_2	0.81 (0.00)	1.12	1.32	1.26	1.44	1.50	1.59	1.68
$ZrSe_2$	0.20 (0.13)	0.51	0.74	0.57	0.72	0.78	0.87	1.20
$ZrSeS$	0.52 (0.06)	0.83	1.05	1.02	1.10	1.16	1.24	1.40
MAE	0.65	0.40	0.28	0.28	0.23	0.18	0.19	
MARE	47.19	28.90	19.96	20.58	16.56	13.28	15.45	

Table 3.4: Summary of different error calculations of 67 test solids using various XC functionals.

	SCAN	MVS	mBJLDA	mBRxH-BG	mBRxC-BG	HSE06
ME (eV)	-1.45	-0.88	-0.36	0.01	-0.15	-0.78
MAE (eV)	1.45	1.05	0.44	0.97	0.68	0.82
STDE (eV)	1.42	1.29	0.50	1.48	0.90	1.19
MRE (%)	-43.03	-6.54	-11.44	-10.00	-8.56	-14.57
MARE (%)	43.03	35.05	14.97	29.32	21.48	17.34
STDRE (%)	31.22	69.80	20.11	39.13	25.80	16.63

The SCAN meta-GGA functional gives the worst result with MAE = 1.45 eV and MARE = 43.03 eV and followed by the MVS functional with MAE = 1.05 eV and MARE = 35.05 eV. On the other hand, the performance of mBRxC-BG is comparable to the HSE06 functional and slightly worse than the mBJLDA potential only functional. It has been observed that the mBRxC-BG provides systematic improvement over mBRxH-BG.

3.6 Conclusions

Two meta-GGA exchange functionals (mBRxH-BG and mBRxC-BG) are proposed using the model hydrogen and cuspless hydrogen density respectively. The functionals are designed using BR model by modifying and generalizing the second-order gradient expansion Q_σ in such a way that it becomes laplacian free and satisfies several exact constraints (see Eq. 3.17). In combination with TPSS correlation, the mBRxH-BG and mBRxC-BG functionals are used to calculate the band gaps of a large palette of bulk solids including narrow to wide gap solids and covalently bonded solids to noncovalently bonded layered materials. The performance of mBRxC-BG is better than mBRxH-BG, MVS, and SCAN functionals and close to the mBJLDA and HSE06 results. The mBRxC-BG could be a potential replacement for computationally demanding hybrid functional for calculating the band gaps of semiconductors. This method of constructing exchange functionals can be further investigated by considering the more sophisticated expression of Q_σ to recover other exact constraints of XC functional.

Chapter 4

Importance of the Pauli Kinetic Energy Density for Semilocal Functionals

4.1 Introduction

In the previous chapter, we have discussed how meta-GGA functionals are constructed by using modified Becke-Roussel approach for the band gap of solids. Meta-GGA exchange energy density $[\varepsilon_{\text{xc}}^{\text{MGGA}}(\rho(\mathbf{r}), \nabla\rho(\mathbf{r}), \nabla^2\rho(\mathbf{r}), \tau(\mathbf{r}))]$ is in general depends upon the electron density, density gradient, Laplacian of density, and positive definite KS kinetic energy density $\tau(\mathbf{r}) = \sum_i^{occ} \frac{|\nabla\phi_i(\mathbf{r})|^2}{2}$, where ϕ_i is the ith occupied KS orbital. However, $\nabla^2\rho(\mathbf{r})$ is not favoured in constructing meta-GGA functionals due to its unphysical oscillation in the functional derivative and on the other hand, almost entire information of $\nabla^2\rho(\mathbf{r})$ is contained in $\tau(\mathbf{r})$. One of the advantages of the meta-GGA functionals is that they can be reliably used for both in the quantum chemistry and solid-state physics. The use of $\tau(\mathbf{r})$ in the meta-GGA functional gives us the freedom to recover the important exact conditions of the XC functional.[32,53] Most of the calculations involving meta-GGA functional are performed in the generalized Kohn-Sham (gKS) scheme.

Regarding the recent developments in the meta-GGA functional, Pauli kinetic enhancement factor $\alpha = (\tau - \tau^{\text{W}})/\tau^{\text{unif}}$ has been shown to be an important ingredient and used together with $s = |\nabla\rho|/[2(3\pi^2)^{1/3}\rho^{4/3}]$ in the construction of meta-GGA function-

als.[32,33,34] Note that, α can be rewritten as

$$\alpha = F_s^{\mathrm{KS}} - \frac{5}{3}s^2, \qquad (4.1)$$

where $F_s^{\mathrm{KS}} = \tau/\tau^{\mathrm{unif}}$ is the exact KS kinetic energy enhancement factor. It is important to note that α contains all the many-body fermionic effect of the kinetic energy and is directly related to the electron localization function.[145] Alpha (α) can distinguish different bonding environments inside a many-electron system in the following way

1. $\alpha = 0$ recognizes one- and two-electron densities characterizing single bonds.

2. $\alpha \approx 1$ is the slowly varying density density limit which characterizes metallic bonds.

3. $\alpha \gg 1$ corresponds to the region of density overlap between closed shells and it is the characteristic of weak noncovalent bonds.

The recently developed MVS,[53] SCAN,[34] and TM[33] functionals use both α and s as their ingredients.

Getting motivated by these recent developments, in this chapter, we will develop a technique for meta-GGA exchange functional construction depending only on the Pauli kinetic energy density. Our procedure will be based on a generalization of the BR model using the cuspless hydrogen density as a model. In the previous chapter, we investigated almost similar idea in a different way and proposed mBRxC-BG meta-GGA functional, efficient for the band gap energy of bulk solids.[146] However, here our aim is to build a meta-GGA functional which will be accurate for the quantum chemistry as well as solid-state physics. This will be validated by applying our functional for several molecular and solid-state test cases.

4.2 Proposed Functional Based on Pauli Kinetic Energy Density

Let's start with the exchange functional construction following the BR[76] approach using the model cuspless hydrogen density $\rho^C(r) = \frac{a^3}{32\pi}e^{-ar}(1+ar)]$ with $a \geq 0$. However, unlike previous functional construction where we have considered both the hydrogen and cuspless hydrogen density for functional development, here the cuspless hydrogen density only will be taken into consideration. This is due to the known limitation of the hydrogen density for which the density gradient s starts from a nonzero minimum value ($s_{\min} \approx 0.38$) at the nuclear cusp as shown in Fig. 3.2. Hence the region $0 \leq s \leq s_{min}$ is not well represented by the hydrogen density. However, this issue is solved by the use of cuspless hydrogen density. The angle averaged exchange hole density for this case has the following form

$$\rho_x^C(r,u) = \frac{a}{64\pi ru}\{e^{-a|r-u|}[a^2(r-u)^2+3a|r-u|+3] - e^{-a(r+u)}[a^2(r+u)^2+3a(r+u)+3]\},$$

(4.2)

which satisfies the normalization condition $\int du 4\pi u^2 \rho_x^C(r,u) = 1$, for any $a \geq 0$. The corresponding BR non-linear equation can be written as

$$\frac{(1+x)^{5/3}}{x-3}e^{-2x/3} = \Lambda(\rho, \nabla\rho, \tau),$$

(4.3)

where we have generalized the right hand side of Eq. 3.33 by a function Λ which will be defined later. Exchange energy can be calculated as

$$\begin{aligned}
E_x &= \int \rho(\mathbf{r})U_x^C(\mathbf{r})d\mathbf{r} \\
&= -\frac{(16\pi)^{1/3}}{16}\int \rho^{4/3}\frac{e^{-2x/3}(-x^2-5x+8e^x-8)}{x(1+x)^{1/3}}d\mathbf{r}
\end{aligned}$$

(4.4)

To arrive at the above equation, Eqs. 3.34 and 3.35 are used. The enhancement factor defined in Eq. 1.47 is given by

$$F_{\mathrm{x}} = \frac{1}{6}\left(\frac{2\pi^2}{3}\right)^{1/3} \frac{e^{-2x/3}(-x^2 - 5x + 8e^x - 8)}{x(1+x)^{1/3}}. \tag{4.5}$$

In order to satisfy the scaling relation described in section 1.7.1, the root x of the Eq. 4.3 and implicitly the function $\Lambda(\rho, \nabla\rho, \tau)$ must be independent of the uniform density scaling $\rho_\gamma(\mathbf{r}) = \gamma^3 \rho(\gamma \mathbf{r})$, with $\gamma \geq 0$. This constraint can be fulfilled by using the well known dimensionless ingredients $\Lambda(\rho, \nabla\rho, \tau) = \Lambda(s, \alpha)$. For the case of mBRxC-BG meta-GGA functional, the function $\Lambda(s, \alpha)$ can be written as $\Lambda(s, \alpha) = (c_1\alpha + c_2 + c_3 s^2 + c_4 s^4)^{-1}$, where the parameters c_i are fixed from the exact constraints and band gap energies of few bulk solids. However, the enhancement factor of the mBRxC-BG tends to larger values than MGE2[130] as s increases and approaches to infinity as $s \to \infty$. This behaviour of the enhancement factor worsens the ground state properties of atoms, molecules, and solids. There are some exchange functionals which are giving accurate ground state results in spite of the fact that the enhancement factor diverges when s tends to infinity but their enhancement factor is usually smaller than $F_{\mathrm{x}}^{\mathrm{MGE2}}$.[33,37,147]

Here, our functional construction using cuspless hydrogen density following the modified BR approach depends on the design of the function $\Lambda(s, \alpha)$. We consider Λ as a functional of α only without any explicit dependence on the reduced density gradient. Hence, the only ingredient of our exchange functional is the Pauli kinetic enhancement factor α. Let us take the following Padé approximation[148,149] for Λ

$$\Lambda(\alpha) = \frac{\beta_1 + \beta_2 \alpha + \beta_3 \alpha^2}{1 + \beta_4 \alpha + \beta_5 \alpha^2}, \tag{4.6}$$

where β_i are the parameters which will be determined from the following conditions

1. At first, we investigate the case with $\alpha = 0$. This type of situation arises for any one- and two-electron singlet states and $\alpha \approx 0$ at the nuclear cusp, in the non-degenerate iso-orbital region.[150,151] For the two-electron system, the value of the enhancement factor is $F_{\mathrm{x}} = 1.174$ and it is shown to be reasonably accurate for these systems.[152] Using the condition in Eq. 4.5, we get

$$\frac{e^{-2x/3}(-x^2 - 5x + 8e^x - 8)}{x(1+x)^{1/3}} = 3.7591. \tag{4.7}$$

By solving the above non-linear equation, and putting the value of x in Eq. 4.3, we will get

$$\beta_1 = 3.712. \tag{4.8}$$

2. Next, we check the limit $\alpha \to \infty$. For this case, we chose the minimum value of enhancement factor $F_x = min_x F_x(x) = 0.937$ for $x = 0$ as found from Eq. 4.5. This type of density regime, where $\alpha \to \infty$ is highly non-local and usually found at the tail of the density, when the highest occupied orbital is degenerate. This condition is closely related to the cuspless hydrogen density model and gives the following relation

$$\beta_5 = -3\beta_3. \tag{4.9}$$

3. For the homogeneous electron gas $\alpha = 1$, the enhancement factor should reduce to $F_x = 1$, in order to recover the exact LDA. This condition is very important for most of the bulk solids where $\alpha \approx 1$. Putting the value $F_x = 1$ in Eq. 4.5, we get

$$\frac{e^{-2x/3}(-x^2 - 5x + 8e^x - 8)}{x(1+x)^{1/3}} = 0.5336. \tag{4.10}$$

After solving this non-linear equation, if we put the value of x in Eq. 4.3, we will get a relation between β_2, β_3 and β_4.

$$\beta_3 = 2.595 + 0.5197\beta_4 + 0.559\beta_2. \tag{4.11}$$

4. We enforce the tight Lieb-oxford bound $F_x \leq 1.174$[52] for our proposed enhancement factor of Eq. 4.5. This condition was used in the construction of MVS[53] and

SCAN[34] meta-GGA XC functionals.

$$\beta_4 - 0.2694\beta_2 \leq 0,$$
$$\beta_2^2 - 4\beta_1\beta_3 \leq 0, \tag{4.12}$$

where $\beta_3 \geq 0$ and $\beta_2 \geq 0$, which ensures that $\Lambda \neq 0$.

5. The remaining parameters β_2 and β_4 are determined from the exchange energies of noble gas atoms and at the same time follow the inequality of Eq. 4.12. The parameters β_2 and β_4 are fixed to be 2.0 and 0.1 respectively. This procedure provides an accurate description of the semiclassical atom theory,[129] which is shown to be significant for both quantum chemistry and solid-state physics, and used in the development of some recent exchange functionals.[130] Parameter values for the MGGAC functionals are shown in Table 4.1.

Table 4.1: Shown are the parameter values for the MGGAC exchange energy functional.

β_1	β_2	β_3	β_4	β_5
3.712	2.0	3.765	0.1	-11.295

Table 4.2: Shown are the exchange energies of the noble gas atoms using spin restricted Hartree-Fock orbital and densities[153] for different XC functionals.

Atoms	HF[53]	PBE[53]	SCAN[34]	MVS[53]	MGGAC
He	-1.026	-1.014	-1.031	-1.031	-1.037
Ne	-12.109	-12.067	-12.108	-12.121	-12.157
Ar	-30.190	-29.996	-30.188	-30.127	-30.173
Kr	-93.892	-93.425	-93.890	-93.892	-93.516
Xe	-179.169	-178.24	-179.200	-179.172	-178.206

After the development of the proposed exchange functional (MGGAC), we have shown the exchange energies of the noble gas atoms in Table 4.2 and compared them with those obtained from other known exchange functionals. The results are reasonably accurate for all the noble gas atoms and comparable with the results of other popular functionals.

However, MGGAC slightly underestimates the exchange energy of the He atom. This is almost the same as the value of PBE overestimation. This fact is related to the simplest, fully local behaviour of the MGGAC exchange functional for the case of one- and two-electron system, where by construction $F_x^{MGGAC} = 1.174$.

4.2.1 Behaviour of the Exchange Enhancement Factor

We have shown the enhancement factor $F_x^{MGGAC}(\alpha)$ as a function of α in the left panel of Fig. 4.1. It is smooth and decreases monotonically from its maximum value of 1.174 at $\alpha = 0$ to its minimum value of 0.937 at $\alpha = \infty$. It also matches very well with the F_x^{MVS} for $s = 0.01$ and $\alpha \approx 1$. In the right panel of Fig. 4.1, the derivate of the enhancement factors w.r.t. α is shown for MVS and MGGAC functionals. F_x^{MGGAC} shows almost zero slope when $\alpha \to 0$ and for all other values of α, $dF_x/d\alpha \leq 0$ is a convex function. This property of the exchange functionals is directly related to the band gap of solids.[154] In general, our proposed F_x^{MGGAC} is very simple compared with the F_x^{MVS} which shows a lot of structure and dependent on both s and α.
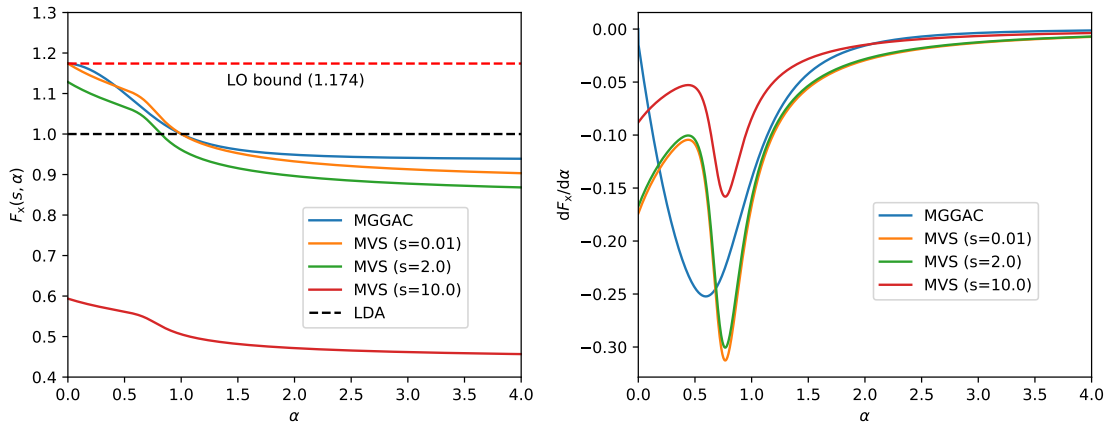
Figure 4.1: Left panel: The exchange enhancement factor F_x as a function of α for the MVS and MGGAC functionals. Right panel: Same as in the left panel but for the derivative of the enhancement factor $dF_x/d\alpha$.

4.2.2 Properties of the BR Non-linear Equation

At this point, let us discuss about the solution of the non-linear Eq. 4.3 which is very crucial for getting the exchange energy. As we have already shown in Fig. 4.1 that $F_x^{MGGAC}(\alpha)$ is smooth and this implies the well-behaved character of the non-linear equation everywhere. The equation can be solved numerically using Newton-Raphson method[155] and for any function Λ it has a unique solution $x \geq -1$. We solve the inverse of Eq. 4.3 i.e. $1/\Lambda(\alpha) = (x-3)e^{2x/3}/(1+x)^{5/3}$ in order to remove possible numerical instability at $x = 3$. We have shown in Fig. 4.2 that both $1/\Lambda(\alpha)$ and $x(\alpha)$ are analytic function of α. Notice that $x \geq 0$ always and $x \to 0$ when $\alpha \to \infty$. The computational cost of the
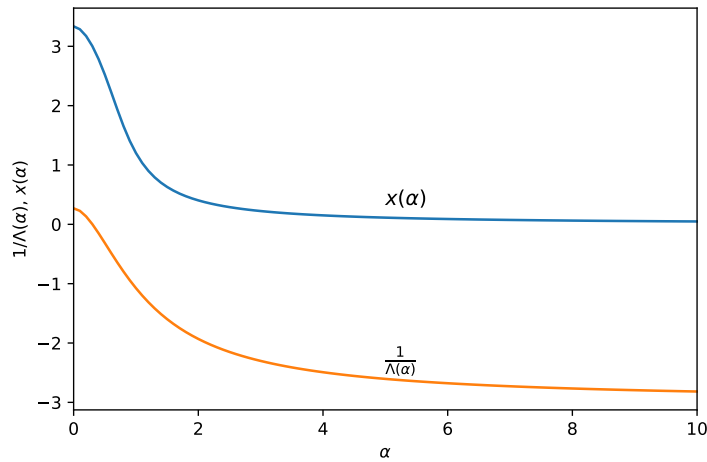
Figure 4.2: Shown are the solution $x(\alpha)$ of Eq. 4.3 and the value of $1/\Lambda(\alpha)$ of Eq. 4.6 with respect to α.

proposed functional is comparable with other meta-GGA functionals because of the good behaviour of the non-linear equation. Note that it is also possible to find an analytical representation of the MGGAC non-linear equation like the existing BR exchange.[128]

4.2.3 Correlation Part of the MGGAC Functional

For the correlation part to be associated with the proposed exchange functional, we used PBE[26] expression with modified second-order gradient coefficient β to be fixed at 0.030. We get this value of β from the fitting of equilibrium lattice constants of twenty densely

packed solids from the LC20 test set.[156] We note that the fixed value of β is very close to the LDA linear response value ($\beta = 0.0375$),[157] which is supposed to be exact in the low-density regime.[158,159]

4.3   Computational Details

The MGGAC functional is implemented in the development version of the QCHEM[160] for quantum chemistry calculations. The def2-QZVP basis set is used for all calculations and XC integrals are performed with a radial grid of 99 points and an angular Lebedev grid of 590 points. Note that meta-GGA functionals especially SCAN is very sensitive to the choice of the grid and particularly for the potential energy curves of the non-bonded interactions.[161] However, our choice of the grid is sufficient for the complete energy convergence of the non-bonded systems.

Solid-state calculations are performed by implementing the MGGAC functional in the plane wave pseudopotential code Vienna ab initio simulation package (VASP).[132,133] A $15 \times 15 \times 15$ Monkhorst-Pack k-mesh and 700 eV energy cutoff is used for all the bulk calculations including the band gap calculations. To calculate the bulk modulus of solids, we use third-order Birch-Murnaghan[162] equation of state to fit the energy-volume data. An antisymmetric box size of $23 \times 24 \times 25$ Å^3 is considered for the atomic calculation of cohesive energies. Surface energies of six transition metals and CO adsorption on the transition metal surfaces are done with $16 \times 16 \times 1$ Γ centred k-mesh and 700 eV energy cut-off. In the case of surface calculations, a vacuum of greater than 20 Åis used to avoid the interaction between the periodic surfaces. We relax the top two layers for the case of CO adsorption.

4.4   Results

4.4.1   Molecular Systems

To check the performance of MGGAC for molecular systems, we examine the following widely used thermochemical and non-covalent interaction test sets: the AE6[58] and G2/148[163] test sets for the atomization energy, the BH76RC[164] test set of thirty chemical reactions, 76 barrier heights (BH76)[164] including 38 hydrogen transfer (HTBH38) and 38 non-hydrogen[165,166] transfer barrier heights, hydrogenic (MGHBL9) and non-hydrogenic (MGNHBL11)[106] bond lengths, six hydrogen bond dissociation (HB6) energies,[58,167] binding energies of seven charge transfer complexes (CT7),[58,167] five dissociation energies (PPS5)[58,167] of π-π system, six dipolar bond dissociation energies (DI6),[58,167] seven hydrocarbon chemistry (HC7),[58,168] nine difficult cases (DC9/12),[58,169] and non-covalent interaction energies of S22[170] test set.

The MAE and RMAE w.r.t. PBE values are shown in the Table 4.3 and all the detailed results are given in the supplementary material of Ref..[54] The performance of MGGAC is quite precise for all the molecular test sets except HB6, where it has been noticed that a substantial underestimation of the hydrogen bond reaction with an MAE of 0.87 kcal/mol. The MGGAC functional outperforms the MVS and TPSS meta-GGAs with an RMAE of 0.78, and their performance is very close to SCAN (RMAE=0.78) and B3LYP (RMAE=0.74) hybrid functionals. The good performance of MGGAC for atomization energies, barrier heights, reaction energies, and difficult cases make it suitable for the thermochemistry calculations. To justify the above point, we want to mention the performance of MGGAC for the DC9/12 test set which is composed of the difficult reactions and atomization energies. MGGAC provides the best result for this case with an MAE of 6.3 kcal/mol, which is almost twice better than SCAN meta-GGA with MAE=11.1 kcal/mol. In addition, the MGGAC gives all the relative errors below 20%, and the result is very accurate for seven out of nine cases. Interestingly, the performance of MVS meta-GGA is worst in this case with an MAE of 43.8 kcal/mol.

Table 4.3: Shown are the mean absolute errors (MAE) of all the molecular test sets for different XC energy functionals. All results are in kcal/mol except for MGHBL and MGNHBL where MAEs are reported in mÅ. The last line provides the averaged MAE relative to the PBE (RMAE=$\frac{1}{N}\sum_i^N$ MAE$_i$/MAE$_i^{PBE}$, with N being the total number of test sets). The best/worst MAE result of each test set is shown in bold/underline style.[1]

	PBE	TPSS	SCAN	MVS	MGGAC	HSE06	B3LYP
AE6	<u>15.03</u>	5.74	**3.43**	10.55	5.24	5.41	3.47
G2/148	<u>15.17</u>	5.47	**3.73**	12.86	4.38	4.47	4.70
BH76	<u>9.32</u>	8.56	7.76	4.77	**3.88**	4.32	4.63
BH76RC	3.33	1.78	2.32	<u>3.49</u>	2.51	**1.60**	1.67
MGHBL9	<u>11</u>	7	**2**	3	3	**2**	**2**
MGNHBL11	7	**5**	6	<u>12</u>	10	10	7
HB6	**0.33**	0.47	0.76	0.42	<u>0.87</u>	**0.33**	0.65
CT7	2.77	1.98	<u>2.99</u>	2.18	1.60	0.95	**0.60**
PPS5	2.38	2.91	0.72	0.79	**0.67**	1.87	<u>2.98</u>
DI6	0.41	0.51	0.53	0.43	0.65	**0.35**	<u>0.84</u>
HC7	4.23	10.73	6.51	9.45	**4.10**	8.85	<u>17.00</u>
DC9/12	39.83	17.29	11.13	<u>43.82</u>	**6.35**	16.57	20.32
S22	2.54	3.41	0.92	**0.75**	1.20	2.33	<u>3.70</u>
RMAE	1.00	0.95	0.78	0.93	0.78	**0.74**	<u>1.09</u>

[1] All the details of the geometries used in the calculations and reference values can be found in the supplementary material of Ref..[54]

4.4.2 Solid-State Systems

Here, we assess the performance of the MGGAC functional for the following solid state test sets - the equilibrium lattice constants (LC20), bulk modulus (BM20) and the cohesive energies (COH20) of twenty strongly bonded solids,[34,156] the band gaps of the semiconductors from the SBG31[171] test set, the surface (111) formation energies of six transition metals (Au, Cu, Pd, Pt, Rh, and Ir), and the adsorption energies of CO molecule on top of the (111) surface of transition metals (Cu, Ir, Pd, Pt, and Rh). The results of the above test sets are reported in Table 4.4 as MAE and RMAE w.r.t the PBEsol values and the full results are given in the supplementary material of Ref..[54] Note that PBEsol is considered to be the best for many solid state calculations and we took this as a reference for computing RMAE.

The overall performance of MGGAC (RMAE=1.0) is comparable to the PBEsol func-

Table 4.4: Shown are the MAEs of the lattice constants (a_0), bulk moduli (B_0), cohesive energies (E_{coh}), band gaps (E_g), transition metal surface (111) energies (σ) and CO adsorption energies (E_{ad}) on top of the (111) surface of the five transition metals. Best/worst MAE result of each column is shown in bold/underline style. The average MAEs are shown in the last column w.r.t. PBEsol (RMAE = $\frac{1}{N}\sum_{i=1}^{N}$ MAE$_i$/MAE^{PBEsol}).[1]

	a_0 (Å)	B_0 (GPa)	E_{coh} (eV/atom)	E_g (eV)	σ (J/m^2)	E_{ad} (eV)	RMAE
LDA	<u>82</u>	10.1	0.64	<u>1.20</u>	**0.16**	<u>0.83</u>	<u>1.6</u>
PBE	60	10.5	**0.14**	1.06	<u>0.67</u>	0.31	1.2
PBEsol	35	6.2	0.25	1.16	0.37	0.50	1.0
TPSS	43	7.9	0.17	0.98	0.38	**0.18**	0.9
SCAN	**26**	**4.5**	0.16	0.75	0.46	0.51	**0.8**
MVS	34	<u>12.2</u>	0.37	0.59	0.22	0.50	1.1
MGGAC	45	10.0	<u>0.39</u>	0.52	0.21	0.28	1.0
HSE06	31	7.2	0.28	**0.28**	0.34	0.49	0.9

[1] The results (a_0, B_0 and E_{coh}) of LDA, PBE, PBEsol and TPSS are taken from Ref.,[156] SCAN, MVS and reference values are from Refs.,[172,173] and.[156] Surface energies of the LDA, PBE, PBEsol and SCAN functionals are from Ref.,[174] the TPSS ones from Ref.[173] and the reference results are from Ref..[175] Adsorption energies of PBE, SCAN, HSE06 and reference values are taken from Ref..[176]

tional and better than LDA, MVS, and PBE functionals. The SCAN meta-GGA functional performs the best for the case of lattice constants and bulk moduli. For cohesive energies, the performance of MGGAC is in line with the MVS functional and the PBE functional outperforms all others in this case. The LDA gives the lowest MAE for transition metal surface energies. On the other hand, it has the largest MAE for the CO adsorption on the transition metal surfaces. For these two cases, the performance of MGGAC is quite good and it outperforms the SCAN, MVS, PBE, PBEsol, and HSE06 functionals. MGGAC is the best performing semilocal functional for the semiconductor band gaps of the SBG31 test set. In order to highlight this point, we have shown the band structure and density of states of the Si bulk crystal calculated using MGGAC, SCAN and HSE06 functional in Fig. 4.3. The SCAN and MGGAC functionals give almost the same occupied bands, but the conduction band picture is drastically improved at the MGGAC level. The indirect band gap for MGGAC is 1.21 eV, which is comparable to the HSE06 (1.17 eV) and the experimental band gap (1.17 eV). On the other hand, SCAN underestimates the band gap

value by giving 0.83 eV in this case. Furthermore, the description of the direct band gap at the Γ point is improved for the MGGAC functional giving 3.32 eV, compared to the
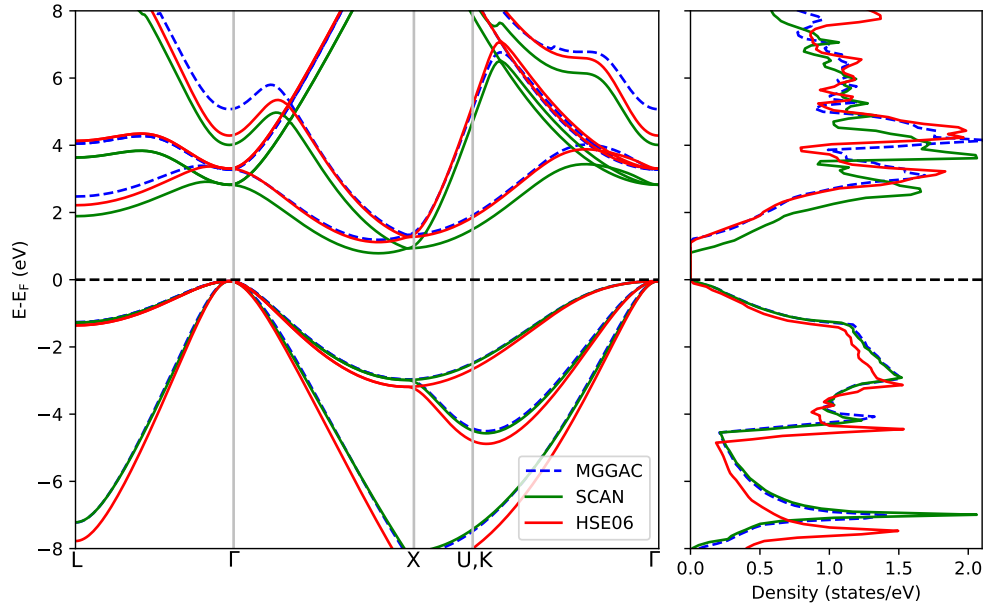
Figure 4.3: The band structure and the density of states for Si bulk crystal as calculated using MGGAC, SCAN and HSE06 hybrid functionals.

experimental value of 3.35 eV, whereas SCAN gives 2.85 eV. It is evident from 4.3 that the unoccupied part of the band and DOS in the case of MGGAC resemble very well that of the HSE06. This manifests the significant accuracy of the MGGAC functional and this can be used for multiscale simulation of Si clusters and various Si quantum dots.[177] Note that the Becke-Johnson exchange potential[178] and the Tran-Blaha modified Becke-Johnson exchange potential[134] were constructed using the Becke-Roussel technique and accurate for the band gap energy of bulk solids. Recently, the good performance of the MGGAC functional has been shown for the prediction of the band gaps of the layered materials.[179]

4.4.3 Orbital Energies of Noble Gas Atoms

Now, we study the orbital energies of noble gas atoms, from He to Rn, to check whether the good performance of the MGGAC functional also holds for the finite systems as well.

In Table 4.5, we have shown the MAEs of the highest occupied (HOMO), lowest unoc-
cupied (LUMO), and second lowest unoccupied (denoted as LUMO+1) molecular orbital
energies w.r.t. the reference values. The MGGAC functional performs exceptionally well
in this case and improves the results significantly over TPSS, SCAN, and MVS. This im-
provement of the MGGAC functional is coming from the Becke-Roussel approach used in
its construction and this procedure has been shown to be relevant for the better description
of excitation energies.[180]

Table 4.5: Shown are the MAEs (eV) of the HOMO, LUMO, and LUMO +
1 for the noble gas atoms from He to Rn. The Best/worst result of each case
is shown in bold/underline style.[1]

Orbital	PBE	TPSS	SCAN	MVS	MGGAC	HSE06	B3LYP
HOMO	<u>5.58</u>	5.47	5.18	4.91	4.76	4.28	**4.16**
LUMO	<u>2.03</u>	1.89	1.43	1.64	**0.86**	1.78	1.83
LUMO+1	2.06	1.94	1.63	<u>2.72</u>	**1.27**	1.80	1.85

[1] Reference HOMO eigenvalues are taken from the experimental ionization potential[181]
using the Koopman's theoem ($\varepsilon_{HOMO} = -IP$). Reference LUMO and LUMO+1 eigen-
values are taken from the long-range corrected hybrid functional (ωB97X-D3)[182] cal-
culation. The UGBS basis set is used. Detailed results are given in the supplementary
information of Ref..[54]

4.5   Conclusions

We have proposed an exchange functional using the Becke-Roussel approach which is
an unusual but powerful way of building exchange functional. The non-linear equation
[see Eq. 4.3] in this approach is derived using the cuspless hydrogen density. The function
$\Lambda(\rho, \nabla\rho, \tau)$ can be modelled in such a way that the resulting exchange functional will fol-
low several exact constraints. The use of cuspless density is crucial in this case, because,
unlike the hydrogen density, both the slowly and rapidly varying density regimes are well
described. We have proposed a very simple expression of $\Lambda(\alpha)$ [see Eq. 4.6] such that
the proposed MGGAC meta-GGA exchange functional depends only on the Pauli kinetic
enhancement factor α. In spite of this heavy simplification, the MGGAC functional cou-
pled with a GGA correlation performs well for a large variety of systems and properties,

and the results are comparable and often better than the more sophisticated and popular functionals. The MGGAC accuracy demonstrates that

1. further improvements of the semi-local DFT can be improved by using reduced density gradient s with α to build a more elaborated form of $\Lambda(s, \alpha)$.

2. the ingredient α which is a signature of the electron localization function, can be used as a standalone variable in DFT functional development.

Chapter 5

Structural Phase Stability of FeS$_2$, TiO$_2$ and MnO$_2$ Polymorphs

5.1 Introduction

Semilocal functionals[33,34,54] developed in recent times are quite successful in describing a large palette of solid-state and quantum chemical properties. Despite their successful application for solids, there are some challenging cases for which their performance is not up to the mark and even the newly developed meta-GGAs and hybrid functionals fail for these cases. Such a challenging solid-state problem is the correct stability prediction of the FeS$_2$, TiO$_2$, and MnO$_2$ polymorphs. Note that these are quite emerging materials from the application point of view. FeS$_2$ and TiO$_2$ are quite useful in electrocatalyst and photoelectrochemical[183,184,185,186] applications due to their suitable band gaps. MnO$_2$ has important application in battery, energy storage, and catalysis.[187,188] From the experimental results, it is established that the pyrite and rutile are the most stable configurations of FeS$_2$ and TiO$_2$, respectively. However, most of the DFT calculations using semilocal XC functionals including Hubbard-U correction (DFT+U) show the wrong prediction of the ground state of FeS$_2$ and TiO$_2$, and all the semilocal functionals fail to predict simultaneously the correct ground state for both the systems.[189,190]

These systems have been investigated using the approximations from the higher rung

of Jacob's ladder including hybrid density functionals and random phase approximation (RPA) methods. The RPA successfully predicts the stability ordering of both these solids while the HSE06[45] functional fails for the case of TiO$_2$. In general, the RPA calculations are performed on top of the semilocal functional and the final results depend on the starting orbitals.[189,190] However, the structural relaxation using the self-consistent RPA approach is not practical due to its huge cost and lack of analytic forces.

In this chapter, we investigate the relative stability of the FeS$_2$, TiO$_2$, and MnO$_2$ polymorphs using the developed functional (MGGAC) in chapter 4. We also consider the recently proposed Tao-Mo (TM)[33] and SCAN[34] meta-GGA functional to assess their performance for these challenging systems. Both the TM and SCAN functionals are accurate for a diverse range of bonding environments such as covalent, non-covalent, and hydrogen bonding. The SCAN and the MGGAC functional satisfy the tight lower bound for exchange[52] unlike the TM functional. In the next section, we briefly describe about the methods used to explore the stability ordering of the above systems.

5.2   Brief Overview of Methods

Unlike GGAs, the meta-GGA functionals can recognize different bonding environments inside a many-electron system using the electron localization indicator which depends upon the density gradient ($\nabla\rho$) and the KS kinetic energy density $\tau(\mathbf{r}) = \frac{1}{2}\sum_i |\nabla\phi_i(\mathbf{r})|^2$, where ϕ_i is the ith occupied KS orbital. In recent years, several non-empirical meta-GGA functionals have been proposed.[33,34,54] The SCAN meta-GGA functional follows seventeen known exact constraints that a meta-GGA functional can satisfy. Its enhancement factor depends upon the reduced density gradient ($s = |\nabla\rho|/(2k_F\rho)$) and the Pauli kinetic enhancement factor $\alpha = (\tau - \tau^W)/\tau^{unif}$.

The TM meta-GGA functional is constructed from the exchange hole derived using density matrix expansion and coupled with the slowly varying density gradient expansion for exchange which is important for solids. Its enhancement factor is dependent on both the meta-GGA ingredients $z = \tau^W/\tau$ and α. At this point, we want to mention about the order-of-limit[191] problem of some meta-GGA functionals. This arises due to the differ-

ent results from the order of two limiting conditions $\alpha \to 0$ and $p \to 0$ ($p = s^2$) on the exchange enhancement factor. In the case of TM functional, it can be expressed as

$$\lim_{\alpha \to 0} \left[\lim_{p \to 0} \left[F_{\mathrm{x}}^{\mathrm{TM}}(p, \alpha) \right] \right] = 1.0137, \tag{5.1}$$

and

$$\lim_{p \to 0} \left[\lim_{\alpha \to 0} \left[F_{\mathrm{x}}^{\mathrm{TM}}(p, \alpha) \right] \right] = 1.1132. \tag{5.2}$$

This problem worsens the functional performance for the transition pressure of solids and leads to inaccurate energy differences between different crystal structures.[192,193]

The MGGAC meta-GGA functional which is discussed in the previous chapter and its exchange enhancement factor depends only on the Pauli kinetic enhancement (α) factor. This functional is developed using the cuspless hydrogen density following the Becke-Roussel technique. Unlike TM functional, the SCAN and the MGGAC functionals do not suffer from the order-of-limit problem. The derivative of the exchange enhancement factor w.r.t. α is negative for both the SCAN and MGGAC functionals and this property is very important for the band gap problem.[194] This fact helps to include some amount of derivative discontinuity of the XC energy within the generalized KS scheme and this improves the description of the band gap energy of the bulk and layered systems. The SCAN and TM functionals satisfy the fourth-order gradient expansion for exchange. On the other hand, the MGGAC functional form is quite simple and recovers the LDA in the slowly varying density limit. The correlation part of the SCAN and TM is one-electron self-interaction free, whereas the MGGAC correlation follows from a simple modification of the PBE correlation functional.

Nonetheless, apart from PBE, PBEsol, and TPSS functionals, the SCAN, TM, and MGGAC meta-GGA functionals incorporate some interesting and peculiar features such as tight lower bound for exchange, the exchange hole constraint, or the Becke-Roussel non-linear equation using cuspless hydrogen density. Therefore, the study of the performance of these functionals for the challenging systems is interesting from both practical and theoretical points of view.

5.3   Computational Details

All the DFT calculations are performed using Vienna ab initio simulation package (VASP)[132,133] which is a plane wave pseudopotential based code. We have used GW tuned norm conserving projector augmented wave pseudopotentials to assure the numerical accuracy as suggested in the previous study.[190] The $3s$ and $3p$ semicore states are considered as valence states for Fe and Ti. We use a $6\times6\times6$ ($7\times6\times10$) Γ centered Monkhorst-Pack[195] k-mesh for FeS_2 pyrite (marcasite) and $6\times6\times8$ ($6\times6\times6$) for TiO_2 rutile (anatase). Plane wave cut-off of 800 eV is used for all the calculations. Structural optimization has been performed with a force convergence criteria of 0.01 eV/Å for each atom. To get the energy-volume data for a particular crystal phase, a set of crystal structures with range $V_{cell} \pm 10\%$ are optimized by relaxing their internal coordinates and crystal shape, where V_{cell} is the equilibrium unit cell volume. The obtained energy-volume data is fitted with the Birch-Murnaghan[162] equation of state to get the equilibrium volume V_{cell}, bulk modulus B_0 and ground state energy E_0.

Phonon calculations are performed using the Phonopy[196] code interfaced with VASP. A $2 \times 2 \times 2$ supercell is used for the phonon calculation and this is constructed from the optimized structure with force convergence criteria of 0.001 eV/Å for each functional. Once we get the phonon energy spectrum, the vibrational internal energy (U_{vib}) is calculated from the following equation

$$U_{vib}(T) = \sum_{\mathbf{q},n} \hbar\omega(\mathbf{q},n) \left[\frac{1}{2} + \frac{1}{\exp(\hbar\omega(\mathbf{q},n)/k_B T) - 1} \right], \qquad (5.3)$$

where n is the band index and k_B is the Boltzmann constant. The enthalpy difference (ΔH) between the two phases of a particular crystal structure at temperature T and pressure P is given by

$$\Delta H = \Delta E + \Delta U_{vib}(T) + p\Delta V, \qquad (5.4)$$

where ΔE and ΔV are the energy and volume differences between the two phases. The last term of Eq. 5.4 has a very little contribution to our case and can be safely ignored.[189]

5.4   Results

5.4.1   Relative Stability of FeS$_2$ Polymorphs

5.4.1.1   Structural Properties, Relative Energies, and Band Gaps

FeS$_2$ pyrite exhibits rock salt structure with space group $pa\bar{3}$ and its conventional unit cell contains four units of FeS$_2$. In pyrite, the FeS$_6$ octahedra share corners with 12 neighbours. The marcasite phase crystallizes in the orthorhombic space group $pnnm$ and its conventional unit cell contains two units of FeS$_2$. In this phase, the FeS$_6$ octahedra shares edges along the unit cell c-axis and corners along with other directions. Marcasite is more loosely packed than pyrite.

The equilibrium volume V_{cell} and bulk modulus B_0 results are shown in Table 5.1 for both the marcasite and pyrite phases, calculated using different XC functionals. Although we have shown the results of many different functionals including widely used GGAs, meta-GGAs and hybrids, here we mainly discuss the performance of the MGGAC, SCAN, and TM meta-GGA functionals. The energy vs volume curve for both the phases using MGGAC and TM functional is shown in Fig. 5.1. Examining the performance, we notice that the TM functional underestimates the volume of the marcasite phase by 2.4% and that of pyrite by 2.8%, while the MGGAC and SCAN perform well and give values within 0.5% close to the experimental value. In the case of bulk moduli, TM functional overestimates the pyrite phase by 5.6% and marcasite phase by 9.3%, while the MGGAC functional underestimates by 12.7% and 5.3% for the pyrite and marcasite phases, respectively. The most precise results for bulk moduli are found from the PBE and TPSS functionals, and the error lies within 3% of the experimental value.

The relative energy difference between the pyrite and marcasite phase ΔE_{P-M} is shown in Table 5.1, which is calculated from the ground state energy of each phase for the respective functionals. Although the AM05, PBEsol, TPSS, MS2, and HSE06 give the required ordering (i.e. $\Delta E_{P-M} < 0$), but their ΔE_{P-M} values are deviated too much w.r.t. the experimental enthalpy. The inclusion of van der Waals interaction also gives in-

Table 5.1: Shown are the equilibrium volume of the unit cell V_{cell}, bulk modulus B_0 and band gap value E_g of the pyrite (P) and marcasite (M) phases of FeS_2 calculated using different XC functionals. The relative energy difference (ΔE_{P-M}) between the two phases and the enthalpy difference (ΔH_{P-M}) calculated by adding the zero point energy (ZPE) to (ΔE_{P-M}) are also shown.[1]

Functional	V_{cell}(Å^3)		B_0(GPa)		ΔE_{P-M}	ΔH_{P-M}	E_g (eV)	
	P	M	P	M	(meV/f.u)	(meV/f.u)	P	M
MGGAC	159.59 (0.5)	81.52 (0.01)	135.8 (-12.7)	138.7 (-5.3)	-28.03	-23.08	1.49	1.89
SCAN	158.64 (-0.1)	81.16 (-0.4)	145.6 (-6.4)	148.1 (1.1)	61.70	[60.30]	1.23	1.64
TM	154.42 (-2.8)	79.55 (-2.4)	164.3 (5.6)	160.18 (9.3)	-39.38	-37.41	0.56	1.24
TPSS	158.20 (-0.4)	81.54 (0.04)	155.6 (0.06)	149.9 (2.3)	-8.10	-5.82	0.54	1.16
RTPSS	155.11 (-2.3)	80.03 (-1.8)	161.9 (4.1)	155.9 (6.4)	-16.5	[-15.10]	0.46	1.18
MS2	159.99 (0.7)	81.98 (0.6)	140.6 (-9.6)	140.8 (-3.9)	-11.74	[-10.34]	1.54	1.89
AM05	150.06 (-5.5)	77.53 (-4.9)	182.9 (17.6)	172.5 (17.7)	-5.22	[-59.80]	0.23	0.98
PBE	157.97 (-0.5)	81.52 (0.01)	157.0 (1.0)	149.3 (1.9)	27.90	29.50	0.67	0.86
PBEsol	151.10 (-4.9)	78.02 (-4.3)	182.7 (17.5)	172.5 (17.7)	-4.50	-3.10	0.64	0.83
HSE06	159.23 (0.2)	81.26 (-0.3)	133.8 (-13.9)	135.8 (-7.3)	-5.20	[-3.8]	2.80	2.70
optB88-vdW	160.38 (1.0)	82.69 (1.4)	153.6 (-1.2)	145.8 (-0.5)	25.5	[26.9]	0.79	1.01
Exp.	158.82[197]	81.51[197]	155.5[198]	146.5[199]		-42.9 ± 0.2[201]	0.70, 2.62[202,203,204,205,206]	0.34[200]

[1] The PBE, PBEsol, HSE06, and optB88-vdW values are taken from Ref.[189] The relative errors (%) of the calculated V_{cell} and B_0 are given in the parentheses. Square bracket in the ΔH_{P-M} column indicates that the ZPE of the PBEsol functional from Ref.[189] is used to calculate the enthalpy difference.

correct ordering, which is obvious from the optB88-vdW results. The MGGAC and TM functionals correctly predict the pyrite phase as the stable one and they give ΔE_{P-M} and ΔH_{P-M} values that are comparable to the experimental values. Notice that even if SCAN is very successful for a wide range of molecular and solid-state systems,[207] still it gives incorrect ordering in this case.

We have compared the calculated band gap results of both the phases using semilocal functionals with the results of hybrid functional and experimental values. The experimentally reported optical band gap varies from 0.70 to 2.62 eV in the case of pyrite.[205] In the case of marcasite, all the semilocal functionals significantly overestimate the value of band gap as compared to the experimental value of 0.34 eV. We find that the MGGAC and MS2 functionals are most accurate in this case and their values are in better agreement with the reference to HSE06 hybrid functional. The larger difference between the calculated band gap of marcasite from the experiment suggests that the experimental resistivity measurement may need to be verified carefully.[208]
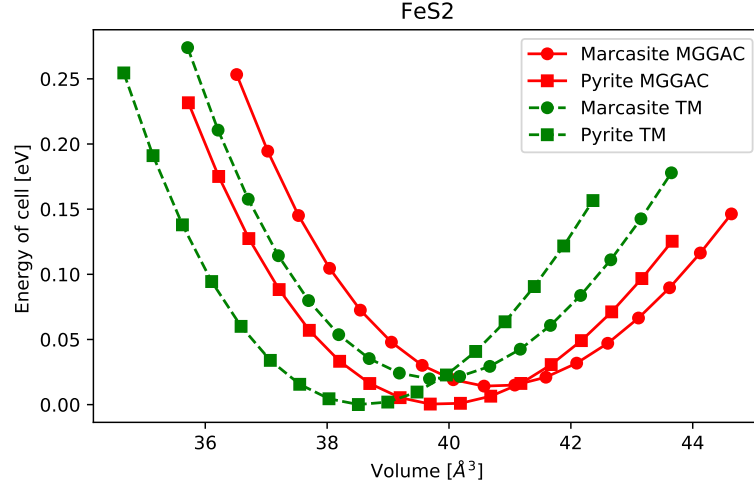
Figure 5.1: Energy vs volume curves for both the phases of FeS_2 calculated using the MGGAC and TM functionals. Zero of the energy is taken as the total energy of the pyrite phase at the equilibrium volume of each functional.

5.4.1.2 Temperature Effects and Zero-Point Energy

Here, we explore the impact of the vibrational energy and temperature on the relative stability of the marcasite and pyrite phases of FeS_2. The calculated value of $\Delta H_{\mathrm{P-M}}$ for each functional is shown in Table 5.1. The density of states for each phase calculated using the MGGAC and TM functional is shown in the left panel of Fig. 5.2. The largest phonon peak for marcasite is observed around 445 cm^{-1} and around 488 cm^{-1} for pyrite using MGGAC functional and the same for TM functional is observed around 429 cm^{-1} and 451 cm^{-1}, respectively. Due to this reason, the zero-point energy of the pyrite phase is larger than the marcasite phase irrespective of the functional used.[209] After adding the zero point energy contribution to $\Delta E_{\mathrm{P-M}}$, the MGGAC functional underestimates the experimental enthalpy by 19.8 meV per formula unit and TM functional by 5.5 meV per formula unit. The enthalpy change $\Delta H_{\mathrm{P-M}}$ at any finite temperature is calculated using the Eq. 5.3 and shown in the right panel of Fig. 5.2 for the MGGAC and TM functionals, along with the experimental results. Within a temperature range of $0-700$ K, the experimental enthalpy change from pyrite to marcasite phase is decreased by 0.4 meV per formula unit. However, from our DFT calculations, it is decreased by 4.0 meV and 1.5 meV for
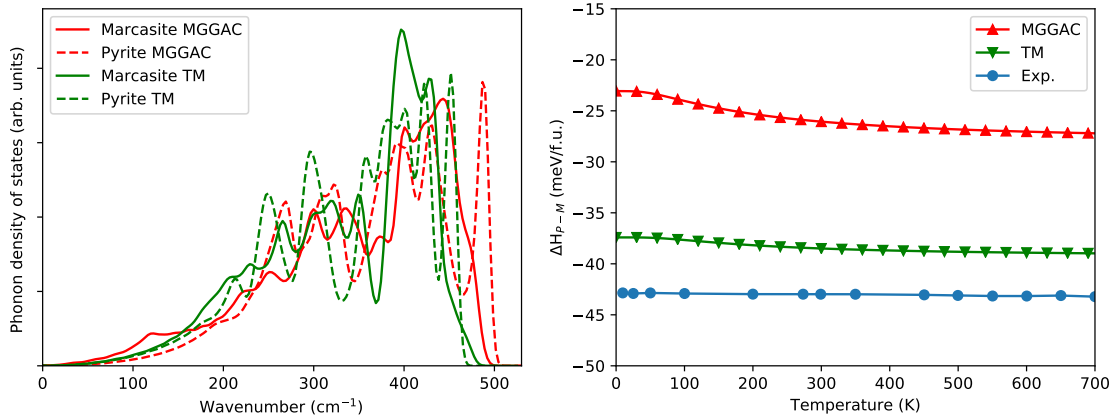
Figure 5.2: Left panel: Phonon density of states of the pyrite and marcasite phases calculated using the MGGAC and TM functionals. Right Panel: Calculated and experimental enthalpy changes from pyrite to marcasite phases within temperature range $0 - 700$ K. Experimental results are taken from.[201]

the MGGAC and TM functional, respectively. Both the MGGAC and TM functionals correctly predict the pyrite phase as the most stable one within the above temperature range and being in line with the experiment.

5.4.2 Relative Stability of TiO$_2$ Polymorphs

5.4.2.1 Structural Properties, Relative Energies, and Band Gaps

TiO$_2$ rutile and anatase crystallize in the space group *I*4$_1$/*amd* and *P*4$_2$/*mnm*, respectively. The basic building block is TiO$_6$ octahedron for both the structures, but the connection between these octahedrons is different in the two phases. The rutile phase is more densely packed than the anatase phase. The equilibrium volume and bulk modulus of the anatase and rutile phases using all the considered functionals are shown in Table 5.2. The energy vs volume curve for both the phases using MGGAC and TM functional is shown in Fig. 5.3. It is evident from Table 5.2 that the PBE functional overestimates the volume of both the phases by less than 2.9%, whereas MGGAC, HSE06, and PBEsol underestimate them by less than 1.8%. All of the other functionals give the unit cell volume with good accuracy compared to the experiment. For the case of bulk moduli, the TM and

TPSS functionals provide accurate results, whereas the MGGAC and SCAN functionals overestimate for both rutile and anatase phases.

Table 5.2: The equilibrium volume of the unit cell V_{cell}, bulk modulus B_0 and band gap E_g of the rutile and anatase phases of TiO_2 calculated using different XC functionals. The relative energy difference (ΔE_{R-A}) between the two phases and the enthalpy difference (ΔH_{R-A}) computed by adding the zero point energy to ΔE_{R-A} are also shown.[1]

Functionals	$V_{cell}(\text{Å}^3)$		B_0(GPa)		ΔE_{R-A}	ΔH_{R-A}	E_g (eV)	
	R	A	R	A	(kJ/mol)	(kJ/mol)	R	A
MGGAC	61.34 (-1.8)	67.18 (-1.4)	257.8 (19.3)	197.9 (11.2)	-0.82	-0.74	2.46	2.79
SCAN	62.14 (-0.5)	68.46 (0.5)	242.9 (12.4)	191.5 (7.6)	6.85	[6.01]	2.22	2.60
TM	62.83 (0.6)	68.69 (0.8)	222.1 (2.8)	182.6 (2.6)	-2.01	-2.89	2.00	2.23
TPSS	63.16 (1.1)	69.45 (1.9)	213.7 (-1.1)	175.4 (-1.5)	12.16	11.11	1.97	2.28
RTPSS	63.06 (1.0)	69.20 (1.6)	216.9 (0.4)	173.7 (-2.4)	7.31	[6.47]	1.99	2.26
MS2	62.39 (-0.1)	68.47 (0.5)	224.7 (4.0)	185.8 (4.4)	10.18	[9.26]	2.21	2.53
AM05	62.06 (-0.6)	68.06 (-0.1)	213.8 (-1.0)	179.1 (0.6)	18.58	[17.74]	1.87	2.18
PBE	63.97 (2.4)	70.10 (2.9)	199.1 (-7.8)	171.1 (-3.9)	9.28	[8.44]	1.84	2.12
PBEsol	61.98 (-0.7)	67.96 (-0.2)	220.9 (2.3)	179.6 (0.9)	5.95	5.11	1.85	2.10
HSE06	61.80 (-1.0)	67.86 (-0.4)	232.9 (7.8)	199.5 (12.1)	8.74	[7.90]	3.45	3.73
optB88-vdW	62.83 (0.6)	68.75 (0.9)	215.7 (-0.1)	173.9 (-2.3)	1.35	[0.51]	1.88	2.19
Exp.	62.45[210]	68.13[210]	216[211]	178[212]		-1.69[213]	3.00[214]	3.20[215]

[1] The PBE, PBEsol, HSE06, and optB88-vdW values are taken from Ref..[190] The relative errors (%) of the calculated V_{cell} and B_0 are given in the parentheses. Square bracket in the ΔH_{P-M} column indicates that the ZPE of the PBEsol functional from Ref.[190] is used to calculate the enthalpy difference.
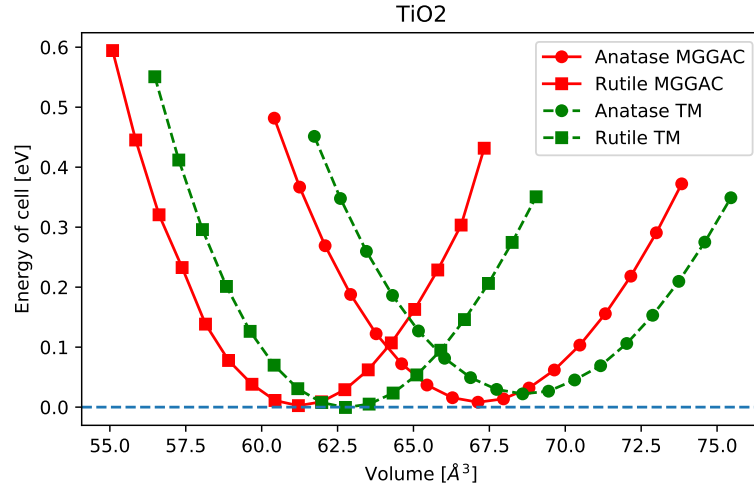

Figure 5.3: Energy vs volume curves for both the phases of TiO_2 calculated using the MGGAC and TM functionals. Zero of the energy is taken as the total energy of the rutile phase at the equilibrium volume of each functional.

Coming to the point of relative energy difference from the ground state calculation, we

observe that all the functionals except MGGAC and TM failed to predict the rutile phase as the stable one. Moreover, the TM and MGGAC values of ΔE_{R-A} are comparable to the experiment. Note that, in this case, the inclusion of van der Waals interaction reduces the energy difference in comparison with the standard GGA functionals, but still fails to predict the correct ordering.

We find that the MGGAC is the most accurate semilocal functional in predicting the band gaps of both the phases and it underestimates the values by around 0.5 eV compared to the experiment. The performance of MGGAC is comparable to the accuracy of hybrid functional HSE06, which overestimates the experimental values by about 0.5 eV.

5.4.2.2   Temperature Effects and Zero-Point Energy

Here, we discuss the impact of zero-point energy and temperature on the relative stability of the rutile and anatase phases of TiO_2. The phonon density of states of both the phases using the MGGAC and TM functionals is shown in the left panel of Fig. 5.4. In the case of MGGAC functional, the lowest energy peak in the phonon spectrum appears at about 173 cm^{-1} for anatase and 189 cm^{-1} for rutile. This small difference in the peak position makes the zero-point energy almost the same for both the phases and favours the anatase by 0.08 kJ/mol. For TM functional, the lowest energy peak for anatase and rutile phases appears at about 138 cm^{-1} and 128 cm^{-1} respectively, which stabilizes the rutile phase by 0.88 kJ/mol. Note that, we have used the highest energy peak for FeS_2 and the lowest energy peak for TiO_2 to explain the zero-point energy difference between the two phases. This is due to the density of states being large at the lowest peak position in TiO_2, whereas for FeS_2 at the highest peak position. The calculated value of enthalpy difference ΔH_{R-A} is shown in Table 5.2. We also noticed that only zero-point energy is not sufficient to change the ordering predicted by density functionals.

Using the phonon spectrum, we calculated the temperature dependence of ΔH_{R-A} as shown in the right panel of Fig. 5.4 for the case of the MGGAC and TM functionals, along with the experimental results. The experimental enthalpy change from the rutile to anatase phase is changed by 0.1 kJ/mol over a temperature range of $0 - 300$ K. However, from our theoretical calculations, it is changed by 0.47 kJ/mol and 0.12 kJ/mol for the
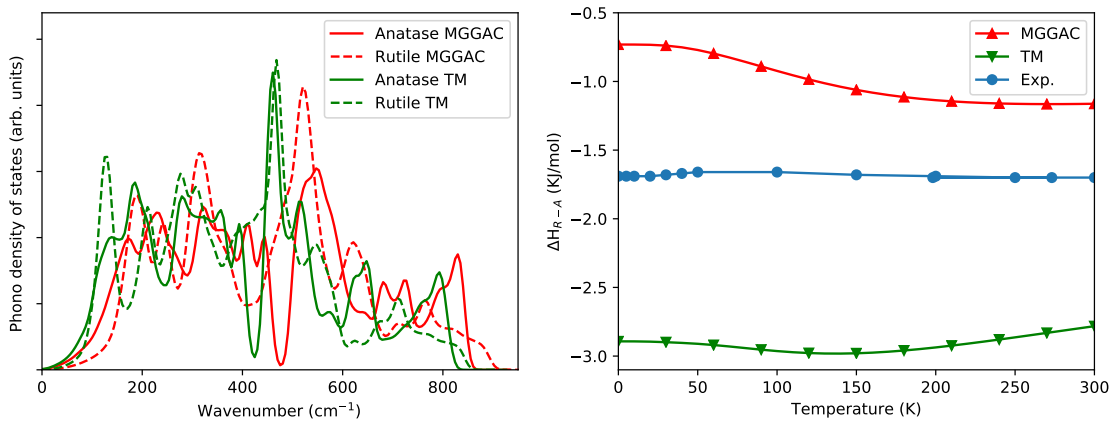
Figure 5.4: Left panel: Phonon density of states of the rutile and anatase phases calculated using the MGGAC and TM functionals. Right panel: Calculated and experimental enthalpy changes from rutile to anatase phases within temperature range $0-300$ K. Experimental results are taken from Ref..[213]

case of the MGGAC and TM functional, respectively.

5.4.3 Relative Stability of MnO$_2$ polymorphs

MnO$_2$ have six different phases which are pyrolusite β, ramsdellite R, hollandite α, intergrowth γ, spinel λ and layered δ. In all these phases, MnO$_6$ octahedrons are arranged in corner- and edge-sharing manner with the Mn^{4+} ions in the spin-polarized 3d^3 configuration and O^{2-} ions in the spin-unpolarized 2p^6 configuration. The various packing of these octahedrons will lead to different kinds of polymorphs. These materials find a very useful application in catalysis and energy storage devices.[187,216,217] Experimentally, it is confirmed that the pyrolusite β-MnO$_2$ is the ground state of pure MnO$_2$,[218] but most of the semilocal functionals and even hybrid functionals fail to predict the correct stability ordering of these phases.[219,220] All the MnO$_2$ phases discussed here are exhibiting antiferromagnetic ordering and the chosen supercells are compatible with the antiferromagnetic ordering and same as Ref..[220] The MGGAC and the SCAN functionals correctly predict the β-MnO$_2$ as the ground state among the MnO$_2$ polymorphs and the TM functional fails in this case by predicting γ-MnO$_2$ as the ground state. The formation enthalpy of R-MnO$_2$ with respect to βMnO$_2$ from the SCAN and MGGAC functionals agree quanti-
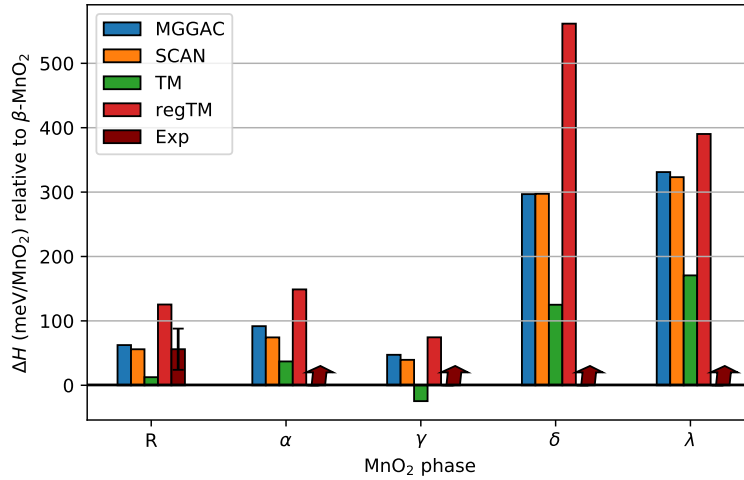
Figure 5.5: Shown are the formation enthalpies ($\Delta H = E_{R,\alpha,\gamma,\delta,\lambda} - E_\beta$) of the MnO$_2$ polymorphs w.r.t. the β-MnO$_2$. Note, the arrows drawn for the experimental formation energies for the α, γ, δ and λ phases indicate that the experimental formation energies are some unknown positive quantity.

tatively with the experiment (56 ± 32 meV/MnO$_2$). The failure of TM functional in this case can be rectified by the use of the order-of-limit free TM functional which is shown in Fig. 5.5.

5.5 Explanation of Results

At this point, let us discuss about the explanation of the above described results. Our study clearly indicates that the MGGAC and TM functionals not only correctly predict the phase ordering but also provide realistic phase transition enthalpies. The GGA functionals like PBEsol and AM05 correctly recover the phase ordering for FeS$_2$ but fail for TiO$_2$. A very similar performance is seen for the meta-GGA functionals like TPSS and RTPSS. The SCAN and MGGAC exchange functionals follow the tight Lieb-Oxford bound, hence their performances may be correlated with their different behaviour for slowly varying density regimes.

Recently, it is observed that the SCAN functional recovers the correct phase ordering for TiO$_2$ at high temperature.[221] To check that the SCAN source of errors are not coming

from the corresponding XC potentials, we also compute the stability ordering of FeS_2 and TiO_2 using rSCAN,[222] r^2SCAN[223] and its different deorbitalized forms SCAN-L[224] and r^2SCAN-L.[225] The results are shown in Table 5.3 and all the revised SCAN methods fail remarkably.

Table 5.3: Relative phase stability of FeS_2 and TiO_2 polymorphs using different modifications of the SCAN functional and their deorbitalized versions.

	rSCAN	r^2SCAN	SCAN-L	r^2SCAN-L
FeS_2(meV/f.u.)	39.07	35.08	50.50	35.03
TiO_2(kJ/mol)	8.04	8.10	5.02	6.28

Finally, the dramatic failure of TM functional in predicting the structural phase stability of MnO_2 can be understood from the order-of-limit problem of this functional.[191,193] In fact, the proposed order-of-limit free TM functional (reg-TM)[193] solves the problem and predicts the correct phase ordering qualitatively. The reg-TM functional overestimates the experimental transition enthalpy from β-MnO_2 to R-MnO_2 and for other cases also it overestimates the formation energies compared to the MGGAC and SCAN functionals as shown in Fig. 5.5.

5.6 Conclusions

We have assessed the performance of different levels of semilocal and hybrid density functional approximations in predicting the relative phase stability of FeS_2, TiO_2, and MnO_2 polymorphs. These are known to be challenging systems for density functional approximations. Most of the XC functionals including SCAN and van der Waals corrected functional fail to predict the correct stability ordering of these systems simultaneously. The present study shows that only the MGGAC functional developed using a generalized Becke-Roussel model recovers the correct stability ordering of all the systems. The MGGAC functional can also predict the band gap of narrow and intermediate band gap semiconductors with good accuracy, hence it can be used for different solid-state applications. Further, the good performance of TM functional for FeS_2 and TiO_2 can be regarded as fortuitous because of its order-of-limit problem which is evident in the case of MnO_2.

Our study shows that the performance of MGGAC is promising for these challenging systems and can be further explored in combination with the higher-order RPA based correlation methods.

Chapter 6

Summary and Discussion

We started the thesis by describing various wave function-based methods to solve the many-electron Schrödinger equation. However, the computational cost of these methods is very high. In contrast, the computational effort in density functional theory is much lower by making use of the electron density to describe the interacting many-particle system. The fundamental theorem of DFT was postulated by Hohenberg and Kohn in 1964 and its practical application is possible after the Kohn-Sham (KS) formalism which maps the interacting many-body system into an effective auxiliary non-interacting system. The effective potential which is also called the KS potential includes the external potential and electron-electron interaction in terms of the Hartree and exchange-correlation potential. For practical calculation, we need to approximate the exchange-correlation part of the KS potential. This thesis is dedicated to the development and application of the exchange-correlation (XC) functional both at the semilocal meta-GGA and range-separated hybrid meta-GGA level.

In chapter 2, we have constructed a long-range corrected exchange energy functional using the recently proposed Tao-Mo semilocal exchange hole by using the standard error function technique. The proposed long-range corrected exchange functional in combination with LYP correlation, is applied to calculate various molecular properties. We have also discussed the impact of one- and many-electron self-interaction error and the asymptotic corrected $(-1/r)$ potential for a finite system. The developed long-range cor-

rected functional performs reasonably well in comparison with the other popularly known functionals in this category.

In chapter 3, we have looked at the problem of band gap prediction from semi-local functionals perspective, keeping in mind that the meta-GGA functionals include some amount of derivative discontinuity which is important in this case. We have developed two exchange functionals using the model hydrogen and cuspless hydrogen density following the Becke-Roussel procedure. It is shown that the cuspless hydrogen density is more suitable for functional development than the hydrogen density. The developed functional using cuspless density performs better than the other semilocal functionals and gives comparable results with the hybrid functional, in the case of solid-state band gap prediction.

In chapter 4, we have developed an exchange energy functional which is dependent only on the Pauli kinetic energy density and follows some exact constraints of XC energy functional. Coupled with a GGA correlation, the proposed exchange functional works very well for a broad range of molecular and solid-state properties. Our study shows that the Pauli kinetic energy density can be the standalone ingredient for the DFT XC functional development.

In chapter 5, we have applied the developed functional in chapter 4, to the case of phase stability of the FeS_2, TiO_2, and MnO_2 polymorphs. It is shown that the MGGAC functional correctly recovers the stability ordering of all the polymorphs.

Our study will help to understand the performance of the recently proposed meta-GGA functionals and the range-separated functionals. It also helps to further develop new functionals with greater accuracy.

Appendix A

Density Matrices

The concept of density matrices is very useful in DFT, specifically when it comes to the point of designing the exchange energy functional using the density matrix expansion technique or the Taylor series expansion of the exchange hole. If we have N electron wavefunction $\psi(\mathbf{x}_1, \mathbf{x}_2, \cdots, \mathbf{x}_N)$ in the coordinate representation, then the Nth order density matrix is defined as

$$\gamma_N(\mathbf{x}_1'\mathbf{x}_2' \cdots \mathbf{x}_N', \mathbf{x}_1\mathbf{x}_2 \cdots \mathbf{x}_N) = \psi(\mathbf{x}_1', \mathbf{x}_2', \cdots, \mathbf{x}_N') \psi^*(\mathbf{x}_1, \mathbf{x}_2, \cdots, \mathbf{x}_N). \tag{A.1}$$

The reduced density matrix of mth order is defined by

$$\gamma_m(\mathbf{x}_1'\mathbf{x}_2' \cdots \mathbf{x}_m', \mathbf{x}_1\mathbf{x}_2 \cdots \mathbf{x}_m) = \binom{N}{m} \int \cdots \int \gamma_N(\mathbf{x}_1'\mathbf{x}_2' \cdots \mathbf{x}_m'\mathbf{x}_{m+1} \cdots \mathbf{x}_N, \mathbf{x}_1\mathbf{x}_2 \cdots \mathbf{x}_N)$$
$$\tag{A.2}$$
$$d\mathbf{x}_{m+1} \cdots d\mathbf{x}_N,$$

where $\binom{N}{m}$ is the binomial coefficient. The most important 2nd and 1st order reduced density matrices are given as

$$\gamma_2(\mathbf{x}_1'\mathbf{x}_2', \mathbf{x}_1\mathbf{x}_2) = \frac{N(N-1)}{2} \int \cdots \int \psi(\mathbf{x}_1'\mathbf{x}_2'\mathbf{x}_3 \cdots \mathbf{x}_N) \psi^*(\mathbf{x}_1\mathbf{x}_2\mathbf{x}_3 \cdots \mathbf{x}_N) d\mathbf{x}_3 \cdots d\mathbf{x}_N,$$
$$\tag{A.3}$$

and,

$$\gamma_1(\mathbf{x}_1',\mathbf{x}_1) = N \int \cdots \int \psi(\mathbf{x}_1'\mathbf{x}_2\cdots\mathbf{x}_N)\psi^*(\mathbf{x}_1\mathbf{x}_2\cdots\mathbf{x}_N)d\mathbf{x}_2\cdots d\mathbf{x}_N. \qquad (A.4)$$

If we sum over the spin coordinates, then the 2nd and 1st order spinless reduced density matrices are written as

$$\rho_2(\mathbf{r}_1'\mathbf{r}_2',\mathbf{r}_1\mathbf{r}_2) = \sum_{\sigma_1,\sigma_2} \gamma_1(\mathbf{x}_1'\mathbf{x}_2',\mathbf{x}_1\mathbf{x}_2), \qquad (A.5)$$

and,

$$\rho_1(\mathbf{r}_1',\mathbf{r}_1) = \sum_{\sigma_1} \gamma_1(\mathbf{x}_1',\mathbf{x}_1). \qquad (A.6)$$

Using this 1st order reduced density matrix, the exchange energy can be expressed as

$$E_{\mathrm{x}} = -\frac{1}{4} \int \int \frac{|\rho_1(\mathbf{r}_1,\mathbf{r}_2)|^2}{|\mathbf{r}_1-\mathbf{r}_2|} d\mathbf{r}_1 d\mathbf{r}_2. \qquad (A.7)$$

Appendix B

Functional Derivative of the Modified Becke-Roussel model

The self-consistent implementation of the meta-GGA functionals is given in Ref..[156] Here, we only give the derivatives needed for the implementation of the functional. The modified version of the BR exchange potential depends on the density, gradient of density and kinetic energy density. Hence it can be implemented using the generalized Kohn-Sham (gKS) formalism. The required functional derivatives of the BR exchange functional is given in Ref..[226] Here, we discuss about the functional derivatives involved in our calculation. In the gKS framework, the exchange potential is given by-

$$V_{x\sigma}\phi_{i\sigma}^{KS} = \frac{\partial}{\partial\rho_\sigma}\left(\frac{1}{2}\rho_\sigma U_{X\sigma}\right)\phi_{i\sigma}^{KS} - \nabla\cdot\left[\frac{\partial}{\partial\nabla\rho_\sigma}\left(\frac{1}{2}\rho_\sigma U_{X\sigma}\right)\phi_{i\sigma}^{KS} + \frac{\partial}{\partial\tau_\sigma^{KS}}\left(\frac{1}{2}\rho_\sigma U_{X\sigma}\right)\nabla\phi_{i\sigma}^{KS}\right]$$
$$+ \left[\frac{\partial}{\partial\nabla\rho_\sigma}\left(\frac{1}{2}\rho_\sigma U_{X\sigma}\right)\right]\cdot\nabla\phi_{i\sigma}^{KS} \tag{B.1}$$

and the exchange energy is given as follows-

$$\begin{aligned}
E_x &= \frac{1}{2}\sum_{i=1}^{\sigma}\int \rho_\sigma(\mathbf{r})U_{X\sigma}\, d^3r, \\
&= \sum_{i=1}^{\sigma}\int G[\rho_\sigma, x]\, d^3r, \tag{B.2}
\end{aligned}$$

For our modified BR functionals, the form of G can be constructed from Eqs. 3.22, 3.34, and 4.4. We need to calculate $\frac{\partial G}{\partial \rho_\sigma}$, $\frac{\partial G}{\partial |\nabla \rho_\sigma|}$ and $\frac{\partial G}{\partial \tau_\sigma^{KS}}$ separately. Now, following the chain rule, we can write

$$
\begin{aligned}
\frac{\partial G}{\partial \rho_\sigma} &= \frac{\partial G}{\partial \rho_\sigma} + \frac{\partial G}{\partial x}\frac{\partial x}{\partial \rho_\sigma}, \\
\frac{\partial G}{\partial |\nabla \rho_\sigma|} &= \frac{\partial G}{\partial |\nabla \rho_\sigma|} + \frac{\partial G}{\partial x}\frac{\partial x}{\partial |\nabla \rho_\sigma|}, \\
\frac{\partial G}{\partial \tau_\sigma^{KS}} &= \frac{\partial G}{\partial \tau_\sigma} + \frac{\partial G}{\partial x}\frac{\partial x}{\partial \tau_\sigma^{KS}}.
\end{aligned}
\tag{B.3}
$$

To calculate the value of $\frac{\partial x}{\partial \rho_\sigma}$, $\frac{\partial x}{\partial |\nabla \rho_\sigma|}$ and $\frac{\partial x}{\partial \tau_\sigma^{KS}}$, we need to consider the non-linear equation [see Eqs. 3.20 and 3.33] which in general can be written as

$$
f(x) = h\left[\rho_\sigma, |\nabla \rho_\sigma|, \tau_\sigma^{KS}\right].
\tag{B.4}
$$

Now,

$$
\frac{df(x)}{dx} = \frac{\partial h}{\partial \rho}\frac{\partial \rho}{\partial x},
\tag{B.5}
$$

which implies that

$$
\frac{\partial x}{\partial \rho} = \frac{\partial h}{\partial \rho} \bigg/ \frac{df(x)}{dx}.
\tag{B.6}
$$

Similarly, we get

$$
\frac{\partial x}{\partial |\nabla \rho_\sigma|} = \frac{\partial h}{\partial |\nabla \rho_\sigma|} \bigg/ \frac{df(x)}{dx},
\tag{B.7}
$$

and

$$
\frac{\partial x}{\partial \tau} = \frac{\partial h}{\partial \tau} \bigg/ \frac{df(x)}{dx}.
\tag{B.8}
$$

This procedure can be applied to any BR-like functional to calculate its derivatives which are needed to calculate the exchange potential.

References

[1] M. Born and R. Oppenheimer, *Annalen der Physik*, **389**, 457–484 (1927).

[2] J. C. Slater, *Phys. Rev.*, **34**, 1293–1322 (1929).

[3] C. C. J. Roothaan, Lester M. Sachs, and A. W. Weiss, *Rev. Mod. Phys.*, **32**, 186–194 (1960).

[4] S. L. Kahalas and R. K. Nesbet, *The Journal of Chemical Physics*, **39**, 529–544 (1963).

[5] Paul E. Cade, K. D. Sales, and Arnold C. Wahl, *The Journal of Chemical Physics*, **44**, 1973–2003 (1966).

[6] Richard M. Stevens and William N. Lipscomb, *The Journal of Chemical Physics*, **40**, 2238–2247 (1964).

[7] L. H. Thomas, *Mathematical Proceedings of the Cambridge Philosophical Society*, **23**, 542–548 (1927).

[8] E. Fermi, *Zeitschrift für Physik*, **48**, 73–79 (1928).

[9] Paul Adrien Maurice Dirac and Ralph Howard Fowler, *Proceedings of the Royal Society of London. Series A, Containing Papers of a Mathematical and Physical Character*, **123**, 714–733 (1929).

[10] P. Hohenberg and W. Kohn, *Phys. Rev.*, **136**, B864–B871 (1964).

[11] Mel Levy, *Phys. Rev. A*, **26**, 1200–1208 (1982).

[12] W. Kohn and L. J. Sham, *Phys. Rev.*, **140**, A1133–A1138 (1965).

[13] Robert G. Parr and Weitao Yang. *Density-Functional Theory of Atoms and Molecules (International Series of Monographs on Chemistry)*. Oxford University Press, USA, 1994. ISBN: 0195092767.

[14] John P. Perdew and Karla Schmidt, *AIP Conference Proceedings*, **577**, 1–20 (2001).

[15] E. Engel and R.M. Dreizler. *Density Functional Theory: An Advanced Course*. Theoretical and Mathematical Physics. Springer Berlin Heidelberg, 2011. ISBN: 9783642140907.

[16] D. M. Ceperley and B. J. Alder, *Phys. Rev. Lett.*, **45**, 566–569 (1980).

[17] S. H. Vosko, L. Wilk, and M. Nusair, *Canadian Journal of Physics*, **58**, 1200–1211 (1980).

[18] J. P. Perdew and Alex Zunger, *Phys. Rev. B*, **23**, 5048–5079 (1981).

[19] John P. Perdew and Yue Wang, *Phys. Rev. B*, **45**, 13244–13249 (1992).

[20] O. Gunnarsson and B. I. Lundqvist, *Phys. Rev. B*, **13**, 4274–4298 (1976).

[21] Kieron Burke, John P. Perdew, and Matthias Ernzerhof, *The Journal of Chemical Physics*, **109**, 3760–3771 (1998).

[22] Philipp Haas, Fabien Tran, and Peter Blaha, *Phys. Rev. B*, **79**, 085104 (2009).

[23] Viktor N. Staroverov et al., *Phys. Rev. B*, **69**, 075102 (2004).

[24] Kurt R. Brorsen et al., *The Journal of Physical Chemistry Letters*, **8**, 2076–2081 (2017).

[25] Klaus Capelle, *Brazilian Journal of Physics*, **36**, 1318 –1343 (2006).

[26] John P. Perdew, Kieron Burke, and Matthias Ernzerhof, *Phys. Rev. Lett.*, **77**, 3865–3868 (1996).

[27] Kieron Burke, John P. Perdew, and Yue Wang. "Derivation of a Generalized Gradient Approximation: The PW91 Density Functional". In: *Electronic Density Functional Theory: Recent Progress and New Directions*. Ed. by John F. Dobson, Giovanni Vignale, and Mukunda P. Das. Boston, MA: Springer US, 1998, 81–111. ISBN: 978-1-4899-0316-7.

[28] Chengteh Lee, Weitao Yang, and Robert G. Parr, *Phys. Rev. B*, **37**, 785–789 (1988).

[29] R. Armiento and A. E. Mattsson, *Phys. Rev. B*, **72**, 085108 (2005).

[30] Jorge Kohanoff. *Electronic Structure Calculations for Solids and Molecules: Theory and Computational Methods*. Cambridge University Press, 2006.

[31] John P. Perdew et al., *Phys. Rev. Lett.*, **82**, 2544–2547 (1999).

[32] Jianmin Tao et al., *Phys. Rev. Lett.*, **91**, 146401 (2003).

[33] Jianmin Tao and Yuxiang Mo, *Phys. Rev. Lett.*, **117**, 073001 (2016).

[34] Jianwei Sun, Adrienn Ruzsinszky, and John P. Perdew, *Phys. Rev. Lett.*, **115**, 036402 (2015).

[35] Axel D. Becke, *The Journal of Chemical Physics*, **98**, 1372–1377 (1993).

[36] Axel D. Becke, *The Journal of Chemical Physics*, **98**, 5648–5652 (1993).

[37] A. D. Becke, *Phys. Rev. A*, **38**, 3098–3100 (1988).

[38] Carlo Adamo, Gustavo E. Scuseria, and Vincenzo Barone, *The Journal of Chemical Physics*, **111**, 2889–2899 (1999).

[39] John P. Perdew, Matthias Ernzerhof, and Kieron Burke, *The Journal of Chemical Physics*, **105**, 9982–9985 (1996).

[40] Yan Zhao and Donald G. Truhlar, *Journal of Chemical Theory and Computation*, **2**, 1009–1018 (2006).

[41]   Yan Zhao and Donald G. Truhlar, *The Journal of Physical Chemistry A*, **109**, 5656–5667 (2005).

[42]   Juanita Jaramillo, Gustavo E. Scuseria, and Matthias Ernzerhof, *The Journal of Chemical Physics*, **118**, 1068–1073 (2003).

[43]   Erin R. Johnson, *The Journal of Chemical Physics*, **141**, 124120 (2014).

[44]   Hisayoshi Iikura et al., *The Journal of Chemical Physics*, **115**, 3540–3544 (2001).

[45]   Jochen Heyd, Gustavo E. Scuseria, and Matthias Ernzerhof, *The Journal of Chemical Physics*, **118**, 8207–8215 (2003).

[46]   Oleg A. Vydrov and Gustavo E. Scuseria, *The Journal of Chemical Physics*, **125**, 234109 (2006).

[47]   Mary A. Rohrdanz, Katie M. Martins, and John M. Herbert, *The Journal of Chemical Physics*, **130**, 054112 (2009).

[48]   Susi Lehtola et al., *SoftwareX*, **7**, 1 –5 (2018).

[49]   Robert G. Parr. "Density Functional Theory of Atoms and Molecules". In: *Horizons of Quantum Chemistry*. Ed. by Kenichi Fukui and Bernard Pullman. Dordrecht: Springer Netherlands, 1980, 5–15. ISBN: 978-94-009-9027-2.

[50]   Mel Levy and John P. Perdew, *Phys. Rev. A*, **32**, 2010–2021 (1985).

[51]   Elliott H. Lieb and Stephen Oxford, *International Journal of Quantum Chemistry*, **19**, 427–439 (1981).

[52]   John P. Perdew et al., *The Journal of Chemical Physics*, **140**, 18A533 (2014).

[53]   Jianwei Sun, John P. Perdew, and Adrienn Ruzsinszky, *Proceedings of the National Academy of Sciences*, **112**, 685–689 (2015).

[54]   Bikash Patra et al., *Phys. Rev. B*, **100**, 155140 (2019).

[55]   Pan Hao et al., *Journal of Chemical Theory and Computation*, **9**, 355–363 (2013).

[56] Lars Goerigk and Stefan Grimme, *Journal of Chemical Theory and Computation*, **7**, 291–309 (2011).

[57] Lars Goerigk and Stefan Grimme, *Journal of Chemical Theory and Computation*, **6**, 107–126 (2010).

[58] Roberto Peverati and Donald G. Truhlar, *Philosophical Transactions of the Royal Society A: Mathematical, Physical and Engineering Sciences*, **372**, 20120476 (2014).

[59] Yuxiang Mo et al., *Phys. Rev. B*, **95**, 035118 (2017).

[60] Denis Jacquemin and Carlo Adamo, *Journal of Chemical Theory and Computation*, **7**, 369–376 (2011).

[61] Jingjing Zheng, Yan Zhao, and Donald G. Truhlar, *Journal of Chemical Theory and Computation*, **5**, 808–821 (2009).

[62] Martin Weimer, Fabio Della Sala, and Andreas Görling, *Chemical Physics Letters*, **372**, 538 –547 (2003).

[63] Jennifer M. Smith, Yasaman Jami Alahmadi, and Christopher N. Rowley, *Journal of Chemical Theory and Computation*, **9**, 4860–4865 (2013).

[64] Thomas Bally and G. Narahari Sastry, *The Journal of Physical Chemistry A*, **101**, 7923–7925 (1997).

[65] Yingkai Zhang and Weitao Yang, *The Journal of Chemical Physics*, **109**, 2604–2608 (1998).

[66] Roi Baer, Ester Livshits, and Ulrike Salzner, *Annual Review of Physical Chemistry*, **61**, 85–109 (2010).

[67] Nobuyuki N. Matsuzawa et al., *The Journal of Physical Chemistry A*, **105**, 4953–4962 (2001).

[68] Mark E. Casida and Dennis R. Salahub, *The Journal of Chemical Physics*, **113**, 8918–8935 (2000).

[69] H. Appel, E. K. U. Gross, and K. Burke, *Phys. Rev. Lett.*, **90**, 043005 (2003).

[70] John P. Perdew et al., *Phys. Rev. Lett.*, **49**, 1691–1694 (1982).

[71] C.-O. Almbladh and U. von Barth, *Phys. Rev. B*, **31**, 3231–3244 (1985).

[72] John P. Perdew et al., *Phys. Rev. A*, **78**, 052513 (2008).

[73] P. J. Stephens et al., *The Journal of Physical Chemistry*, **98**, 11623–11627 (1994).

[74] Viktor N. Staroverov et al., *The Journal of Chemical Physics*, **119**, 12129–12137 (2003).

[75] Takeshi Yanai, David P Tew, and Nicholas C Handy, *Chemical Physics Letters*, **393**, 51 –57 (2004).

[76] A. D. Becke and M. R. Roussel, *Phys. Rev. A*, **39**, 3761–3767 (1989).

[77] Matthias Ernzerhof and John P. Perdew, *The Journal of Chemical Physics*, **109**, 3313–3320 (1998).

[78] Lucian A. Constantin, John P. Perdew, and Jianmin Tao, *Phys. Rev. B*, **73**, 205104 (2006).

[79] Andreas Savin and Heinz-Jürgen Flad, *International Journal of Quantum Chemistry*, **56**, 327–332 (1995).

[80] Jong-Won Song et al., *The Journal of Chemical Physics*, **129**, 184113 (2008).

[81] Yoshinobu Akinaga and Seiichiro Ten-no, *Chemical Physics Letters*, **462**, 348 –351 (2008).

[82] Weitao Yang, *The Journal of Chemical Physics*, **109**, 10107–10110 (1998).

[83] Richard M. Koehl, Gregory K. Odom, and Gustavo E. Scuseria, *Molecular Physics*, **87**, 835–843 (1996).

[84] Jianmin Tao, Michael Springborg, and John P. Perdew, *The Journal of Chemical Physics*, **119**, 6457–6464 (2003).

[85] John P. Perdew and Wang Yue, *Phys. Rev. B*, **33**, 8800–8802 (1986).

[86] Aliaksandr V. Krukau et al., *The Journal of Chemical Physics*, **129**, 124103 (2008).

[87] Ester Livshits and Roi Baer, *Phys. Chem. Chem. Phys.*, **9**, 2932–2941 (2007).

[88] Yoshihiro Tawada et al., *The Journal of Chemical Physics*, **120**, 8425–8433 (2004).

[89] Aron J. Cohen, Paula Mori-Sánchez, and Weitao Yang, *The Journal of Chemical Physics*, **126**, 191109 (2007).

[90] Prakash Verma and Rodney J. Bartlett, *The Journal of Chemical Physics*, **140**, 18A534 (2014).

[91] Yifan Jin and Rodney J. Bartlett, *The Journal of Chemical Physics*, **145**, 034107 (2016).

[92] Subrata Jana et al., *Chemical Physics Letters*, **713**, 1 –9 (2018).

[93] M. Valiev et al., *Computer Physics Communications*, **181**, 1477 –1489 (2010).

[94] Roberto Peverati and Donald G. Truhlar, *Philosophical Transactions of the Royal Society A: Mathematical, Physical and Engineering Sciences*, **372**, 20120476 (2014).

[95] Larry A. Curtiss et al., *The Journal of Chemical Physics*, **106**, 1063–1079 (1997).

[96] Subhas J. Chakravorty et al., *Phys. Rev. A*, **47**, 3649–3670 (1993).

[97] Robin Haunschild and Wim Klopper, *The Journal of Chemical Physics*, **136**, 164102 (2012).

[98] Benjamin J. Lynch, Yan Zhao, and Donald G. Truhlar. *Minnesota database for chemistry and solid state physics.* URL: `https://comp.chem.umn.edu/db/`.

[99] Kellar Autumn et al., *Proceedings of the National Academy of Sciences*, **99**, 12252–12256 (2002).

[100] Hobza P, Sponer J, and Polasek M, *Journal of the American Chemical Society*, **117**, 792–798 (1995).

[101] Robert L. Baldwin, *Journal of Molecular Biology*, **371**, 283 –301 (2007).

[102] Michelle L. Coote, Addy Pross, and Leo Radom, *Organic Letters*, **5**, 4689–4692 (2003).

[103] James A. Phillips and Christopher J. Cramer, *Journal of Chemical Theory and Computation*, **1**, 827–833 (2005).

[104] Stefan Grimme, *The Journal of Chemical Physics*, **124**, 034108 (2006).

[105] Yan Zhao and Donald G. Truhlar, *Theoretical Chemistry Accounts*, **120**, 215– 241 (2008).

[106] Yan Zhao and Donald G. Truhlar, *The Journal of Chemical Physics*, **125**, 194101 (2006).

[107] Yan Zhao and Donald G. Truhlar, *The Journal of Physical Chemistry A*, **110**, 5121–5129 (2006).

[108] Joseph L. Durant, *Chemical Physics Letters*, **256**, 595 –602 (1996).

[109] Yan Zhao, Benjamin J. Lynch, and Donald G. Truhlar, *The Journal of Physical Chemistry A*, **108**, 2715–2719 (2004).

[110] Yan Zhao, Núria González-García, and Donald G. Truhlar, *The Journal of Physical Chemistry A*, **109**, 2012–2018 (2005).

[111] H. Chermette et al., *The Journal of Chemical Physics*, **114**, 1447–1453 (2001).

[112] Aron J. Cohen, Paula Mori-Sánchez, and Weitao Yang, *Science*, **321**, 792–794 (2008).

[113] Aron J. Cohen, Paula Mori-Sánchez, and Weitao Yang, *Chemical Reviews*, **112**, 289–320 (2012).

[114] Lide. D. R. *CRC Handbook of Chemistry and Physics*. CRC, Boca Raton, 2004.

[115] Roberto Peverati and Donald G. Truhlar, *The Journal of Physical Chemistry Letters*, **2**, 2810–2817 (2011).

[116] Jeng-Da Chai and Martin Head-Gordon, *The Journal of Chemical Physics*, **128**, 084106 (2008).

[117] C. Ullrich. *Time-Dependent Density-Functional Theory: Concepts and Applications*. Oxford Graduate Texts. OUP Oxford, 2012. ISBN: 9780199563029.

[118] R. W. Godby, M. Schlüter, and L. J. Sham, *Phys. Rev. B*, **36**, 6497–6500 (1987).

[119] R. W. Godby, M. Schlüter, and L. J. Sham, *Phys. Rev. B*, **37**, 10159–10175 (1988).

[120] John P. Perdew et al., *Proceedings of the National Academy of Sciences*, **114**, 2801–2806 (2017).

[121] Zeng-hui Yang et al., *Phys. Rev. B*, **93**, 205205 (2016).

[122] Szymon Śmiga et al., *The Journal of Chemical Physics*, **146**, 064105 (2017).

[123] Antonio C. Cancio and Jeremy J. Redd, *Molecular Physics*, **115**, 618–635 (2017).

[124] Daniel Mejia-Rodriguez and S. B. Trickey, *Phys. Rev. A*, **96**, 052512 (2017).

[125] M. Brack, B.K. Jennings, and Y.H. Chu, *Physics Letters B*, **65**, 1 –4 (1976).

[126] C. H. Hodges, *Canadian Journal of Physics*, **51**, 1428–1437 (1973).

[127] Lucian A. Constantin, E. Fabiano, and F. Della Sala, *Phys. Rev. B*, **84**, 233103 (2011).

[128] Emil Proynov, Zhenting Gan, and Jing Kong, *Chemical Physics Letters*, **455**, 103 –109 (2008).

[129] Peter Elliott et al., *Phys. Rev. Lett.*, **100**, 256406 (2008).

[130] Lucian A. Constantin et al., *Phys. Rev. B*, **93**, 045126 (2016).

[131] P. R. Antoniewicz and Leonard Kleinman, *Phys. Rev. B*, **31**, 6779–6781 (1985).

[132] G. Kresse and J. Hafner, *Phys. Rev. B*, **47**, 558–561 (1993).

[133] G. Kresse and J. Furthmüller, *Computational Materials Science*, **6**, 15 –50 (1996).

[134] Fabien Tran and Peter Blaha, *Phys. Rev. Lett.*, **102**, 226401 (2009).

[135] Zhi-Hao Cui et al., *The Journal of Physical Chemistry Letters*, **9**, 2338–2345 (2018).

[136] Yoon-Suk Kim et al., *Phys. Rev. B*, **82**, 205212 (2010).

[137] Fabien Tran and Peter Blaha, *The Journal of Physical Chemistry A*, **121**, 3318– 3325 (2017).

[138] Nicolas Mounet et al., *Nature Nanotechnology*, **13**, 246–252 (2018).

[139] Boubacar Traoré et al., *Phys. Rev. B*, **99**, 035139 (2019).

[140] Hong Jiang, *The Journal of Chemical Physics*, **134**, 204705 (2011).

[141] Sefaattin Tongay et al., *Nano Letters*, **12**, 5576–5580 (2012).

[142] K. K. Kam and B. A. Parkinson, *The Journal of Physical Chemistry*, **86**, 463– 467 (1982).

[143] A. Ghafari et al., *Phys. Rev. B*, **84**, 125205 (2011).

[144] , *WIEN2k, An Augmented Plane Wave + Local Orbitals Program for Calculating Crystal Properties, P. Blaha, K. Schwarz, G. K. H. Madsen, D. Kvasnicka, J. Luitz, R. Laskowski, F. Tran and L. D. Marks*, (2018).

[145] Andreas Savin et al., *Angewandte Chemie International Edition in English*, **36**, 1808–1832 (1997).

[146] Bikash Patra et al., *Phys. Rev. B*, **100**, 045147 (2019).

[147] Lucian A. Constantin et al., *Phys. Rev. B*, **91**, 041120 (2015).

[148] E. Engel and S. H. Vosko, *Phys. Rev. B*, **47**, 13164–13174 (1993).

[149] Matthias Ernzerhof, *Chemical Physics Letters*, **263**, 499–506 (1996).

[150] Lucian A. Constantin, *Phys. Rev. B*, **78**, 155106 (2008).

[151] Lucian A. Constantin, *Phys. Rev. B*, **93**, 121104 (2016).

[152] Jianwei Sun et al., *The Journal of Chemical Physics*, **144**, 191101 (2016).

[153] Enrico Clementi and Carla Roetti, *Atomic Data and Nuclear Data Tables*, **14**, 177–478 (1974).

[154] Thilo Aschebrock and Stephan Kümmel, *Phys. Rev. Research*, **1**, 033082 (2019).

[155] William H. Press et al. *Numerical Recipes in Fortran 90 (2nd Ed.): The Art of Parallel Scientific Computing*. USA: Cambridge University Press, 1996. ISBN: 0521574390.

[156] Jianwei Sun et al., *Phys. Rev. B*, **84**, 035117 (2011).

[157] Lucian A. Constantin, Eduardo Fabiano, and Fabio Della Sala, *Phys. Rev. B*, **86**, 035130 (2012).

[158] John P. Perdew et al., *Phys. Rev. Lett.*, **103**, 026403 (2009).

[159] John P. Perdew et al., *Phys. Rev. Lett.*, **106**, 179902 (2011).

[160] Yihan Shao et al., *Molecular Physics*, **113**, 184–215 (2015).

[161] Saswata Dasgupta and John M. Herbert, *Journal of Computational Chemistry*, **38**, 869–882 (2017).

[162] Francis Birch, *Phys. Rev.*, **71**, 809–824 (1947).

[163]   Larry A. Curtiss et al., *The Journal of Chemical Physics*, **109**, 42–55 (1998).

[164]   Lars Goerigk et al., *Phys. Chem. Chem. Phys.*, **19**, 32184–32215 (2017).

[165]   Roberto Peverati and Donald G. Truhlar, *Philosophical Transactions of the Royal Society A: Mathematical, Physical and Engineering Sciences*, **372**, 20120476 (2014).

[166]   Amir Karton et al., *The Journal of Physical Chemistry A*, **112**, 12868–12886 (2008).

[167]   Yan Zhao and Donald G. Truhlar, *Journal of Chemical Theory and Computation*, **3**, 289–300 (2007).

[168]   Roberto Peverati, Yan Zhao, and Donald G. Truhlar, *The Journal of Physical Chemistry Letters*, **2**, 1991–1997 (2011).

[169]   Roberto Peverati and Donald G. Truhlar, *Journal of Chemical Theory and Computation*, **8**, 2310–2319 (2012).

[170]   Petr Jurečka et al., *Phys. Chem. Chem. Phys.*, **8**, 1985–1993 (2006).

[171]   Pragya Verma and Donald G. Truhlar, *The Journal of Physical Chemistry Letters*, **8**, 380–387 (2017).

[172]   Fabien Tran, Julia Stelzl, and Peter Blaha, *The Journal of Chemical Physics*, **144**, 204120 (2016).

[173]   Subrata Jana, Kedar Sharma, and Prasanjit Samal, *The Journal of Physical Chemistry A*, **123**, 6356–6369 (2019).

[174]   Abhirup Patra et al., *Proceedings of the National Academy of Sciences*, **114**, E9188–E9196 (2017).

[175]   Lorena Vega et al., *Journal of Chemical Theory and Computation*, **14**, 395–403 (2018).

[176]   Shaama Mallikarjun Sharada et al., *Phys. Rev. B*, **100**, 035439 (2019).

[177] C. S. Garoufalis, Aristides D. Zdetsis, and Stefan Grimme, *Phys. Rev. Lett.*, **87**, 276402 (2001).

[178] Fabien Tran, Peter Blaha, and Karlheinz Schwarz, *Journal of Physics: Condensed Matter*, **19**, 196208 (2007).

[179] Abhilash Patra et al., *Phys. Rev. B*, **102**, 045135 (2020).

[180] Fabien Tran, Peter Blaha, and Karlheinz Schwarz, *Journal of Chemical Theory and Computation*, **11**, 4717–4726 (2015).

[181] Takao Tsuneda et al., *The Journal of Chemical Physics*, **133**, 174101 (2010).

[182] You-Sheng Lin et al., *Journal of Chemical Theory and Computation*, **9**, 263–272 (2013).

[183] Mariam Barawi et al., *The Journal of Physical Chemistry C*, **120**, 9547–9552 (2016).

[184] Yanmei Xin et al., *ACS Sustainable Chemistry & Engineering*, **4**, 6659–6667 (2016).

[185] Amy L. Linsebigler, Guangquan. Lu, and John T. Yates, *Chemical Reviews*, **95**, 735–758 (1995).

[186] B. Thomas et al., *Journal of Crystal Growth*, **170**, 808–812 (1997).

[187] Jeffrey E. Post, *Proceedings of the National Academy of Sciences*, **96**, 3447–3454 (1999).

[188] B. Ammundsen and J. Paulsen, *Advanced Materials*, **13**, 943–956 (2001).

[189] Min-Ye Zhang, Zhi-Hao Cui, and Hong Jiang, *J. Mater. Chem. A*, **6**, 6606–6616 (2018).

[190] Zhi-Hao Cui, Feng Wu, and Hong Jiang, *Phys. Chem. Chem. Phys.*, **18**, 29914–29922 (2016).

[191] Adrienn Ruzsinszky et al., *Journal of Chemical Theory and Computation*, **8**, 2078–2087 (2012).

[192] James W. Furness et al., *The Journal of Chemical Physics*, **152**, 244112 (2020).

[193] Abhilash Patra, Subrata Jana, and Prasanjit Samal, *The Journal of Chemical Physics*, **153**, 184112 (2020).

[194] Thilo Aschebrock and Stephan Kümmel, *Phys. Rev. Research*, **1**, 033082 (2019).

[195] Hendrik J. Monkhorst and James D. Pack, *Phys. Rev. B*, **13**, 5188–5192 (1976).

[196] Atsushi Togo and Isao Tanaka, *Scripta Materialia*, **108**, 1–5 (2015).

[197] Mette S. Schmokel et al., *Chem. Sci.*, **5**, 1408–1421 (2014).

[198] N Benbattouche et al., *Journal of Physics D: Applied Physics*, **22**, 670–675 (1989).

[199] T. Chattopadhyay and H.G. von Schnering, *Journal of Physics and Chemistry of Solids*, **46**, 113 –116 (1985).

[200] , *Physics Letters A*, **80**, 59 –61 (1980).

[201] Fredrik Grønvold and Edgar F. Westrum, *The Journal of Chemical Thermodynamics*, **8**, 1039 –1048 (1976).

[202] A. Ennaoui et al., *Solar Energy Materials and Solar Cells*, **29**, 289 –370 (1993).

[203] I.J. Ferrer et al., *Solid State Communications*, **74**, 913 –916 (1990).

[204] D W Bullett, *Journal of Physics C: Solid State Physics*, **15**, 6163–6174 (1982).

[205] I. Opahle, K. Koepernik, and H. Eschrig, *Phys. Rev. B*, **60**, 14035–14041 (1999).

[206] Thomas J. Ahrens and Raymond Jeanloz, *Journal of Geophysical Research: Solid Earth*, **92**, 10363–10375 (1987).

[207] Jianwei Sun et al., *Nature Chemistry*, **8**, 831–836 (2016).

[208] Ruoshi Sun, M. K. Y. Chan, and G. Ceder, *Phys. Rev. B*, **83**, 235311 (2011).

[209] D. Spagnoli et al., *Phys. Rev. B*, **81**, 094106 (2010).

[210] K. V. KRISHNA RAO, S. V. NAGENDER NAIDU, and LEELA IYENGAR, *Journal of the American Ceramic Society*, **53**, 124–126 (1970).

[211] Zhu Jun et al., *Chinese Physics B*, **17**, 2216–2221 (2008).

[212] V. Swamy and L.S. Dubrovinsky, *Journal of Physics and Chemistry of Solids*, **62**, 673 –675 (2001).

[213] Stacey J. Smith et al., *American Mineralogist*, **94**, 236–243 (2009).

[214] J. Pascual, J. Camassel, and H. Mathieu, *Phys. Rev. B*, **18**, 5606–5614 (1978).

[215] H. Tang et al., *Solid State Communications*, **87**, 847 –850 (1993).

[216] Sophie Fritsch, Jeffrey E. Post, and Alexandra Navrotsky, *Geochimica et Cosmochimica Acta*, **61**, 2613–2616 (1997).

[217] Weifeng Wei et al., *Chem. Soc. Rev.*, **40**, 1697–1721 (2011).

[218] Sophie Fritsch et al., *Chemistry of Materials*, **10**, 474–479 (1998).

[219] D Balachandran et al., *Journal of Solid State Chemistry*, **173**, 462–475 (2003).

[220] Daniil A. Kitchaev et al., *Phys. Rev. B*, **93**, 045132 (2016).

[221] Yubo Zhang et al., *The Journal of Chemical Physics*, **150**, 014105 (2019).

[222] Albert P. Bartók and Jonathan R. Yates, *The Journal of Chemical Physics*, **150**, 161101 (2019).

[223] James W. Furness et al., *The Journal of Physical Chemistry Letters*, **11**, 8208–8215 (2020).

[224] Daniel Mejia-Rodriguez and S. B. Trickey, *Phys. Rev. B*, **98**, 115161 (2018).

[225] Daniel Mejía-Rodríguez and S. B. Trickey, *Phys. Rev. B*, **102**, 121109 (2020).

[226] Ralf Neumann, Ross H. Nobes, and Nicholas C. Handy, *Molecular Physics*, **87**, 1–36 (1996).